



TECHNICAL UNIVERSITY OF LIBEREC
Faculty of Mechatronics, Informatics
and Interdisciplinary Studies ■

MIRROR ALIGNMENT CONTROL FOR COMPASS RICH-1 DETECTOR AT CERN

Dissertation

Study programme: P2612 – Electrotechnology and informatics

Study branch: 2612V045 – Technical Cybernetics

Author: **Ing. Lukáš Steiger**

Supervisor: doc. RNDr. Miroslav Šulc, Ph.D.





TECHNICKÁ UNIVERZITA V LIBERCI
Fakulta mechatroniky, informatiky
a mezioborových studií ■

POČÍTAČOVÁ KOREKCE ROZKLADĚNÍ POLOHY ZRCADEL V DETEKTORU ČERENKOVOVA ZÁŘENÍ RICH-1 EXPERIMENTU COMPASS V EVROPSKÉM STŘEDISKU JADERNÝCH VÝZKUMŮ CERN

Disertační práce

Studijní program: P2612 – Elektrotechnika a informatika

Studijní obor: 2612V045 – Technická kybernetika

Autor práce: **Ing. Lukáš Steiger**

Vedoucí práce: doc. RNDr. Miroslav Šulc, Ph.D.



Prohlášení

Byl jsem seznámen s tím, že na mou disertační práci se plně vztahuje zákon č. 121/2000 Sb., o právu autorském, zejména § 60 – školní dílo.

Beru na vědomí, že Technická univerzita v Liberci (TUL) nezasahuje do mých autorských práv užitím mé disertační práce pro vnitřní potřebu TUL.

Užiji-li disertační práci nebo poskytnu-li licenci k jejímu využití, jsem si vědom povinnosti informovat o této skutečnosti TUL; v tomto případě má TUL právo ode mne požadovat úhradu nákladů, které vynaložila na vytvoření díla, až do jejich skutečné výše.

Disertační práci jsem vypracoval samostatně s použitím uvedené literatury a na základě konzultací s vedoucím mé disertační práce a konzultantem.

Datum:

Podpis:

Abstract

This Thesis summarizes various attitudes for the alignment measurements of large segmented mirrors. Especially in the field of Ring Imaging Cherenkov (RICH) detectors for particle physics, the measurement arrangement is limited mainly by the available space and material budget influencing the acceptance area of the spectrometer.

The detector RICH1 of the COMPASS experiment at CERN SPS is a large size gaseous Cherenkov detector with two reflecting spherical surfaces formed by hexagonal and pentagonal mirrors, with individual degrees of freedom for angular adjustment. The mirror elements must be very accurately aligned so to form a focused image in the detector photon detection area. Any misalignments distort the image and thus directly affect the detector resolution. The mirrors had been carefully adjusted before the start of the experiment data taking period, but the influence of external vibrations, temperature fluctuation and hydrostatic pressure in the radiator gas causes misalignments of some mirrors. There was no possibility to check and monitor this effect during the data taking period of typically 6 – 8 months.

An original method was applied for on-line mirror alignment monitoring. The rectangular grid, placed near the focal plane of the mirror wall inside the detector vessel is illuminated by high luminosity LEDs. The image of the grid, reflected by the spherical mirrors, is monitored by digital camera. Small tilts of a mirror create discontinuities of the grid line image. The observed shift provides the direction and value of the mirror tilt. The required resolution of the measurement is in the order of 0.1 mrad.

Two attitudes, the relative measurement and the absolute measurement, are tested and compared with two independent methods. In the Thesis, image processing techniques are adopted to analyze the position of the grid image, deformed by a reflection on individual spherical mirrors. To determine the absolute misalignment of the mirrors the precise position of the camera has to be known. The position of the camera is calculated using the close range photogrammetry where the influence of optical system parameters has to be considered.

For the precise measurement of the mirror tilt a new method was developed based on the optical reconstruction of line images and photogrammetry targets positions. It is shown that the sensitivity of the monitoring method is sufficient, i.e. 0.1 mrad, and that the measured misalignments can be included in the particle identification algorithm. The positions of COMPASS RICH1 mirrors are determined.

Abstrakt

Dizertační práce se zabývá automatickou detekcí přesné polohy segmentů velkých zrcadelových stěn, zejména v oblasti Čerenkovových detektorů (RICH) určených pro částicovou fyziku.

Detektor RICH1 je součástí experimentu COMPASS v CERN. Jednou z jeho komponent je multisegmentální stěna zrcadel. Jednotlivé segmenty zrcadel tvoří dvě sféry, které slouží ke směřování Čerenkovových fotonů do detekční části detektoru. Pro vytvoření jasného obrazu v detekční části musí být všechny segmenty zrcadelové stěny přesně zarovnané. Jakékoliv vychýlení některého ze segmentů deformuje detekovaný obraz a tím přímo ovlivňuje rozlišení detektoru RICH1. Zrcadla byla přesně nastavena před zahájením experimentu COMPASS, ale působením okolních vlivů, t.j. vnějších vibrací, kolísání teploty a atmosférického tlaku, dochází k vychýlení poloh některých segmentů. Během probíhajícího experimentu není možné sledovat pohyb jednotlivých zrcadel. Toto období obvykle trvá 6–8 měsíců.

V roce 2005 byla navržena nová metoda pro on-line sledování zarovnání zrcadel. Základní myšlenka této metody je jednoduchá - nejsou-li přilehlé segmenty zrcadel vůči sobě správně zarovnané, obraz libovolného objektu se v nich jeví porušeně. Čtyři fotoaparáty, rozmístěné v rozích detektoru RICH1, slouží ke snímání odrazu pravoúhlé sítě stěnou zrcadel. Tato síť se ve fotoaparátu zobrazí jako soustava protnutých kuželoseček. Vychýlení zrcadla ze své správné polohy se projeví posunem sítě v odpovídající části snímku. Pozorovaný posun obrazu sítě poskytuje informaci o směru a naklonění zrcadla. Aby nedošlo k degradaci v rozlišení částic v detektoru RICH1, zrcadla musí být zarovnaná s přesností 0.1 mrad.

V dizertační práci jsou rozebrány dva přístupy k detekci vychýlení zrcadel - relativní měření a absolutní měření. Idea relativního měření spočívá v porovnávání dvou snímků odpovídajících si zrcadel vzniklých v různém časovém období. Absolutní měření spočívá v určení velikosti a směru natočení zrcadla bez znalosti jeho původní orientace. V práci jsou použity metody zpracování obrazu a metody fotogrametrie.

Pro přesné měření polohy jednotlivých zrcadelových segmentů byla vyvinuta nová metoda, která je založena na principech paprskové optiky. Tato metoda je použita pro zjištění poloh všech zrcadel v detektoru RICH1. V práci je dokázáno, že citlivost této metody je lepší než 0.1 mrad. Tato nová originální metoda může být obecně použita i pro další plynové RICH detektory.

Acknowledgements

I would like to express my thanks to all my colleagues for the help and constant support. My greatest thanks belong to my family for the continuous support and endless patience.

Contents

List of Figures	10
List of Tables	13
Notation	14
1 Introduction	19
1.1 Motivation and Goal of the Thesis	19
1.2 Structure of the Thesis	19
2 Background	21
2.1 COMPASS experiment	21
2.2 RICH1 detector	21
3 State-of-the-Art of the mirror misalignment measurement	31
3.1 Theodolite in autocollimation mode	31
3.2 Alignment of the optical system with data	32
3.3 Laser Alignment Monitoring System for the RICH	34
3.4 Mirror alignment for Cherenkov Telescopes	36
3.5 Suitability of the existing methods for the COMPASS RICH1	38
4 CLAM - Online mirror alignment monitoring method	40
4.1 Hardware arrangement	40
4.1.1 Cameras	42
4.1.2 Retro-reflective grid	43
4.2 Control system	45
4.3 Summary	47
5 CLAM - Relative measurement	49
5.1 Introduction	49

5.2	Calibration of the method	50
5.3	Image processing	52
5.3.1	Mathematical morphology	52
5.3.2	Hough transform	54
5.4	Summary and results	56
6	CLAM - Absolute method	58
6.1	Photogrammetry	59
6.1.1	Interior orientation of a camera	59
6.1.1.1	Finite element method model	66
6.1.1.1.1	FEM model of the filling of the vessel	66
6.1.1.1.2	FEM model of the temperature in- fluence	70
6.1.2	Exterior orientation of a camera and collinearity equa- tions	76
6.1.2.1	Photogrammetric targets on the frame of the mirror wall	79
6.1.2.2	Image processing	83
6.1.3	Sensitivity analysis of the camera position algorithm	87
6.2	Determination of mirror orientation	92
6.2.1	Image processing	95
6.3	Results	97
6.3.1	Simulations	97
6.3.2	Sensitivity of the absolute method algorithm	99
6.3.3	CLAM measurements in RICH1 detector	99
6.3.3.1	Time of illumination influence	101
6.3.3.2	Filling RICH1 vessel with C_4F_{10}	101
6.3.3.3	Measurements during COMPASS run	104
6.4	Prospects	108
7	Conclusions	110
	Bibliography	114
	Publications of the Author	123
	Publications of the Author which are not directly related to the Thesis	124

List of Figures

2.1	scheme of the CERN accelerator complex	22
2.2	The COMPASS spectrometer	23
2.3	Cherokov effect	24
2.4	Schematic view of the COMPASS RICH1 detector	25
2.5	Working principle of the COMPASS RICH1 detector	27
2.6	Mirror holders	28
2.7	RICH1: A typical event display	29
3.1	Theodolite in autocollimation mode	32
3.2	Cherenkov rings for HERA-b	33
3.3	Unambiguous photons	34
3.4	LAMS scheme	35
3.5	Telescope mirror alignment technique with source at infinite distance	36
3.6	Telescope mirror alignment technique with source at infinite distance: CCD image of a star before alignment	37
4.1	Continuous Line Alignment Monitoring method for RICH mirrors - simulation	41
4.2	Continuous Line Alignment Monitoring method for RICH mirrors - differential image	42
4.3	Continuous Line Alignment Monitoring method for RICH mirrors - HW components	43
4.4	Photogrammetric targets - name definition.	45
4.5	Continuous Line Alignment Monitoring method for RICH mirrors - control system	46
4.6	Continuous Line Alignment Monitoring method for RICH mirrors - the output image	47

5.1	CLAM - relative measurement - laboratory setup and typical result	51
5.2	Relative measurement - visual inspection	57
6.1	Image series for the camera calibration.	62
6.2	Multiple media photogrammetric model	64
6.3	Radial pixel shift caused by multiple media environment	65
6.4	Geometry of the 2-D FEM model of the filling of the vessel with the C_4F_{10}	67
6.5	Graphical results of the 2-dimensional two-phase fluid flow FEM model	69
6.6	Geometry of the 2-D FEM model of varying ambient temperature in the course of one day	71
6.7	Change of the refractive index in the course of time	73
6.8	Graphical results of the 2-dimensional heat transfer FEM model	75
6.9	RICH1 mirrors and structure points	78
6.10	Photogrammetric targets on the mirror wall	79
6.11	CLAM targets on the mirror wall	81
6.12	Photogrammetric target - beams in glass ball	82
6.13	Photogrammetric target - deflection of the beam vs. relative principal ray position	83
6.14	Photogrammetric targets on the mirror wall	85
6.15	Image preprocessing in camera position algorithm	86
6.16	Camera position determination - inaccuracy in input coordinates	88
6.17	Camera position determination - depending on the number of input targets	89
6.18	Camera position determination - depending on one missing target	89
6.19	Camera position determination - depending on the illumination time	91
6.20	Determination of mirror orientation - principle geometry	92
6.21	Determination of mirror orientation - principle geometry in 2D coordinate system	93
6.22	Determination of mirror orientation - the spherical coordinate system in the RICH1.	95
6.23	Photogrammetric targets reflected by the mirror wall	96
6.24	Mirror misalignments - Simulations	98
6.25	Mirror misalignments - Laboratory measurements	100

6.26	Mirror misalignments - Time of illumination	102
6.27	Mirror misalignments - Time of illumination, two LEDs . . .	103
6.28	Mirror misalignments - Filling the RICH1 vessel with C_4F_{10}	104
6.29	Mirror misalignments - Mirror misalignments during the COM- PASS run period	105
6.30	Mirrors misalignments - complete list of mirrors	106
6.31	Mirrors misalignments - histograms	107

List of Tables

4.1	Photogrammetric targets names explanations	44
6.1	The summary of distortion parameters of the CLAM cameras.	63
6.2	Material parameters of N_2 and C_4F_{10} used in numerical simulation of two-phase fluid flow.	70
6.3	Material parameters of N_2 used in numerical simulation of the heat transfer in the fluid.	72
6.4	The coordinates of the CLAM reference targets placed on the frame of the mirror wall	80

Abbreviations and Symbols

Abbreviations

ASPRS	American Society for Photogrammetry and Remote Sensing
CERN	the European Organization for Nuclear Research
CLAM	Continuous Line Alignment Monitoring method for RICH mirrors
COMPASS	The Common Muon and Proton Apparatus for Structure and Spectroscopy
FEM	Finite Element Method
FM	Faculty of Mechatronics, Informatics and Interdisciplinary Studies
GEANT4	GEometry ANd Tracking
IACT	Imaging Atmospheric Cherenkov Telescope
JB	Jura-Bottom - position of CLAM camera in RICH1 detector
JT	Jura-Top - position of CLAM camera in RICH1 detector
LAMS	Laser Alignment Monitoring System
LED	Light Emitting Diode
MAPMT	MultiAnode PhotoMultiplier Tube
MWPC	Multi-Wire Proportional Chamber
PC	Personal Computer
PID	Particle Identification
RICH	Ring Imaging Cherenkov detector
SB	Saleve-Bottom - position of CLAM camera in RICH1 detector
SPS	Super Proton Synchrotron
ST	Saleve-Top - position of CLAM camera in RICH1 detector
TUL	Technical University of Liberec
VUV	Vacuum UltraViolet
VERITAS	Very Energetic Radiation Imaging Telescope Array System

Symbols of physical variables and constants

A_1, A_2, A_3	radial distortion parameters
B_1, B_2	tangential distortion parameters
A, B	coefficients correspond to the misalignment of individual mirrors of the RICH mirror wall
c (ms^{-1})	speed of light in vacuum
c ($\text{m}^3 \cdot \text{kg}^{-1}$)	Gladstone-Dale constant (FEM model)
C	calculated center of the Cherenkov ring
C_p ($\text{J} \cdot \text{kg}^{-1} \cdot \text{K}^{-1}$)	specific heat capacity at a constant pressure (FEM model)
C'	measured center of the Cherenkov ring
C_k	center of curvature of top/bottom part of the mirror wall
C_1, C_2	affinity and shear distortion parameters
D	image of point of the retroreflective rectangular grid on the camera sensor given in 3D coordinates
E	point of the retroreflective rectangular grid in 3D coordinates
E_{th}	threshold value of the total energy at which Cherenkov radiation is emitted
f_c (m)	objective focal length
g	number of general entity
\mathbf{g} ($\text{m} \cdot \text{s}^{-2}$)	gravity vector
h	number of general entity
h (m)	height of the vessel (FEM model)
hor	value of the shift of conics in mirror in horizontal direction
H'	principal point
i	index number
j	index number
k ($\text{W} \cdot \text{m}^{-1} \cdot \text{K}^{-1}$)	thermal conductivity (FEM model)
k_{ij}	matrix coefficients in pixel shift vs mirror tilt relationship
m (kg)	mass

m_0 (kg)	rest mass
n	index of refraction
N	number of detected photons
p (Pa)	pressure (FEM model)
p (m)	pixel size
p_{th}	threshold momenta at which Cherenkov radiation is emitted
P	principal point of a camera given in 3D coordinates
\mathbf{q} ($\text{W}\cdot\text{m}^{-2}$)	heat flux vector (FEM model)
Q ($\text{W}\cdot\text{m}^{-3}$)	heat source or sink (FEM model)
r_c (m)	Cherenkov ring radius
r'_{rad}	radial distortion; radial shift
r (m)	photogrammetric target - distance from the optical axis
R (m)	radius of curvature of the spherical mirror
R (m)	photogrammetric target - ball radius
R_{specific} ($\text{J}\cdot\text{kg}^{-1}\cdot\text{K}^{-1}$)	individual gas constant (FEM model)
S	reflection point on the mirror surface given in 3D coordinates
t (s)	time (FEM model)
t_{max} (s)	time at the T_{max} (FEM model)
T (K)	thermodynamic temperature (FEM model)
T_0 (K)	initial temperature (FEM model)
$T_{\text{BC}}(t)$ (K)	temperature boundary condition as a function of time (FEM model)
T_{min} (K)	minimum temperature in the temperature boundary condition function (FEM model)
T_{max} (K)	maximum temperature in the temperature boundary condition function (FEM model)
s	scale factor in projection equation
u (ms^{-1})	particle velocity in current medium
\mathbf{u} ($\text{m}\cdot\text{s}^{-1}$)	velocity vector (FEM model)
U_0 ($\text{m}\cdot\text{s}^{-1}$)	incoming velocity vector amplitude (FEM model)
v (ms^{-1})	phase velocity of light in current medium
ver	value of the shift of conics in mirror in vertical direction
w (m)	width of the vessel (FEM model)
x, y (m)	orthogonal coordinates (FEM model)
x'_0, y'_0	image coordinates of principle point H'

x'_p, y'_p	image coordinates of object in the image
$\Delta x', \Delta y'$	axis-related correction values for imaging errors
$\Delta\alpha$ (rad/turn)	angular resolution
α (rad)	camera's view direction around x-axis
α (rad)	chamfer angle of the vessel (FEM model)
β (rad)	camera's view direction around y-axis
α (rad)	angle angle of incidence
β (rad)	angle angle of refraction
ϵ (m)	parameter controlling interface thickness in a level set function (FEM model)
φ (rad)	mirror tilt in horizontal direction
φ (rad)	azimuthal angle of the Cherenkov photon
φ_0 (rad)	measured azimuthal angle around the Cherenkov ring
φ_{ch} (rad)	calculated azimuthal angle around the Cherenkov ring
Φ (1)	Level set function (FEM model)
γ (rad)	camera's view direction around z-axis
γ (rad)	deflection angle
λ (nm)	wavelength
μ (Pa·s)	dynamic viscosity of a fluid (FEM model)
μ_1 (Pa·s)	dynamic viscosity of Fluid 1 – N ₂ (FEM model)
μ_2 (Pa·s)	dynamic viscosity of Fluid 2 – C ₄ F ₁₀ (FEM model)
ϱ (kg·m ⁻³)	mass density of a fluid (FEM model)
ϱ_1 (kg·m ⁻³)	mass density of Fluid 1 – N ₂ (FEM model)
ϱ_2 (kg·m ⁻³)	mass density of Fluid 2 – C ₄ F ₁₀ (FEM model)
τ	vector of unknown variables in collinearity equations
θ (rad)	Cherenkov angle
θ_0 (rad)	measured Cherenkov angle
θ_{ch} (rad)	Cherenkov angle
$\theta_{ph,i}$	reconstructed photon angles
ϑ (rad)	mirror tilt in vertical direction
ρ (m)	distance from the origin to the line along a vector perpendicular to the line
σ (rad)	single ring resolution
σ_θ (rad)	error of the reconstructed Cherenkov photon angle
	θ

σ (m) standard deviation in the Gauss function (FEM model)

Commonly used mathematical symbols

\mathbf{I}	second-order identity matrix
∇	Del operator (gradient operator), represented by the nabla symbol
Δ	finite difference
\cdot	vector dot(scalar) product
\times	vector cross product
$\ \cdot \ $	Euclidean norm
\subset	set theory - subset
\cup	set theory - union
\sum	set theory - summation
\ominus	mathematical morphology - erosion
\oplus	mathematical morphology - dilation
\circ	mathematical morphology - image opening
\bullet	mathematical morphology - image closing

1. Introduction

1.1 Motivation and Goal of the Thesis

Ring imaging Cherenkov counters allow to detect electrically charged particles. As the particle is traversing the medium of the detector it emits so called Cherenkov photons along its way through the detector. The resulted cone of light is then focused towards the photon detection area. The image focalization is obtained by a large reflecting (spherical) surfaces composed of many mirror segments of a smaller size, which must be very accurately aligned to form a single smooth reflecting surface. Any misalignment directly affects the detector resolution. The possibility to monitor and correct the misalignment of the mirror wall is difficult particularly in RICH detectors with extended gas radiators, where the mirror wall is placed inside the RICH vessel in the gas atmosphere. In such cases, the mirror wall alignment can be measured only before filling and closing the vessel of the detector.

In case of the COMPASS RICH1 detector the single photon angular resolution is about 2 mrad. The mirror misalignment errors contribute with the error of 0.6 mrad for the central region and 1.3 mrad in the peripheral region of the detection area of the RICH1 detector. To limit the mirror misalignments effect the continuous line alignment monitoring method (CLAM) was proposed. The aim of this Thesis is to apply the CLAM method to contribute to the increase of the angular resolution of the detector.

1.2 Structure of the Thesis

The Thesis is organized into 7 chapters as follows:

- *Chapter 1. Introduction* describes the motivation behind the work efforts together with the goals and the brief outline of the Thesis.

- *Chapter 2. Background* introduces the reader to the necessary experimental background of the RICH1 detector. The Chapter presents theoretical basics of the COMPASS experiment at CERN SPS and puts emphasis on the RICH1 detector. The Cherenkov radiation and hardware setup of the detector are described.
- *Chapter 3. State-of-the-Art of the mirror misalignment measurement* surveys the current state-of-the-art. The literature review of the state of the art in the field of the mirror misalignment measurement in RICH detectors is presented.
- *Chapter 4. CLAM - Online mirror alignment monitoring method* introduces the proposal for the online mirror monitoring system for the RICH1 detector. The hardware arrangement and the used control system are described.
- *Chapter 5. CLAM - Relative measurement:* The objective of the study presented in this Chapter is to analyze the relative measurement method, to present its advantages and limitations.
- *Chapter 6. CLAM - Absolute method* presents the method to monitor misalignments of a segmented sphere. The sphere is composed of a large set of spherical mirrors. It is shown that each mirror can be measured individually only with the knowledge of its theoretical position inside the RICH1 vessel. Change of ambient conditions affecting the measurements are also discussed.
- *Conclusions:* Summarizes the results of the research presented in the Thesis.

2. Background

This Chapter introduces the reader to the experimental background of the RICH1 detector.

2.1 COMPASS experiment

The COMPASS experiment [1–5] is a fixed target experiment at Super Proton Synchrotron (SPS) at CERN in Geneva, Switzerland. It is located at the North Area of CERN. The aim of the COMPASS is to study in detail the nucleon spin structure via a high energy muon beam and to perform hadron spectroscopy via a hadron beam. Basically the experiment looks at the complex ways in which the elementary quarks and gluons form a particle, for example, understanding the contribution of the gluons to the spin of the proton and other nuclei and the production and investigation of other exotic particles. To study the produced particles of a wide range momenta, the COMPASS spectrometer is designed in two stages (Figure 2.2), each equipped with trackers and calorimeters [6]. Particle identification is ensured within the first stage of the spectrometer, where a large size Cherenkov imaging counter, RICH1, is placed.

2.2 RICH1 detector

A Ring Imaging Cherenkov detector allows the identification of electrically charged subatomic particles through the detection of the Cherenkov radiation.

Cherenkov radiation is used in the field of particle physics experiments by Ring Imaging Cherenkov detectors to exploit the so called Particle Identification (PID). In diagnostic medicine it is employed to detect radioactive phosphorus [9]. It can also be used to characterize the remaining radioactivity of spent fuel rods in nuclear reactors. In astrophysics it is used to

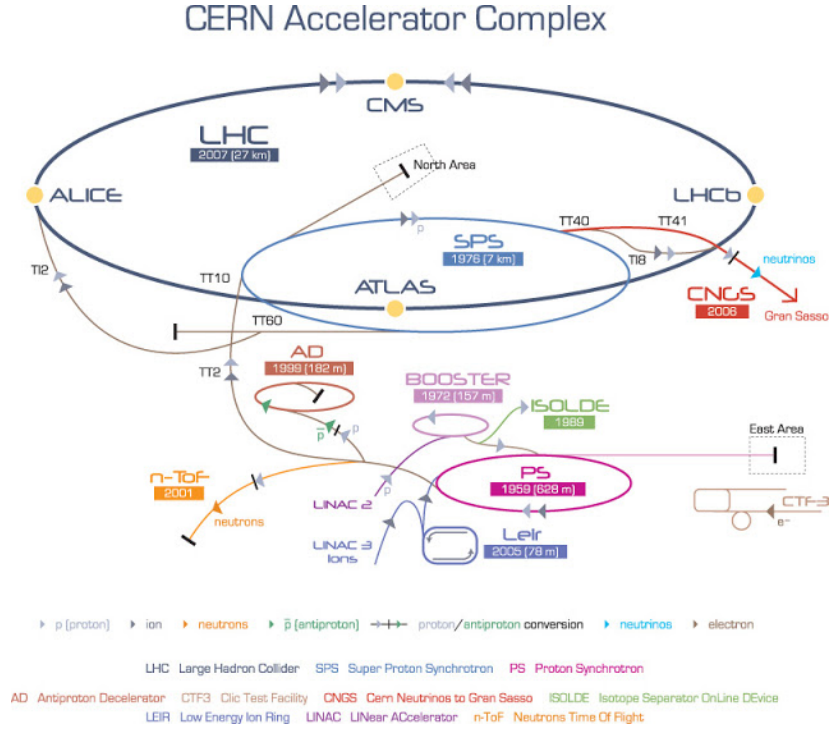


Figure 2.1: scheme of the CERN accelerators complex [7].

identify the source and intensity of the incoming cosmic or gamma rays. More detailed information can be found in [10–12].

The Cherenkov electromagnetic radiation is emitted by a charged particle passing through a transparent dielectric medium at a speed greater than the phase velocity of light in that medium. When the charged particle is passing through the medium it polarizes molecules of the medium. As the molecules turn back to their ground state, they emit photons in the process as it can be seen in Figure 2.3. These photons interfere with each other generating a cone of light at an angle of emission, θ_{ch} , of the Cherenkov radiation with respect to the particle's velocity. The angle θ_{ch} can be computed with formula $\cos(\theta_{ch}) = c/(un)$, where u stands for the particle velocity, c stands for the speed of light in vacuum and n stands for the refractive index of the medium. When the charged particle reaches a speed slower than the speed of light in current medium, photons interfere destructively with each other and no radiation is detected. We can calculate the minimum value of the total energy at which Cherenkov radiation

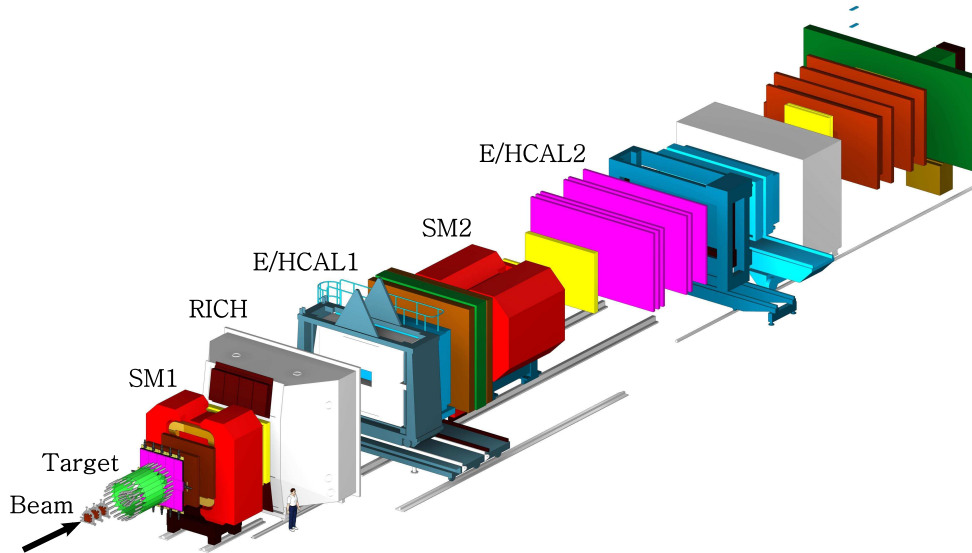


Figure 2.2: The COMPASS spectrometer setup. Position of calorimeters (HCAL1, HCAL2), magnets (SM1, SM2), polarized target and RICH1 is presented [8].

is emitted, using the following formula:

$$E_{th} = mc^2 = \frac{m_0c^2}{\sqrt{1 - \frac{u^2}{c^2}}} \quad (2.1)$$

This effect was discovered by P.A. Cherenkov in 1934 [13]. Three years later I. Tamm and I. Frank described the physical process theoretically [14].

The Figure 2.4 shows the COMPASS Experiment setup parts. The COMPASS RICH1 [15] is located between the magnets SM1 and SM2 and is designed to cover the acceptance of the first stage of the spectrometer (i.e. ± 250 mrad in the horizontal plane and ± 180 mrad in the vertical plane), achieving charge hadrons separation above three standard deviation levels (pions, kaons and protons) of particle momentum up to 60 GeV/c. Large volume vessel of the RICH1 detector is filled with heavy fluorocarbon radiator gas C_4F_{10} [16, 17]. Its refractive index is $n \approx 1.00153$ at 7 eV

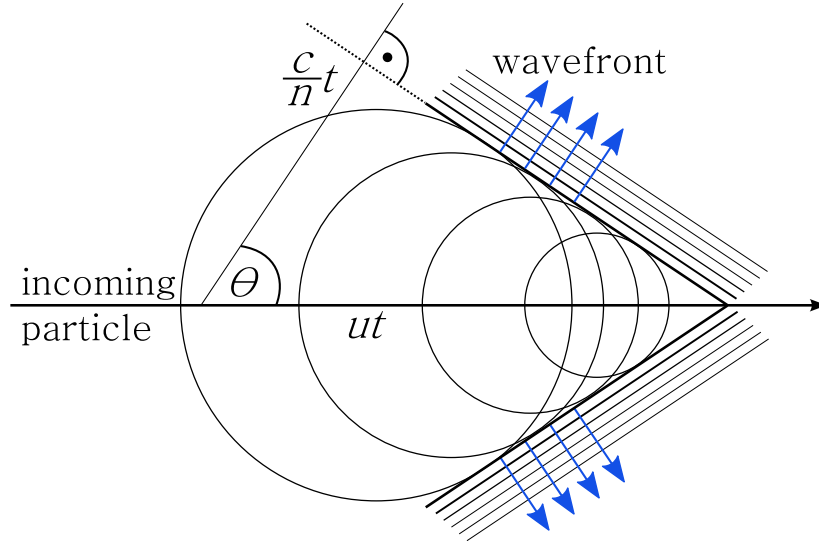


Figure 2.3: Cherenkov effect principle. Particle crossing a medium at greater speed (u) than the phase velocity of light in that medium $v = c/n$, where c stands for the speed of light in vacuum and n stands for the refractive index of the medium, generates so called Cherenkov photons, which form a cone of light with Cherenkov angle θ_{ch} .

at atmospheric pressure and room temperature. Corresponding threshold momenta p_{th} for emission of Cherenkov photons are: $p_{th} \approx 2.5, 8.9$ and 17.0 GeV/c for pions, kaons and protons respectively.

The overall scheme of the detector RICH1 is in Figure 2.4. The ability of a RICH detector to successfully detect the particle depends on two principal factors: the effective angular resolution per photon σ and the maximum number of detected photons in the photon detection area. The number of detected photons depends upon the length of the particle path in the radiator, the photon transmission through the radiator material, the photon transmission through the optical system of the detector and the quantum efficiency of the photon detectors.

To produce sufficient number of Cherenkov photons in C_4F_{10} the overall length of the radiator vessel is of about 3 m. The volume is about 80 m^3 . A dedicated control system [18] is used to monitor and control gas pressure and temperature inside the vessel and it also maintains the radiator gas transparency. The pressure is kept constant within 10 Pa above the atmospheric pressure in order to avoid damages to the thin vessel walls, and to avoid mechanical deformation of the vessel itself, which can be transferred

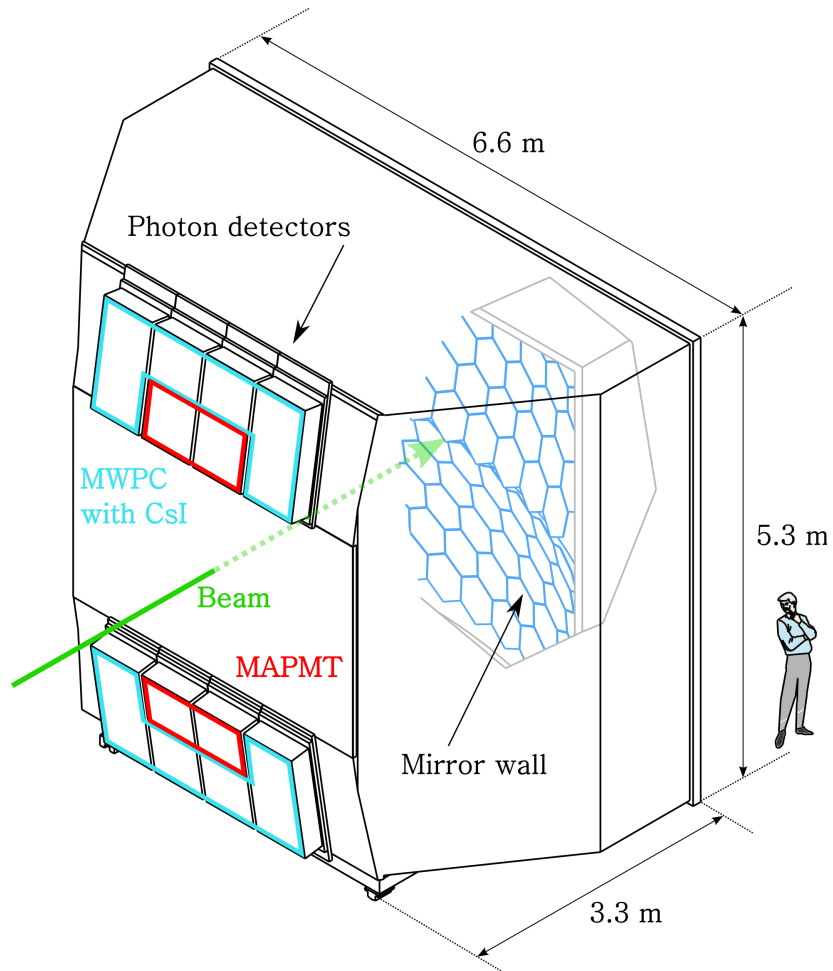


Figure 2.4: Schematic view of the COMPASS RICH1 detector with dimensions. The photon sensitive surface area of RICH1 is equipped with large-size Multi-Wire Proportional Chambers with CsI photocathodes (blue) and the inner part of the detection area is instrumented with a detection system based on MultiAnode PhotoMultiplier Tubes (red) since 2006 [8].

to the mirror wall.

Since the most Cherenkov radiation is in the ultraviolet spectrum, RICH1 operates in the Vacuum UltraViolet (VUV) wavelength domain. Optimum VUV transparency is achieved by continuous filtering of VUV absorbing impurities such as oxygen and water vapour. As a result, water vapour traces below 1 ppm and O₂ below 3 ppm are routinely obtained.

Cherenkov photons emitted in the gas are reflected by two spherical mirror surfaces of total area larger than 21 m² towards the photon detection chambers. The chambers are placed outside the COMPASS spectrometer acceptance. Such arrangement focuses the cone of light produced by particle crossing the radiator towards the detector plane, where it generates image of a ring, regardless of the photon emission point along the trajectory of the particle. Furthermore, the arrangement fulfills the requirement of a minimal amount of material budget along the particle trajectories and ensures stable operation of the photon detectors.

The mirror wall is formed by a mosaic arrangement of 116 spherical UV mirror elements [19] and is split in two parts by the horizontal plane on the beam axis. The clearance left between adjacent mirror segments results in a 4 % loss of the reflecting surface. The radius of curvature of 6606 mm \pm 20 mm is equal for both spheres [20]. To ensure a good reflectance in the VUV region (83 – 87 %), mirrors are coated with 80 nm reflective layer of aluminum (Al) and with 30 nm protective layer of magnesium fluoride (MgF₂).

The mechanical structure supporting the mirror wall has a net-like configuration with spherical design made from aluminum. The mirrors are suspended to the nodal points (Figure 2.6). Due to this particular arrangement, only angular adjustment of the mirror units is possible. Each mirror is coupled to a fine thread screw which allows it to rotate around two orthogonal axes with angular resolution $\Delta\alpha = 2.5$ mrad/turn with no hysteresis.

During the years 2001 – 2004, the photon detection with RICH1 has been performed by large-size Multi-Wire Proportional Chambers (MWPC) equipped with caesium iodide (CsI) photocathodes [21]. Some characteristic features of these photon detectors and of its associate front-end read-out electronics limits the RICH1 performance in the COMPASS environment, reducing the efficiency in particular for particles scattered at small angles and introducing some dead-time in the experiment data acquisition. To overcome these limitations, the photon detection system of the RICH1 counter has partially been upgraded [22].

Since 2006 inner part of the detection area is instrumented with a detec-

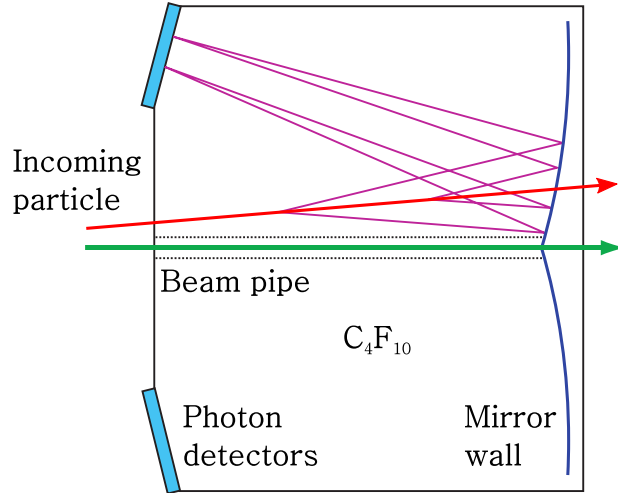


Figure 2.5: Working principle of the COMPASS RICH1 detector. Cherenkov photons emitted by the incoming particle in the radiator gas are reflected by two spherical mirror surfaces towards the photon detection chambers [8].

tion system based on MultiAnode PhotoMultiplier Tubes (MAPMT) connected to a new front-end read-out electronics. The PMTs are coupled to individual telescopes of fused silica lenses (a prismatic field lens followed by a concentrator lens) to enlarge the effective active area of the photon detectors. The inner part (25 % of the detection area) is more populated by the uncorrelated background noise compared to the peripheral region of the photon detection area. The uncorrelated background signals related to the long integration time of the front-end read-out electronics can be rejected by pushed time resolution. As a result of the upgrade, the part with MAPMTs allows to detect about four time more Cherenkov photons. More details about the RICH1 upgrade can be found also in [23]. Using two different photon detector types employing also different photoconverters results in the detection of photons in two different wavelength regions, which must be considered in the software analysis.

Photon hits are measured on the photon detector plane, together with either time information for the MAPMTs or signal amplitude for the MWPCs to reduce background (electronic noise, uncorrelated photons). A photon converted in MWPCs can induce a signal on more than one adjacent MWPC pad. In order to achieve better determination of the photon impact, a clustering procedure is used, giving as impact position the centre of mass of



Figure 2.6: Mirror holder, which allows only angular adjustment of mirror unit around two orthogonal axes.

the hits involved. Figure 2.7 shows an example of a typical RICH1 event, where individual rings correspond to individual cones of light coming from the particles crossing the detector RICH1. The Cherenkov photons, emitted uniformly along the particle path inside the radiator, are characterized by the same Cherenkov angle θ_{ch} (neglecting chromatic aberration) and by different azimuthal angles φ along the track. The Cherenkov ring radius r_c depends on the Cherenkov angle according to the equation

$$r_c = \frac{R}{2} \cdot \tan(\theta_{ch}), \quad (2.2)$$

where R stands for radius of curvature of the spherical mirror. The trajectory of a photon can be reconstructed from its position on the detector plane and from its emission point [24]. Since the emission point of the photon along the particle trajectory is not known, the middle point of the particle track is taken. The emission point is considered to be the same for all the photons from the pattern, i.e. the ring. The reconstructed photons are then defined by their angles given in the particle reference system. The coordinate system is defined with the z-axis along the particle trajectory and the x-axis lying in the particle plane, namely the plane including the particle trajectory and from its virtual RICH1 mirror reflection. For the angle reconstruction, the detailed geometry of the RICH1 is used, including the measured radii and the positions of each mirror element and the

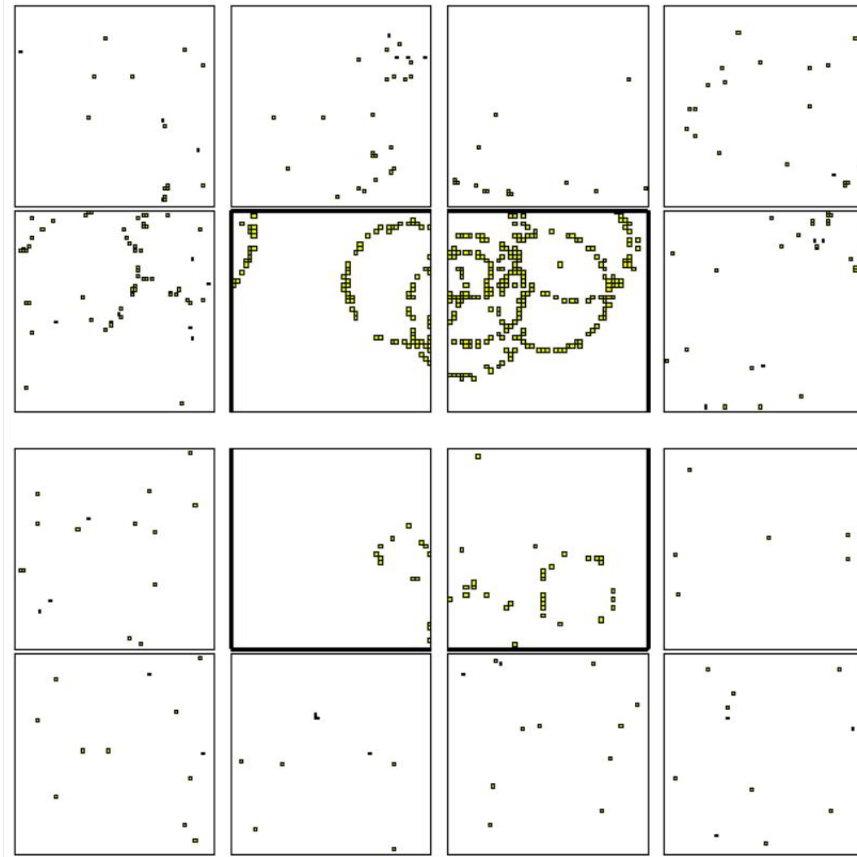


Figure 2.7: RICH1: A typical event display, where squares represent photon detection frames. The central part of the detectors is equipped with MAPMTs, the outer part with MWPCs. More photons per ring are detected in the MAPMT part [22].

fused silica window separating the radiator from the detectors. Then, for each particle, the Cherenkov angle θ_{ch} is determined from the reconstructed photon polar angles $\theta_{ph,i}$ belonging to the ring. The Cherenkov angle is the average value of all the single photon angles [25]:

$$\theta_{ch} = \sum_{i=1}^N \frac{\theta_{ph,i}}{N}, \quad (2.3)$$

where N is the number of detected photons. The single ring resolution is $\sigma_{ring} = \sigma_{\theta}/\sqrt{N}$, σ_{θ} is the single photon resolution. The expected maximum Cherenkov angle is about 55 mrad for C_4F_{10} . This is the Cherenkov angle for

photons at saturation, i.e. the photons, produced by a particle with $u/c \rightarrow 1$, detected in the outer part of the RICH. The Cherenkov angle for photons produced in the inner part of the RICH is smaller. Two algorithms are used providing two estimates of the angle: the likelihood-based method and the ring reconstruction method. More details about software package developed to perform RICH1 data reduction, pattern (ring) recognition and particle identification as well as the algorithms implemented and the detector RICH1 characterization and performance can be found in [26].

In a correlation plot of θ_{ch} as a function of φ , the photons belonging to the particle distribute around a precise value of θ_{ch} uniformly in φ . The ring recognition algorithm is based on the search of a peak in the θ_{ch} distribution using specific look-up window with error $2\sigma_\theta$. The error σ_θ of the photon position resolution depends on the photon detector type. The pad sizes of the photon detector lead to geometrical contribution of ≈ 1 mrad for MAPMTs and ≈ 0.7 mrad for MWPCs. Considering dispersion due to chromaticity of the lens telescope in front of the MAPMTs, the total error from the photon position measurement is 1.6 mrad. The chromatic dispersion, caused by different sensitivity of the detectors to the photon wavelengths, adds 0.9 mrad for MAPMTs and 0.6 mrad for MWPCs. Reduced resolution of MAPMTs compared to MWPCs is compensated by higher number of photons detected by the MAPMTs. The particle trajectory reconstruction and the dispersion that comes from the mirror imperfections and the mirror alignment errors contribute with the error of 0.6 mrad for the central region and 1.3 mrad in the peripheral region.

Error in the mirrors alignment can be caused by initial installation and it can vary with temperature changes (material dilatation), pressure changes or mechanical vibrations. To eliminate the alignment error, and consequently to minimize the angular resolution of the RICH1 detector, it is suitable to monitor the alignment of individual mirrors and to set appropriate corrections. The overview of methods which are used to monitor the alignments of mirrors in RICH detectors is discussed in the next chapter.

3. State-of-the-Art of the mirror misalignment measurement

This Chapter describes the current state-of-the-art of the large mirror alignment control in RICH type detectors. Four basic different methods used for the mirrors alignment will be presented.

3.1 Theodolite in autocollimation mode

The basic alignment method for setting the mirror segments of the RICH detectors in the correct positions is a measurement with the theodolite in autocollimation mode. The method allows absolute mirror alignments with at least 0.1 mrad relative accuracy [19, 27]. Since the surveying procedure requires direct access to the mirror setup, it can be performed only when the COMPASS spectrometer is not in data taking period. The access in the RICH vessel is needed for several days.

As the loci of the centres of the spherical surfaces are outside the vessel volume, the alignment procedure is as following: The coordinates of the two sphere centres are known in the vessel reference frame coordinate system. The coordinates of a theodolite are measured with respect to the same reference frame while its axis is oriented along the straight line joining the centres of the sphere and the theodolite, i.e. reference line. The theodolite is placed in front of each mirror segment. If the mirror is perfectly aligned, the normal to the mirror surface at the intersection point with the reference line lies exactly along the reference line. If it is not aligned as it can be seen in Figure 3.1, the normal and the reference line are at an angle, and the image of a reticle reflected from the mirror is displaced. Then, the theodolite is rotated to make the two lines coincide (a cross hair on the theodolite objective and its image from the mirror are seen superimposed).

The precision of the measured angle is strongly dependent on knowledge

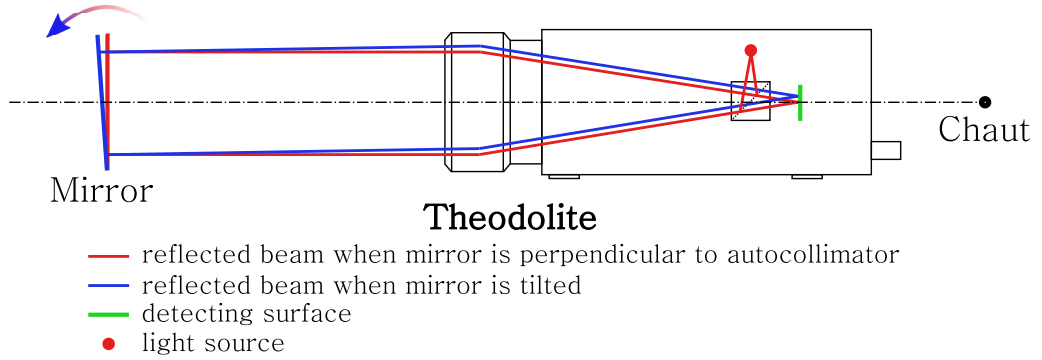


Figure 3.1: Theodolite in autocollimation mode - the effect of mirror misalignment is presented. If the mirror is not aligned, the normal (blue line) and the reference line (red line) are at an angle. The image of a reticle on the detecting surface reflected from the mirror (green line) is displaced compared to the reference value.

of the exact position of the theodolite itself. To minimize vibrations during the measurement special scaffolding is built inside the vessel and removed at the end of the alignment procedure. More detailed information about the theodolite measurement in autocollimation mode can be found in [28, 29].

3.2 Alignment of the optical system with data

Another mirror position calibration method is used for the optical system of the HERA-B RICH [30]. The mirror position calibration method [31] based on reconstructed tracks from the data recorded by the HERA-B spectrometer. This method can be used only with high-energetic particles ($u/c \rightarrow 1$), for which the Cherenkov angles can be calculated in advance.

The principle is presented in (Figure 3.2). The Cherenkov ring is created by Cherenkov photons at the photon detector plane. Its diameter and position correspond to the direction of a particle crossing the radiator. If the mirror segments are misaligned, the center of the ring C' will not coincide with the expected center C . The expected center is determined by the direction vector of the charged particle reflected from the mirrors in ideal positions. The ring center displacement is given by the parameters a and b . Any misalignment in the mirror segments with respect to the photon detectors can be calculated by measuring the difference between two Cherenkov angles, the reconstructed angle θ_0 and the expected angle θ_{ch} (calculated for

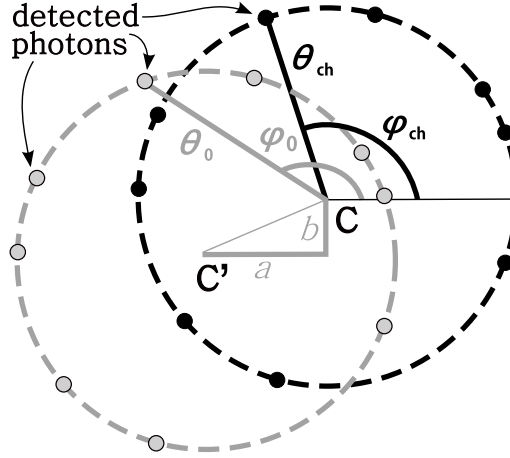


Figure 3.2: Cherenkov rings - the mirror misalignment reconstruction for HERA-b. The point C stands for the expected position of the ring center given by the particle trajectory, and C' is the actually measured center of the ring. The Cherenkov angles θ_{ch} and θ_0 and their azimuth angles φ_{ch} and φ_0 [31].

saturated particles), as a function of the reconstructed azimuthal Cherenkov angle φ_0 :

$$\theta_{ch} - \theta_0 = a \cos(\varphi_0) + b \sin(\varphi_0), \quad (3.1)$$

where, in the case of one mirror wall, coefficients a and b correspond directly to the misalignment of individual mirrors.

This method requires large statistics (thousands of events) [31]. Moreover, only photons reflected by the investigated mirror segment can be used. After reconstruction of θ_0 and φ_0 for a given measured photon, the mirror segment on which the photon was reflected is determined in the following way: Two photons propagated through the optical system, one generated at the beginning of the radiator and the other at the end, both at the measured values of θ_0 and φ_0 . The scheme of the procedure is shown in (Figure 3.3). If both of these photons are reflected from the same mirror then the initial measured photon is declared unambiguous, and only such photons are used for the alignment.

The resolution of 0.2 mrad can be achieved with this type of alignment technique [32]. Similar method is applied also in the COMPASS RICH1 [33]. For the HERA-b RICH detector and for the RICH2 detector at the LHCb experiment [34] the calculation is even more complicated since two mirror

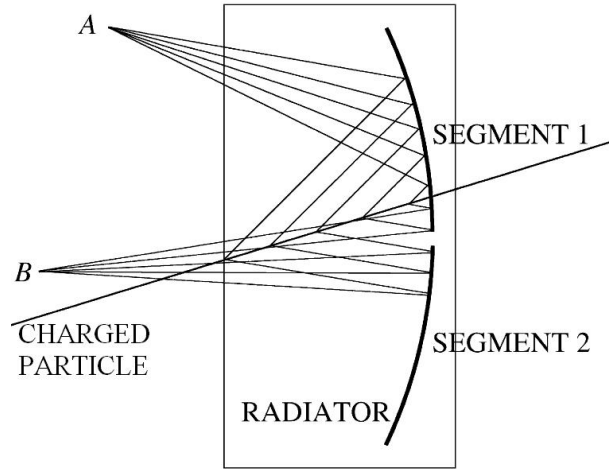


Figure 3.3: Two photons are considered to propagate through the optical system, one generated at the beginning of the radiator and the other at the end. The photon detected in the point A is unambiguous since it is reflected only on the mirror segment 1. Photon detected in the point B could be reflected by both mirror segments. Only unambiguous photons are used for the alignment procedure [31].

walls are used in the detectors. For the set of two mirror walls, coefficients a and b in the Eq. 3.1 express combined effect of the displacement of mirror pair segments. To calculate misalignment of individual segments in a pair a reference mirror has to be chosen with respect to which the other segments will be aligned. Due to the fact that one needs to align the two sets of mirrors simultaneously in combination with large statistic demands, it is impossible to monitor the alignment constants in real time, while the detector is taking data.

3.3 Laser Alignment Monitoring System for the RICH

For RICH2 detector at the LHCb experiment, LAMS (Laser Alignment Monitoring System) has been installed [35,36]. It is a complementary alignment method to the alignment of the optical system with data discussed in previous section (Sec. 3.2). Figure 3.4 presents a basic scheme of the LAMS. It is quite space demanding, it consists of laser source, beam-splitter, focus-

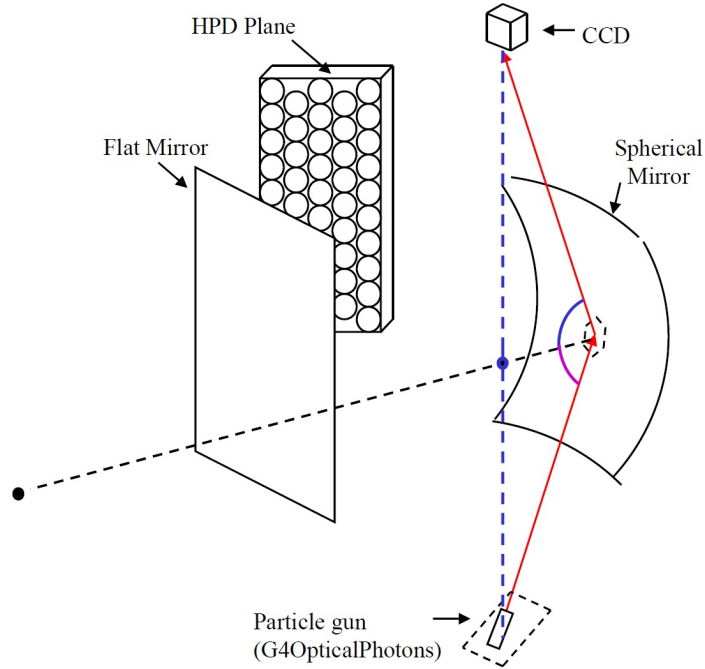


Figure 3.4: Laser Alignment Monitoring System for the RICH. The particle gun provides set of two beams, both are scanned on the same CCD plane. First beam is reflected by the mirror segment and the second one, reference beam, is heading directly to the CCD plane. [35]

ing units, optical fibres and a CCD camera. Thus only selected mirrors (4 spherical and 4 flat per side) are monitored. A laser with an optical fibre coupling system delivers light to 16 fibres. Each fibre has a focusing unit at its end and it is focused onto a mirror segment. The beam-splitter provides a reference beam for each fibre. Both beams are scanned by the same CCD camera generating two spots on the CCD plane.

The coordinates differences of the spots positions $(\Delta x, \Delta y)$ correspond to the movement of selected mirror segment according to the set of equations:

$$\begin{aligned}\Delta\gamma_x &= A_{11}\Delta x + A_{12}\Delta y \\ \Delta\gamma_y &= A_{21}\Delta x + A_{22}\Delta y,\end{aligned}\tag{3.2}$$

where $\Delta\gamma_x$ and $\Delta\gamma_y$ are the changes in rotational angles and A_{ij} are the coefficients of the transformation matrix. A_{ij} were obtained using the simulation of the system in GEANT4 (GEometry ANd Tracking) software, the toolkit for the simulation of the passage of particles through matter using

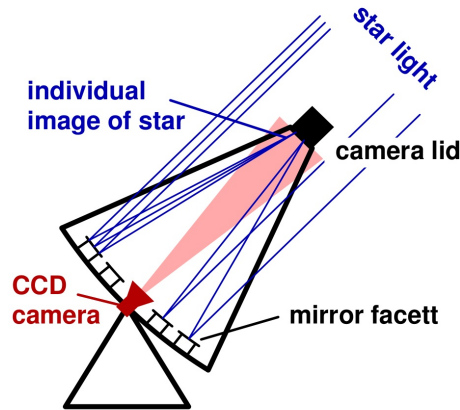


Figure 3.5: Telescope mirror alignment technique with a source at infinite distance. The telescope is directed towards a star whereupon all mirror facets generate individual images of the star in the focal plane. This is observed by a CCD camera viewing the lid of the PMT camera which acts as a screen [38].

Monte Carlo methods. In such a way, the mirrors can be aligned to an accuracy of 0.1 mrad.

3.4 Mirror alignment for Cherenkov Telescopes

The last of the mirror alignment methods, that will be introduced in the Chapter, is used for Cherenkov telescopes. The method is presented on the reflector of an imaging atmospheric Cherenkov telescope (IACT) [37]. The telescope consists of an array of mirrors mounted on a large frame. The challenge of such reflector is to keep several hundreds of mirror facets perfectly aligned to maintain its optical qualities.

This method is very common and employs laser, beamsplitter, a translucent screen and CCD camera [39]. The system is set up on a platform located at twice the focal distance from the center of the reflector along the optical axis. During the procedure, part of the beam is directed towards mirror facet unit and part of the beam is backscattered by the beamsplitter onto the translucent screen for reference purposes. The procedure continues as follows: In the case of correct mirror alignment the laser beam is reflected back by the mirror along its own outgoing path. In the case of misalignment, the reflected beam will be displaced as a point on the screen where it

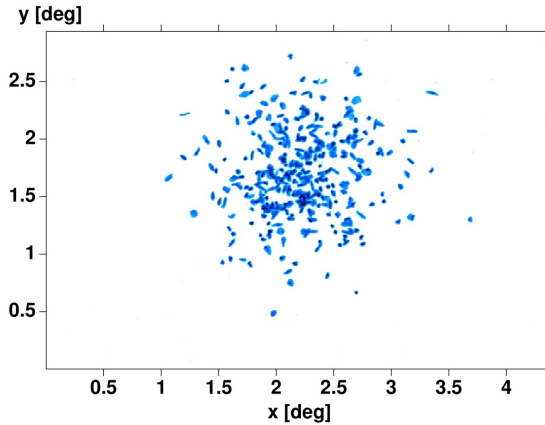


Figure 3.6: Image of a star on the camera lid of RICH telescope mirror alignment technique with source at infinite distance [38]. Each spot corresponds to a reflection off the mirror facet before the alignment of the mirrors.

is compared with its reference point. The difference in the position of the points on the screen corresponds to the value of the mirror misalignment. The CCD camera is used to monitor the screen for an automatic evaluation of the mirror misalignment. The procedure is repeated for each mirror facet. The mirror facets are equipped by actuators. Thus the position of a mirror facet can be remotely controlled. When proper alignment is set, light from a source at infinity should converge to a point at the focal plane of the telescope.

Other method used in RICH telescopes for corrections of the mirror misalignment uses a natural point-like source at infinite distance, i.e. the image of a distant light source at night, usually image of a star [38, 40–43]. The light source is focused by all mirror facets on the closed lid of the photomultiplier camera. The mirror facets generate individual images of the star in the focal plane. This is observed by a CCD camera viewing the lid of the PMT camera which acts as a screen (Figure 3.5).

Figure 3.6 shows an image of a star on the camera lid before the alignment, where each spot corresponds to an individual mirror facet. The mirror facets are aligned correctly when only one spot is seen on the lid by the CCD camera.

3.5 Suitability of the existing methods for the COMPASS RICH1

Now, it will be explained why the existing methods developed for the measurement of the mirrors misalignments in RICH detectors, discussed in previous sections (Sec. 3.1 - Sec. 3.4), have some limitations in the case of usage in the COMPASS RICH1. As it was mentioned in the previous Chapter (particularly Sec. 2.2), the misalignment of mirror elements of the detector significantly affects the detector resolution. The mirror elements must be very accurately aligned to form a single smooth reflecting surface.

In the case of the alignment of the optical system with data collected by the spectrometer (Sec. 3.2) alignment of the reference mirror has to be known precisely in advance. Moreover, a large statistics is needed, hence the information is averaged over a long time intervals. In case of COMPASS RICH-1 detector, not more than about one quarter of the mirrors, those, which are placed in the most populated areas, can be monitored with this approach.

The laser alignment monitoring system (Sec. 3.3) can be adopted to ensure correct alignment of the reference mirror. Because of large number of components needed by the LAMS, the method can be used to monitor only a few mirror segments.

The main disadvantage of the most advanced method - surveying the mirrors with the theodolite (Sec. 3.1) - is the need of direct access to the mirror setup. Thus, the surveying can be performed only when the spectrometer is not in operation mode.

In 2001, the initial alignment of the whole mirror wall of the RICH1 was performed and then remeasured using the autocollimation technique [44–46]. At the end of the measurement, residual misalignments showed a standard deviation of 0.06 mrad. Later, the alignment of selected mirrors was measured several times between the experiment data taking periods, typically once per year. Typically, it takes one day to measure ten mirrors. Misalignments with a random distribution in the range of 0–1.5 mrad used to be observed. The origin of the misalignments detected after the initial alignment procedure is not known yet.

It was obvious that a new complementary method for the online monitoring of the mirror wall segments had been missing. This kind of method was proposed in 2005, it was called Continuous Line Alignment Monitoring method for RICH mirrors (CLAM). The method allows almost real time

monitoring for all the mirrors of the mirror wall. The values of the mirror misalignments can be applied directly to the data measured by the RICH1 detector.

4. CLAM - Online mirror alignment monitoring method

As it was discussed in the previous Chapter, the monitoring of alignment of mirror walls in Cherenkov detectors for particle physics is performed mainly offline (Sec. 3.1) or in a long-time scale (Sec. 3.2) or for selected mirrors only (Sec. 3.3). Almost realtime monitoring for all the mirrors of the mirror wall is not implemented so far. The first proposal of the on-line monitoring method, named Continuous Line Alignment Monitoring method for RICH mirrors (CLAM), was written by Sergio Costa and Jean-Christophe Gayde in 2005 [47]. According to feasibility study which was performed afterward, the production of a prototype started. In 2007 hardware parts of the CLAM were installed in the COMPASS experiment in the RICH1 detector. In this Chapter the proposal for the CLAM will be discussed, particularly the hardware arrangement (Sec. 4.1) and the control system (Sec. 4.2).

4.1 Hardware arrangement

As it was presented in Chapter 2 the mirror wall of the RICH1 detector forms a part of a sphere with known radius. The idea behind the CLAM method is as follows: If adjacent mirror segments are not coherently aligned, the image of an object reflected by these mirrors appears broken, not consistent. Thus, any discontinuity in the image of a rectangular grid of continuous lines corresponds to a relative mirrors misalignment.

The idea of the CLAM method was simulated using the the Persistence of Vision Raytracer (POVRay), a free software package for creating three-dimensional photo realistic pictures [48]. It took into account the RICH-1 geometry and the optical characteristics of the mirrors. The results of the simulations are presented in Figure 4.1. First, a picture of a grid reflected by perfectly aligned mirrors was produced (Fig. 4.1). Later, by defining the

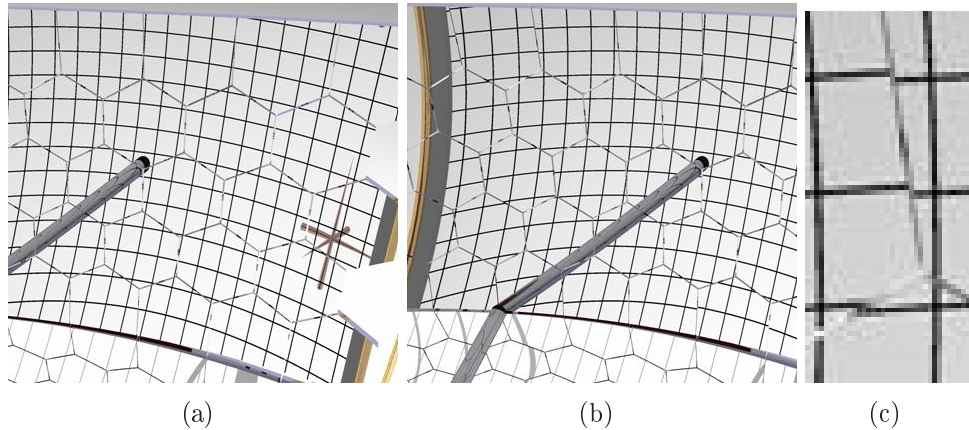


Figure 4.1: The simulation of the basic idea of the CLAM method in POVRay software; (a) Simulated view of the grid reflected by aligned mirrors; (b) Misalignment on selected mirrors up to 1.5 mrad; (c) Detail of the mirror misalignment on selected mirror [47].

given rotation of selected mirror segment, shifts in the grid were generated, as it can be seen in Figure 4.1 and Figure 4.1 in detail. The images (Fig. 4.1 and 4.1) were then subtracted which resulted in a differential image, where the change of mirror rotational angle corresponds linearly to the size of a line shift in the picture Figure 4.2. It is convenient to emphasize that in the simulations using the POVRay the rotations around the horizontal or vertical axis are considered. Extraction of the angle and direction of the mirror misalignment for a combination of horizontal and vertical rotations is not a straightforward task since the pixel shift in the grid image can be different for each line which was not considered in the simulations. The simulations proved the ability to detect mirror misalignments with required resolution of 0.1 mrad, consequently the CLAM components were installed in the RICH1 vessel.

Figure 4.2 shows the basic hardware components set mounted in 2007. It includes four digital cameras for the monitoring of four different segments of the mirror wall, a regular grid of retro-reflective strips and two LEDs for each camera. All the parts of the system were properly chosen to meet the required resolution of mirror misalignment of 0.1 mrad.

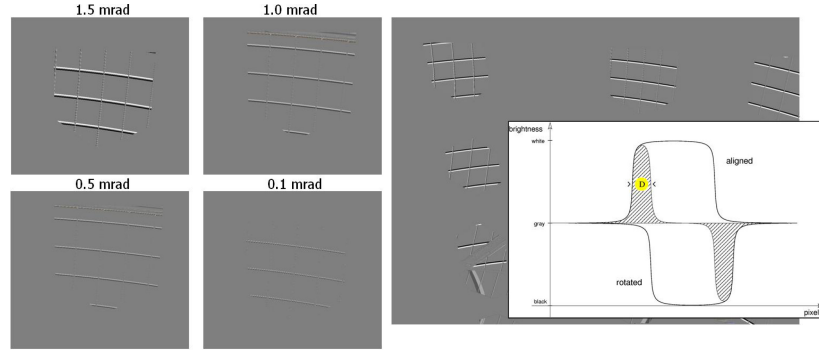


Figure 4.2: CLAM simulation: Differential image between aligned mirrors and some mirrors rotated. The inserted plot shows how the change of mirrors rotational angle corresponds linearly to the size of a line shift in the picture, leaving in their difference white and black zones of width D [47].

4.1.1 Cameras

The cameras, which monitor the four segments of the mirror wall, are CANON EOS 5D [49]. They are placed outside the RICH1 vessel, near to corners of the detector plane, and they monitor the mirror wall through glass windows. The camera positions are distinguished according to Swiss and France mountains location around CERN: Jura-Top (JT), Jura-Bottom (JB), Saleve-Top (ST), Saleve-Bottom (SB). The position of each camera in RICH1 and its inclination in relation to position of the mirror wall and the rectangular grid allows complete overlap only of one mirror, partial overlap of about three mirrors. Vertical overlap is impossible due to the tilt of two parts of the spherical mirror wall (Sec. 2.2).

The full frame CMOS camera sensor has the size of $35.8 \text{ mm} \times 23.9 \text{ mm}$ and the full resolution is 4368×2912 pixels. Size of one pixel is $p = 0.0082 \text{ mm}$. Each camera is equipped with wide-angle lens objective Canon EF 24mm f/2.8.

According to the formula, presented in [47],

$$\alpha_{\min} \approx \frac{p}{f_c} \quad (4.1)$$

where $f_c = 24 \text{ mm}$ is the objective focal length, the smallest observable value of the mirror misalignment is $\alpha_{\min} = 0.34 \text{ mrad}$. The estimated sensitivity of the CLAM method can be improved using the follow-up image processing.

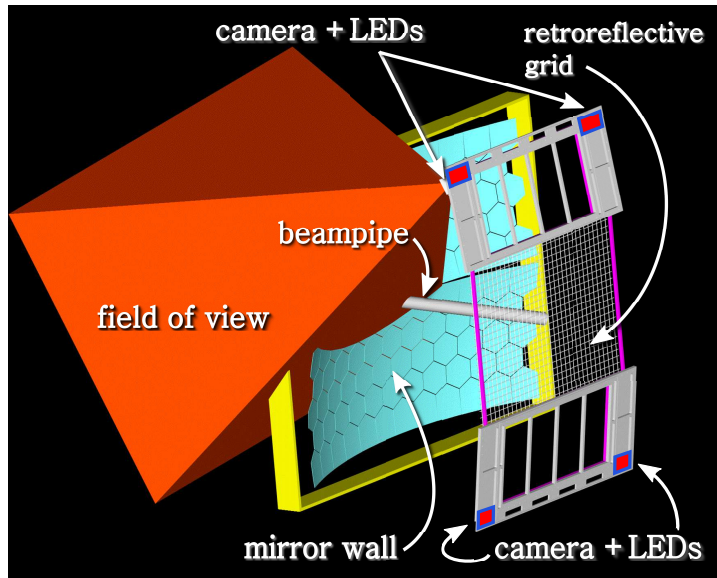


Figure 4.3: The arrangement of CLAM hardware components inside the RICH1 detector.

4.1.2 Retro-reflective grid

The regular grid is created using the retro-reflective strips, which are made from Nikkalite by Nippon Carbide [50]. Retro-reflectors in general are devices that operate by returning light back to the light source along the same light direction. Retro-reflective material Nikkalite is manufactured with a synthetic resin that renders high reflectivity especially at night. The foil of the retro-reflective material is produced using the retro-reflective glass beads, microprisms, or encapsulated lenses sealed onto a fabric or plastic substrate. It is designed mainly for the use on traffic signs, and vehicle license plates.

In the arrangement, designed for the CLAM system, the strips of the width of 10 mm form a square grid with pitch of 100 mm. Circular photogrammetric reflective targets, each 10 mm in diameter, are placed on the strips intersections. To avoid mechanical deformations of the grid, the grid is glued to an aluminum (Al) support. The Al plate is also black anodized to increase the contrast between the strips and the background. The plate is mounted inside the vessel, onto the upstream wall of the RICH1, i.e. opposite wall to the mirror wall. Since the grid is fixed only at the top and the bottom part and it is not stabilized in the middle part, a movement

	Points at the intersections of the grid: 1xxyy
1	grid intersection point
<i>xx</i>	vertical line number starting from the left-bottom intersection
<i>yy</i>	horizontal line number starting from the left-bottom intersection
	Points on the grid support bars (top and bottom): 2iijj
2	grid support bar point
<i>ii</i>	position in prolongation of the grid hole ^a columns, number starting from the left-bottom grid hole ^a
<i>jj</i>	00 for the bottom bars, 21 for the top bars.
	Points on the upstream RICH1 window: 3iijj
3	upstream RICH window point
<i>ii</i>	position of the grid hole ^a column the point belongs, number starting from the left-bottom grid hole ^a
<i>jj</i>	position of the grid hole ^a row the point belongs, number starting from the left-bottom grid hole ^a

^a Empty space between two adjacent retro-reflective stripes

Table 4.1: Photogrammetric targets names explanations [51].

towards the mirror-wall may occur.

Positions of the target points are given in the COMPASS survey coordinate system with the precision of 0.5 mm [51].

According to the Figure 4.4 the three different types of points positions can be distinguished: (i) Points at the intersections of the grid, (ii) Points on the grid support bars, (iii) Points on the upstream RICH1 window. The exact names of individual targets are explained in Table 4.1. Some more optical targets are fixed onto the peripheral frame of the mirror supporting structure to support detection of the camera positions.

The retro-reflective grid is illuminated by high luminosity light emitting diodes (LED) LUXEON-LLXHL-LW6C 5500K HEXAGON produced by Lumileds [52]. A set of two LEDs is placed close to each camera, specifically, they are mounted in the camera holder.

More detailed information about hardware components of the CLAM method and the reasoning of their selection can be found in [53].

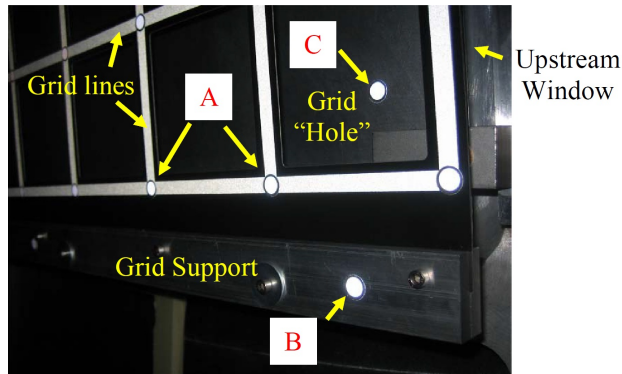


Figure 4.4: The arrangement of photogrammetric targets mounted on the aluminum plate with the retro-reflective grid. Three kinds of photogrammetric targets are defined: A - Points at the intersections of the grid, B - Points on the grid support bars, C - Points on the upstream RICH1 window [51].

4.2 Control system

The control system was proposed and developed by Stefano Takekawa [54]. The scheme of the control system of the CLAM is shown in Figure 4.5. The camera and LEDs are controlled remotely via specially developed LabView by National Instruments application [55] and Canon EOS utility, both installed on dedicated personal computer (PC). The PC is connected over ethernet with a USB hub. Cameras are connected to the USB hub by the USB cable. A portable digital I/O device NI 6501 USB operates relays LD 3021 to control power supplies of individual CLAM components. NI 6501 USB provides 24 digital I/O lines, one 32-bit counter, USB 2.0 bus interface and TTL logic. LD 3021 relays need their own DC power supply and they can be controlled via TTL logic. Interlock signal is used for safety reasons.

The mirror misalignment measurement includes several steps. The MAPMT high voltage power supply is switched off during the image collection remotely to avoid damaging the MAPMT photocathodes by the light emitting diodes. The DC power source is placed inside the experimental zone of the COMPASS spectrometer. When the LabView application is started, interlock signal is sent to the high voltage power supplies to prevent the possibility of having switched on MAPMTs and LEDs at the same time. The application controls individually each LED set and its camera. Unfor-

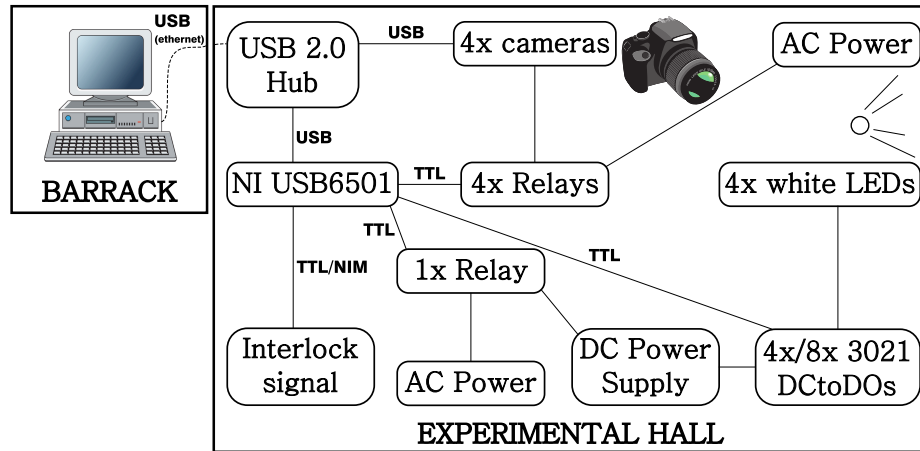


Figure 4.5: CLAM control system. The camera and LEDs are controlled remotely via specially developed application installed on dedicated personal computer (PC). The PC is connected over ethernet with a USB hub. Cameras are connected to the USB hub by the USB cable. A portable digital I/O device NI 6501 USB operates relays LD 3021 to control power supplies of individual CLAM components. NI 6501 USB provides 24 digital I/O lines, one 32-bit counter, USB 2.0 bus interface and TTL logic. LD 3021 relays need their own DC power supply and they can be controlled via TTL logic. Interlock signal is used for safety reasons.

Unfortunately, due to software limitations it is not possible to operate all cameras in parallel at the same time. Then, the Canon EOS utility to control the camera settings and shooting is started. Before switching on the LEDs, the camera shutter is opened for 20 s to avoid any camera vibrations during the image collection. The time of the exposition can be set in the LabView application by choosing the illumination time interval. After the picture is downloaded to the control PC, the Canon EOS is closed. It takes about five minutes for one camera to acquire a picture. The same procedure is repeated for all the cameras. When all pictures are collected, the control applications are switched off, the interlock signal is released and the MAPMTs might be turned on again.

The output of data collection can be seen in Figure 4.6. For the sake of clarity the picture colors are inverted. The picture was taken by Jura-Top camera. Some features of the CLAM can be seen on the photograph. The photogrammetry targets are mounted on the mirror wall frame. They are used to calculate the position of the camera. Shift of the grid lines in the

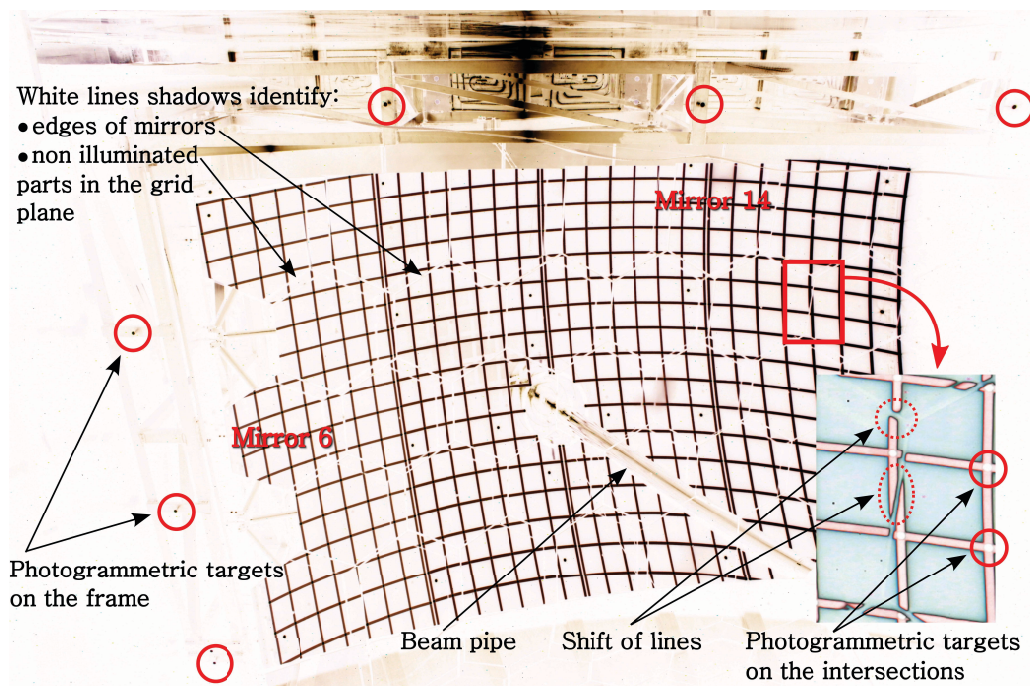


Figure 4.6: Example of a picture collected by one of the CLAM camera. To calculate the position of the camera, seven photogrammetric targets on the mirror wall frame are used. Every mirror is labeled. In detail, shift of grid lines is shown indicating the mirrors rotation.

mirror is shown in detail. Size of the shift indicates the mirror misalignment.

4.3 Summary

The processing of the images, obtained with the CLAM system, and further extracting of appropriate information is discussed within next Chapters of this Thesis. Two approaches are considered when one needs to evaluate mirrors misalignments - *relative* and *absolute measurement*. During the *relative measurement*, the positions of the grid lines reflected by the mirrors are evaluated from images taken at different times. The first image serves as a reference. Then, the other images are subtracted from the reference one. Consequently the change of mirror rotation is indicated in the subtracted image by arised line. Eventually, one could compare each mirror with its neighboring mirrors using just one picture. This would work on the

assumption that surrounding mirrors are perfectly aligned. Unfortunately, several mirrors were misaligned since the beginning when the CLAM data collection started [45].

The position of the mirror wall is given by its center of curvature. If all the mirrors are aligned, all their centers of curvature would be focused in the same point, i.e. the center of curvature of the whole mirror wall. The so called *absolute measurement* method is aimed at the measurement and calculation of the center of curvature of each mirror segment of the RICH1 mirror wall.

5. CLAM - Relative measurement

This Chapter introduces the *relative measurement* of the mirror misalignment. There will be given a fundamental mathematical description of image processing techniques to an extent which is necessary for understanding their applications to the shift of lines measurement presented in this Thesis (Sec. 5.3). For more extensive information, the reader should consult literature dedicated to the field of image processing such as in [56–58]. Finally, the resulting measurements of shift of lines corresponding to the mirror misalignment are discussed and summarized in Sec. 5.4.

5.1 Introduction

The mirror wall of the RICH1 detector is split in two parts, where each part is set-up in a way to form a part of a sphere with known radius R and known center of curvature of the sphere C_k . The radius is an identical value for both sphere parts of the mirror wall and obviously, the centers of curvature are different. The primary goal of the CLAM method is to find misalignments of a single mirror with respect to its initial position.

The regular retro-reflective grid (Sec. 4.1.2) is reflected off the mirror wall and on the account, that the mirrors are spherical, the reflection image of the lines taken by the camera (Sec. 4.1.1) will be an image with the conic sections instead of the straight lines. Then, the mirror misalignment is detected as a discontinuity of conics. The proposal for online mirror monitoring, where the mirror misalignment would be given by the shift of conics positions, was presented by Sergio Costa and J.-Ch. Gayde [47]. In the proposal, authors suggest to measure the shift as difference of two images taken at different dates and times.

In the simulations of the CLAM method, presented in Chapter 4, the authors considered a misalignment in horizontal or vertical directions, in fact, not their combination. The value of the shift of the conics is given

in pixels and it corresponds to the misalignment of investigated mirror. The misalignment can be expressed by means of horizontal and vertical tilt angles, ϕ and ϑ , respectively.

It should be noted, that according to the images, which were taken after the CLAM had been installed, the discontinuities were noticeable already at the beginning of the tests of the CLAM system before the COMPASS run in 2007.

5.2 Calibration of the method

In laboratory conditions, an activity to find a relationship between the shift of conics in the image in horizontal and vertical directions, *hor* and *ver*, and the two angles, φ and θ , was performed for each single mirror position. The exercises were the main part of the diploma thesis by Marek Švec [53]. During the laboratory testing Marek Švec checked all the 30 possibilities of the relative mirror-camera positions of a RICH1 Jura-Top quadrant. The other quadrants (JB, SB, ST) are symmetric with respect to the JT quadrant.

The laboratory testing set-up was arranged as follows: A laser interferometer was used as a reference measurement instrument. A movable Canon camera holder was mounted in the plane of a rigid frame. Two LED light sources were connected with the camera holder. The retro-reflective grid was placed at the same relative position with respect to the mirror and the camera positions, as it is in the RICH1 vessel. An original COMPASS RICH1 spare mirror was mounted onto a stable holder, which can rotate around 2 axes. The photograph of the part of the laboratory testing set-up can be seen in Figure 5.2(a). The dominant feature of the photograph is apparently the mirror which reflects the regular grid of retro-reflective strips.

The distance and rotation of the camera, relative to the mirror position, was adjusted using a laser handhold distance meter. The final mirror position was adjusted by the comparison between the picture taken in the laboratory and the picture taken in the RICH1 vessel using the CLAM camera: The mirror images had to appear at the same positions in both pictures.

This study had provided the calibration parameters for the image shift, which can be expressed as a function of the mirror tilt angle. Of course, this calibration differs for each single mirror. For that reason all the possible relative positions had to be taken into account. The calibration parameters

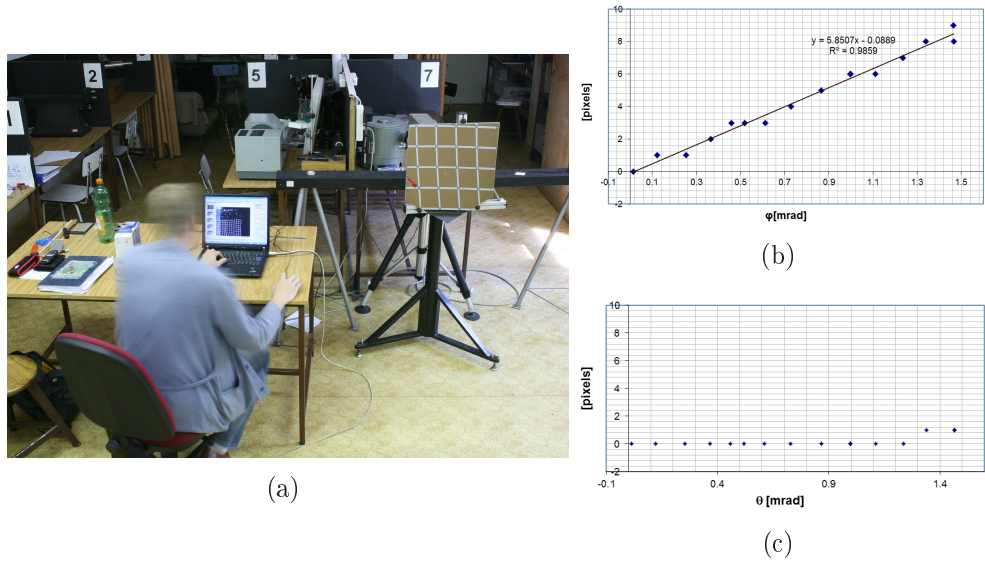


Figure 5.1: (a) Picture taken by CLAM camera during laboratory measurements. Relative position and rotation of the mirror in the picture and camera corresponds to the mirror MT20 placed in the Jura-Top part of the mirror-wall; The two plots (b), (c) correspond to mirror movement in horizontal direction. It is seen that slight movement in vertical direction is present too [53].

were obtained as follows: The mirror was tilted horizontally and vertically in small steps of tenth of a mrad. For each orientation of the mirror, pictures were taken and the tilt angle was simultaneously measured with a very high accuracy (better than 0.005 mrad) using a laser interferometer (Figure 5.2(b) and 5.2(c)). As a result, the shift of the grid lines in the horizontal and vertical directions in the image depends on the tilt angles almost linearly, especially for a small tilt:

$$\begin{bmatrix} hor \\ ver \end{bmatrix} = \begin{bmatrix} k_{11} & k_{12} \\ k_{21} & k_{22} \end{bmatrix} \begin{bmatrix} \varphi \\ \theta \end{bmatrix} \quad (5.1)$$

The coefficients k_{ij} are the calibration parameters and are given in pixels per mrad. They were calculated from 10 – 15 photogrammetric targets positions in image for every mirror orientation. A set of calibration matrices was obtained, each matrix related to each mirror. Then, it is possible to determine the relative tilt of each mirror using the calibration matrices.

Basic description of image processing methods used to process the rel-

ative measurement performed in the laboratory is presented in the next Section.

5.3 Image processing

In accordance with the CLAM proposal, which was briefly sketched in Chapter 4, the task to find the grid lines in the image and evaluate the relative change of their position required a solution.

Two basic methods were used to process the relative measurements - Mathematical morphology and Hough transform. Mathematical morphology was used to remove spurious objects that do not contribute to the evaluation. The Hough transform was used to detect the grid lines.

Every picture taken by a digital camera is a numeric representation of a two-dimensional raster image. It is a dot matrix of the data structure representing the image. In fact, it is a grid of pixels which are, as well known, the smallest controllable elements of a digital image. Individual pixels are represented by their position within the image coordinate system and by their colors. In our case, the color image system is represented by three color components - red, green and blue (RGB color model). According to the Standard ITU-R Recommendation BT.601 [59], a greyscale image can be created from an original RGB color model by weighted sums:

$$GreyPixel = 0.2989 \cdot R + 0.5870 \cdot G + 0.1140 \cdot B, \quad (5.2)$$

where R, G and B are the intensity values of each color component - red, green and blue, respectively. As a result, each pixel of the greyscale image is given as a single intensity value, i.e. image in which colors are shades of gray.

5.3.1 Mathematical morphology

Mathematical morphology is based on the algebra of non-linear operators operating on object shape [56, 60]. In the field of image processing, it is based on probing an image with a structuring element and either filtering or quantifying the image. We can then derive structural object informations from the transformed image. The primary morphological operations are erosion, dilation, opening and closing. They can be applied for binary and gray-scale images. The erosion of an image A by the structuring element B

is denoted by:

$$A \ominus B = \{x : B_x \subset A\}, \quad (5.3)$$

where B_x is the translation of B by the vector x . In other words, when the structuring element fits inside the image, the scanning position is marked. The erosion has a shrinking effect, eliminating small extrusions in the object. The dilation is complement method to the erosion operation. Contrary to erosion it extends the objects in the image, filling in small intrusions into the image. Formally it is defined by:

$$A \oplus B = \bigcup_{a \in A} B_a, \quad (5.4)$$

where a is set of points from the set A . Both operations can be used to find contours of objects in the image very effectively. This can be achieved by subtracting an original image of its dilated version, eroded image from the original image or eroded image from dilated image.

Other two basic methods are opening and closing. The opening of an image by a structuring element B is the union of all the elements that fit inside the image. It can be defined as an erosion followed by a dilation:

$$A \circ B = (A \ominus B) \oplus B. \quad (5.5)$$

The closing is complementary to the opening and it is defined by:

$$A \bullet B = (A \oplus B) \ominus B. \quad (5.6)$$

An interesting property of the opening/closing is that only first operation affects the result, a repeated application of opening/closing has no further effect on the result. The morphology operations mentioned so far are usually used to eliminate small objects (noise in the background) in the image. The opening and closing are much finer operations than the erosion and dilation, they preserve the global shape of investigated object much better.

In the algorithm for the relative measurement processing, a morphology operation called skeletonization was used as well. Skeletonization is a process for reducing foreground regions in a binary image to a skeletal remnant that largely preserves the extent and connectivity of the original region while throwing away most of the original foreground pixels. In other words, it removes pixels on the boundaries of objects but does not allow objects to break apart. The skeleton can be thought as the continuous connecting line

of loci of centers of bi-tangent circles that fit entirely within the foreground region being considered. For a discrete binary image, the skeleton S_A is the union of the skeleton subsets $S_n(A)$, for $n = 0, 1, \dots, N$, where

$$S(A) = \bigcup_{n=0}^{\infty} ((A \ominus nB) - (A \ominus nB) \circ B), \quad (5.7)$$

where $nB = B \oplus B \oplus \dots \oplus B$ and n corresponds to the size of structuring element. One of the example of an image processed using the skeletonization could be seen in Figure 5.2(a) where the image of the retro-reflective grid was processed.

For each mirror measurement, the CLAM picture was segmented. Only the part where the mirror was contained was left for the image processing. During the segmentation of an image one has to look for the position of the grid in the picture. Typically, when looking for objects within an image with known shape and size, a mask with an appropriate shape and size moves along the image. Using the mask one has to look for the correlation between the image and the mask. Unfortunately, the objects within the image are often distorted by noise, their rotations, zoom, etc. In our case, it is advantageous to use the standard Hough transform for the detection of the grid lines, which will be discussed in the next Section.

5.3.2 Hough transform

The method was developed and patented by Paul Hough in 1962 [61]. Originally the Hough transform worked with objects, that can be analytically parametrized. The method was designed specifically to find lines, but in general, it can be used for objects with known shape and size. The Generalised Hough transform was introduced by Dana H. Ballard in 1981 [58]. The modification is based on the principle of template matching, where the object is described with its model and the problem of finding the model position is transformed to a problem of finding the transformation parameter that maps the model in the image. The main advantage of such approach is its robustness, even with presence of imperfect data in the sense of noise presence in the data or that parts of the object in the image are missing.

The Hough transform was used to detect straight lines. Of course, the grid in the image corresponds to a set of general curves, not lines. Finding a straight line is possible only when the image is cropped to smaller parts.

A line is expressed parametrically according to the formula:

$$\rho = x \cos(\alpha) + y \sin(\alpha), \quad (5.8)$$

where ρ and α represent polar coordinates. The symbol ρ is the distance from the origin to the line along a vector perpendicular to the line. The symbol α is the angle of the perpendicular projection from the origin to the line measured in degrees clockwise from the positive x -axis. Since the $\sin(\alpha)$ and $\cos(\alpha)$ are harmonic functions, the range of α can be limited to $-90^\circ \leq \alpha < 90^\circ$. The angle between the line and x -axis is $\alpha + 90^\circ$, measured clockwise with respect to the positive direction of the x -axis.

At the beginning of the search for lines in the image, the so called accumulator matrix is generated. The rows and columns of the matrix correspond to the values of ρ and α , respectively, with predefined step and minimum and maximum values of the defined range. Initially, the value in each cell of the accumulator array is zero. Generally, the dimension of the accumulator array equals the number of unknown parameters. It is obvious that the more complicated object (curve) we have the more parameters is needed and the more computational effort is required.

In the next step, for every non-background point in the image, ρ is calculated for every α using Equation (5.8) and the corresponding accumulator cell is incremented. It depends on the number of pixels belonging to the object in the image how many times the cell will be incremented. Therefore, lines existing in the image will produce large values of the appropriate cell. At the end of the procedure, the peak values in the accumulation array represent potential lines in the input image. During the evaluation, a criterion to decide whether the value contained in a specific block of the accumulation array can be a line or not has to be set. The accuracy of the collinearity of the points lying on a line is dependent on the number of discrete cells in the array.

The main advantage of using the Hough transform lies in the fact that it can overcome missing parts of lines, image noise, etc. Many implementations of the method can be found in public domain and used freely as well.

5.4 Summary and results

During the relative measurement, the positions of the grid lines reflected by the mirrors are evaluated from images taken at different times. The first image serves as a reference. Then, the other images are subtracted from the reference one. It is obvious, that light conditions and camera settings have to be identical for the photographs that are about to be compared. Consequently, the change of mirror rotation is indicated in the subtracted image by arised lines. One of the example of two images subtraction can be seen in Figure 5.2(b). Almost no lines can be seen. It means that the two images almost do not differ from each other and the mirrors have not moved until the second picture was taken.

Unfortunately, several mirrors were misaligned since the beginning when the CLAM data collection started [45]. That means that it is not possible to measure the real mirror positions. On the other hand, the method is fast and helps in fast visual inspections of the behavior of mirrors inside the detector RICH1. This makes the method suitable for monitoring the influence of surrounding effects such as temperature or pressure changes.

In laboratory conditions (Sec. 5.2) the calibration parameters for every mirror of the mirror wall were obtained. It was computed (Eq. 5.1), that depending on the mirror position within the mirror wall, the shift of one pixel corresponds to the mirror rotation of $0.14 \div 0.20$ mrad.

The relative measurement in the RICH1 was performed at different times in 2007: Before the start and during the COMPASS data taking period, which took six months, At changing pressure conditions, ranging from 957 to 968 hPa, At changing temperature conditions, from 21°C to 30°C). The comparison of the taken pictures shows that some mirrors exhibit a slow continuous motion, characterized by a typical tilt of 0.05 mrad in the horizontal and 0.11 mrad in the vertical directions. Some mirrors tend to be in a stable position after 2 months of the run.

In the relative measurement, the possible camera movements had to be considered. As it was already mentioned in Sec. 4.1.2, several photogrammetric targets are fixed onto the peripheral frame of the mirror wall supporting structure. In the hypothesis, that the position of the frame is stable, the shift of the photogrammetric targets in the image indicates movement of the camera. The positions of the target centers were calculated by the circular Hough transform based on the gradient field of an greyscale image with resolution better than 0.5 pixels. The movement of the camera is apparent in the images which were taken before and after filling the ves-

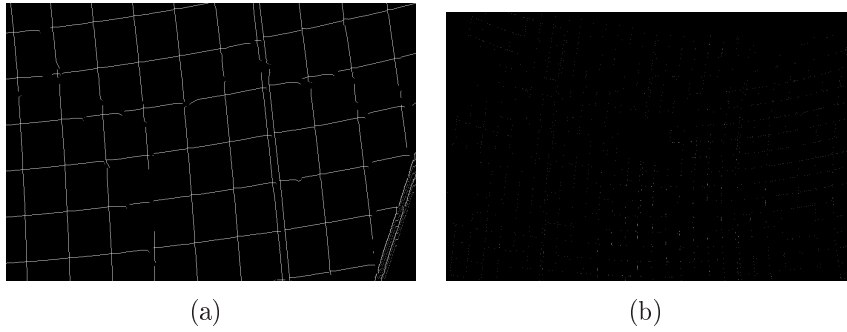


Figure 5.2: (a) Example of image processing method called skeletonization; (b) One of the example of two images subtraction. Almost no lines can be seen. It means that the two images almost do not differ from each other and the mirrors have not moved until the second picture was taken.

sel of the RICH1 detector with the C_4F_{10} . A horizontal movement of the target centers of about 2 pixels was observed, whereas the vertical shift was almost negligible. This indicates that the cameras have been slightly rotated of about 0.6 mrad due to the pressure change. After the RICH1 was filled, the camera position seemed to be stable within the range of the experimental uncertainty (0.25 pixel corresponds to a tilt of 0.035 mrad).

6. CLAM - Absolute method

This Chapter introduces the *absolute measurement* of the mirror misalignment.

In the previous Chapter, the relative measurement was described. It was emphasized that it is possible to measure displacements of mirrors in comparison to a reference picture which defines a reference set of mirrors positions values. On the other hand, the aim of the absolute measurement method is to determine directly the mirror tilt/orientation using only one picture. Every mirror segment is originally defined by its ideal position and its orientation according to the center of curvature C_k of the top or the bottom part of the mirror wall. The coordinates of both centers are given in COMPASS coordinate system. The picture taken by the camera is a result of a projection of the measured scene ($3D \rightarrow 2D$). In the absolute method, the mirror position and its orientation is estimated using only the image of the mirror taken by the camera.

In the following sections, the process to obtain the absolute mirrors misalignments is described. The employed image processing techniques, used in the algorithm for the search for the camera position and mirrors misalignments, are explained in Sec. 6.1.2.2 and Sec. 6.2.1, respectively. Within the Sec. 6.1, the influence of the refractive index of the medium on the accuracy of the absolute method is discussed. For this purpose, the simple 2-dimensional Finite Element Method (FEM) model of the RICH1 vessel was performed (Sec. 6.1.1.1). The main algorithm to determine the mirror misalignments is explained in Sec. 6.2. The influence of optical system parameters is included in the algorithm. These phenomena are discussed in Sec. 6.1.1. Finally, the results of the measurement of mirrors misalignments using the absolute method are summarized and discussed in Sec. 6.3.

6.1 Photogrammetry

The science of obtaining reliable measurements by the processing of photographs is called photogrammetry [62, 63]. As it is given by the American Society for Photogrammetry and Remote Sensing (ASPRS), the photogrammetry is the art, science and technology of obtaining reliable information about physical objects and the environment, through processes of recording, measuring, and interpreting photographic images and patterns of recorded radiant electromagnetic energy and other phenomena [64].

The process to obtain a relationship between the image coordinates and the real world coordinates can be divided into two basic steps: Interior orientation of the camera which provides the camera calibration and the exterior orientation of the camera which provides the position of the camera.

6.1.1 Interior orientation of a camera

A camera can be modelled as a spatial system with its perspective center. The model consists of a planar imaging area (CMOS sensor) and lens. The interior orientation parameters are the principal point, the principal distance and the parameters of functions describing imaging errors.

The principal point H' is defined within an image coordinate system (x'_0, y'_0) . It is the nadir of the camera perspective centre in the image sensor. For standard cameras H' is considered to be equal to the centre of the image.

The principal distance is the normal distance to the perspective centre from the image plane in the negative z -axis direction. The principal distance is considered to be equal to the calibrated focal length f_c of the optical system.

The imaging errors represent aberrations and distortions of the ideal central perspective model. Contrary to optical aberrations that affect radiometric quality of the final image, optical distortions affect the geometric quality of the final image. The effect of radial-symmetric distortion $\Delta r'$ and decentering lens distortion are considered in the algorithm of the absolute measurement.

Once all the parameters are known, i.e. the principal point, the focal length and the effect of optical distortions, the coordinates of an object

within the image can be defined with respect to the perspective centre:

$$x' = \begin{bmatrix} x' \\ y' \\ z' \end{bmatrix} = \begin{bmatrix} x'_p - x'_0 - \Delta x' \\ y'_p - y'_0 - \Delta y' \\ -c \end{bmatrix}, \quad (6.1)$$

where (x'_p, y'_p) are the image coordinates of the object in the image and $(\Delta x', \Delta y')$ are the axis-related correction values for imaging errors. Any distortions are related to the principal point H' .

The radial distortion dominates the imaging errors [65]. It corresponds to refractive index variations of individual camera objective components (lens). In the model of the camera, due to the radial distortion, the light ray changes its direction after passing through the perspective center of the camera. The radial distortion increases with the distance of the principal point. Typically, Brown's model is used to calculate the distortion, according to [66]:

$$\Delta r'_{rad} = r(1 + k_1 r^2 + k_2 r^4 + k_3 r^6 + \dots + k_{n/2} r^n), \quad (6.2)$$

where $r = \sqrt{(x'_p - x'_0)^2 + (y'_p - y'_0)^2}$ is the image radius, an image point distance from the principal point. The distortion is especially dominated by the first term and it has also been found that too high order, included in the computations, may cause a numerical instability [67–69]. Alternatively, the following polynomial can be used:

$$\Delta r'_{rad} = A_1 r(r^2 - r_0^2) + A_2 r(r^4 - r_0^4) + A_3 r(r^6 - r_0^6), \quad (6.3)$$

where r_0 is set in a way that minimal and maximal distortion values are similar with respect to the complete image format. Finally, the image coordinates can be corrected using the following formulas:

$$\Delta x'_{rad} = x' \frac{\Delta r'_{rad}}{r'} \quad (6.4a)$$

$$\Delta y'_{rad} = y' \frac{\Delta r'_{rad}}{r'} \quad (6.4b)$$

where the x', y' are the corrected image coordinates.

Next category of distortions, the tangential distortion, is caused by de-centering and misalignment of components of the lens system within the

objective. The tangential distortion is radial-asymmetric. Usually, it occurs mainly in low-cost video systems. It can be compensated by [66]:

$$\begin{bmatrix} \Delta x'_{tan} \\ \Delta y'_{tan} \end{bmatrix} = \begin{bmatrix} r'^2 + 2x'^2 & 2x'y' \\ 2x'y' & r'^2 + 2y'^2 \end{bmatrix} \begin{bmatrix} B_1 \\ B_2 \end{bmatrix}, \quad (6.5)$$

where B_1, B_2 stand for tangential distortion parameters.

The affinity and the shear describe deviations of the image coordinate system with respect to orthogonality and uniform scale of the coordinate axes:

$$\Delta x'_{aff} = C_1 x' + C_2 y' \quad (6.6a)$$

$$\Delta y'_{aff} = 0, \quad (6.6b)$$

Finally, the total correction of the optical system of the camera can be summarized as follows:

$$\Delta x' = \Delta x'_{rad} + \Delta x'_{tan} + \Delta x'_{aff} \quad (6.7a)$$

$$\Delta y' = \Delta y'_{rad} + \Delta y'_{tan} + \Delta y'_{aff} \quad (6.7b)$$

Typically, the correction values are obtained by the self-calibrating bundle adjustment method. In our case, a plate with circular photogrammetry targets placed in well defined regular positions is used. The plate is photographed by the camera from several positions, as it can be seen in Figure 6.1. During imaging the plate should cover whole area of the image sensor. Measured image coordinates and approximately known space coordinates of the targets in the plate are processed by bundle adjustment to give the parameters of the interior orientation of the camera. Commercially available software, AICON 3D Studio [70], is used for the calculation of the interior parameters for all four cameras of the CLAM system.

Table 6.1 summarizes the distortion parameters values of the CLAM cameras. The calibration images were obtained in the air (Figure 6.1). If one takes a look at the interior orientation values of each camera it is obvious, that the distortion parameters are very similar. On the other hand, the focal lengths and the principal points are different. Hence, the optics of the camera objectives seems to be similar, but the mechanics of the cameras varies.

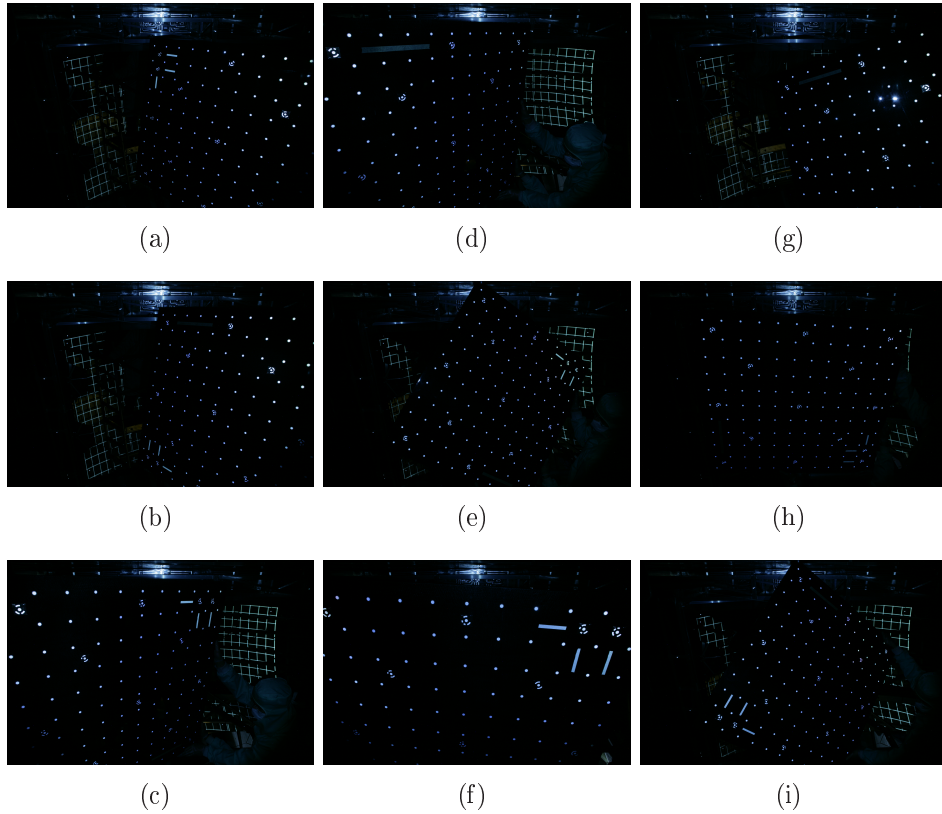


Figure 6.1: Image series example for the camera JT calibration.

It has to be mentioned, that the CLAM cameras are placed outside the RICH1 detector. That means, that the light ray has to go through multiple media. Figure 6.2 shows a simple scheme of the ray path from the radiator C_4F_{10} to the image plane, from the point P_2 to the point P'_0 . First, the cameras are separated from the inner environment by 1 cm thick glass planparallel window. Second, the cameras are placed in air atmosphere, while the RICH1 is filled with the C_4F_{10} , eventually with nitrogen. It can be shown that the planparallel glass plate influences distortion parameters of the optical system [71]. It can be also shown that the planparallel plate negatively influences the quality of resulted image. The effect of dispersion can be calculated using the equation which was presented in [72]. The influence of the glass plate is included in the calibration procedure of the cameras.

If we consider homogeneous and isotropic transmission media, the radial shift $\Delta r'$ in the image plane can be calculated using the Snell's law of

Distortion parameters	JT	ST	JB	SB
r_0 (mm)	13.425	13.425	13.425	13.425
f_c (mm)	-24.0370	-24.1241	-24.0438	-23.9805
x'_0 (mm)	-0.1120730	-0.0727421	-0.3283670	-0.0842206
y'_0 (mm)	0.0073559	-0.0419821	-0.0088308	0.2113350
A_1 (10^{-4})	-1.91122	-1.88703	-1.89387	-1.95049
A_2 (10^{-7})	3.34593	3.22400	3.34447	3.55484
A_3 (10^{-10})	-1.07016	-0.81142	-1.07829	-1.41506
B_1 (10^{-6})	2.28195	-0.64063	-4.05026	-14.16670
B_2 (10^{-5})	-2.09756	-1.53875	-1.60019	1.33112
C_1 (10^{-3})	-1.32099	-1.39376	-1.43297	-1.33767
C_2 (10^{-5})	-6.57227	-4.79107	2.36186	13.3118

Table 6.1: The summary of distortion parameters of the CLAM cameras.

refraction:

$$n_1 \sin \epsilon_1 = n_2 \sin \epsilon_2, \quad (6.8)$$

or an alternative expression:

$$\frac{\tan \epsilon_1}{\tan \epsilon_2} = \sqrt{n^2 + (n^2 - 1) \tan^2 \epsilon_1}, \quad (6.9)$$

where $n = n_2/n_1$ and $n_2 > n_1$. n_i stand for refractive indices of different media and ϵ_1 and ϵ_2 are the angles of reflection. Finally, the radial shift can be calculated using the equation:

$$\Delta r' = r'_0 Z_{rel} \left(1 - \frac{1}{\sqrt{n^2 + (n^2 - 1) \tan^2 \epsilon_1}} \right), \quad (6.10)$$

where $Z_{rel} = (Z_i - Z_0)/Z_i$ and $r'_0 = f_c \cdot \tan \epsilon_1$. Z_0 stands for the distance from the principal point of the camera to the media interface and Z_i stands for the distance from the principal point of the camera to the position of the object. For multiple media with p number of layers, Eq. (6.11) can be expanded as follows:

$$\Delta r' = \frac{r'_0}{Z_i} \left[(Z_i - Z_{01}) - \sum_{l=1}^p \frac{d_l}{\sqrt{N_l^2 + (n_l^2 - 1) \tan^2 \epsilon_1}} \right], \quad (6.11)$$

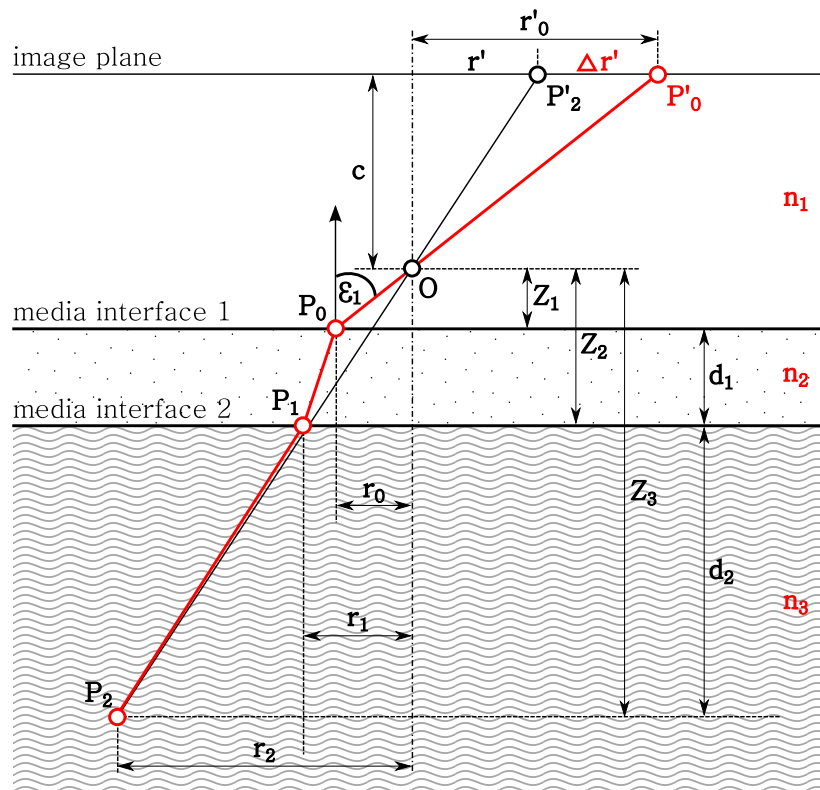


Figure 6.2: Multiple media photogrammetric model. The CLAM cameras are filled with air (n_1), whereas the RICH1 detector is filled with C_4F_{10} (n_3). The cameras are separated from the inner environment by the quartz window (n_2). The point O is the principal point of the camera. The light ray goes from the C_4F_{10} to the image plane and is refracted at the border of each medium with different refractive index according to the Snell's law of refraction.

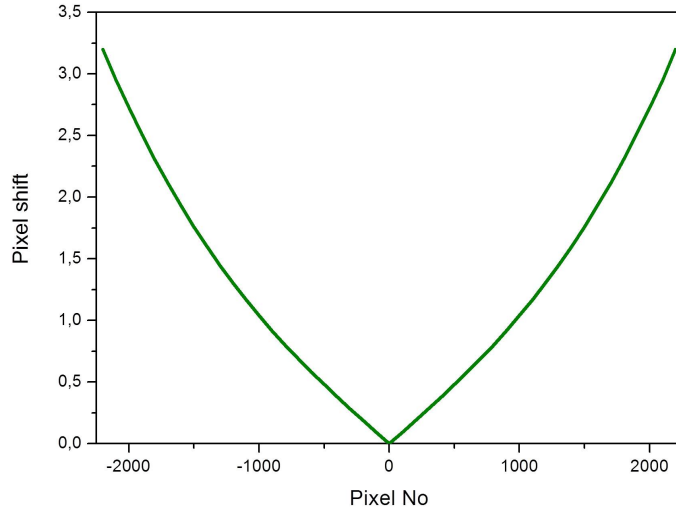


Figure 6.3: Influence of the multiple media environment. CLAM cameras are filled with air, whereas the RICH1 detector is filled with C_4F_{10} . Plot of the pixel shift depending on the path of the light ray through multiple media (Eq. 6.10). It can be seen that the pixel shift increases symmetrically with the distance from the center of the image sensor.

where d_l stands for the distance between two adjacent interfaces and $N_l = n_{l+1}/n_l$ stands for the relative refractive index of two adjacent interfaces.

Generally, before RICH1 is filled with C_4F_{10} ($n = 1.00131$) it contains only nitrogen ($n = 1.0002793$). In out-of-run periods of the COMPASS spectrometer, the RICH1 vessel is filled with air ($n = 1.0002724$). The stated values of the refractive indices, which can be found in [73–77], are valid for wavelength $\lambda = 546.1$ nm and for normal working conditions of the RICH1 detector, i.e. temperature $t = 25^\circ$ C and atmospheric pressure $p_a = 101325$ Pa. Water vapor and oxygen traces are kept below 5 ppm [18]. The change of the gas from air or nitrogen to C_4F_{10} results in maximum radial shift at the edge of the sensor of about 0.0277 mm, when Eq. (6.11) is applied. Size of the pixel of the image sensor is 0.0082 mm [49], thus the radial shift corresponds to $0.0277/0.0082 \approx 3.4$ pixels (Figure 6.3).

Generally, the refractive index of a gaseous radiator depends on many parameters, mainly on the purity of the gas itself, the atmospheric pressure and the local temperature. Therefore, the value of refractive index is time dependent. The refractive index of the gas inside the RICH1 detector vessel is measured only from the data analysis [26]. The gas circulation system

ensures the purity of the gas system. The temperature is measured in five different places inside the vessel and also the pressure can be monitored. Thanks to the gas circulation system of the RICH1, that was installed in July 2009, the inner gas environment of the detector is kept homogeneous. The rate of the circulation is in order of 20 m³/hour [22]. However, the influence of the outer environment should be considered. The change of the ambient temperature or pressure and subsequently of the gas refractive index influences the gas density according to the Gladstone-Dale relationship:

$$\frac{n - 1}{\varrho} = c, \quad (6.12)$$

where ϱ stands for the gas density in g/cm³ and c is the Gladstone-Dale constant, for the gas and given wavelength λ , in m³·kg⁻¹. For the purpose to which extent the environmental phenomena influence the refractive index, the finite element method model was developed and is discussed in the next Section.

6.1.1.1 Finite element method model

The objective of the study presented in this Section is to analyze an influence of various physical phenomena on the refractive index of the gas medium in the vessel. One of the possibility to obtain an approximative solution is to perform a numerical simulation using a finite element method (FEM).

First, in order to see the influence of the filling of the vessel with the C₄F₁₀ it is convenient to develop a realistic 2-dimensional two-phase fluid flow FEM model which would be robust enough to see the changing density of the gas in time (Sec. 6.1.1.1.1). Second, in order to see the changing density of the gas due to the influence of varying temperature around the vessel during the day a FEM model using the heat transfer in liquids is developed (Sec. 6.1.1.1.2).

6.1.1.1.1 FEM model of the filling of the vessel

The geometry of the vessel placed in the system of coordinates is shown in Figure 6.4. The symbols h , w , R and α stand for the height of the vessel, width of the vessel, the radius of the mirror wall and the chamfer angle, respectively, where $h = 5.3$ m, $w = 3.3$ m, $R = 6.6$ m and $\alpha = 0.15$ rad. The vessel has one inlet for the incoming and one outlet for the outgoing gas. The

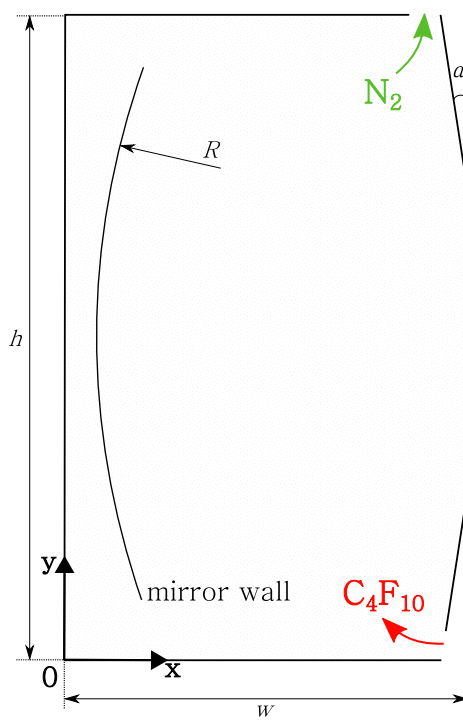


Figure 6.4: Geometry of the 2-D FEM model of the filling of the vessel with the C_4F_{10} . The symbols h , w , R and α stand for the height of the vessel, width of the vessel, the radius of the mirror wall and the chamfer angle, respectively, where $h = 5.3$ m, $w = 3.3$ m, $R = 6.6$ m and $\alpha = 0.15$ rad. The vessel has one inlet for the incoming C_4F_{10} and one outlet for the outgoing N_2 .

normal velocity amplitude of the incoming gas flow is $U_0 = 20 \text{ m}^3 \cdot \text{hour}^{-1}$. At the beginning, i.e. in the time $t = 0$ s, only N_2 is present in the vessel.

To model the flow of two different, immiscible fluids, where the exact position of the media is of interest, the level set method can be used [78]. The level set method tracks the fluid-fluid interface using an auxiliary function on a fixed mesh. This method accounts for differences in the two fluid's densities and viscosities and can include the effect of gravity.

To describe the double phase fluid flow problem the incompressible formulation of the Navier-Stokes equations is used:

$$\varrho \frac{\partial \mathbf{u}}{\partial t} + \varrho (\mathbf{u} \cdot \nabla) \mathbf{u} = \nabla \cdot [-p \mathbf{I} + \mu (\nabla \mathbf{u} + (\nabla \mathbf{u})^T)] + \varrho \mathbf{g}, \quad (6.13)$$

where the divergence of the velocity vector \mathbf{u} is

$$\nabla \cdot \mathbf{u} = 0, \quad (6.14)$$

p is the pressure in Pa, \mathbf{I} is a second-order identity matrix, ϱ is the density of the mixed fluid in $\text{kg}\cdot\text{m}^{-3}$, μ is the dynamic viscosity of the mixed fluid in Pa·s and \mathbf{g} is the gravity vector, where $\mathbf{g} = (0, -9.8066)$ $\text{m}\cdot\text{s}^{-2}$. If the level set method is used to track the interface, it adds the following equation:

$$\frac{\partial \Phi}{\partial t} + \mathbf{u} \cdot \nabla \Phi = \nabla \cdot \left(\epsilon \nabla \Phi - \Phi(1 - \Phi) \frac{\nabla \Phi}{|\nabla \Phi|} \right), \quad (6.15)$$

where Φ is the auxiliary function, called the level set function. Symbol ϵ stands for the parameter controlling interface thickness. Generally, the value of a half of the maximum mesh element size is used for the ϵ [79]. The density is a function of the level set function according to

$$\varrho = \varrho_1 + (\varrho_2 - \varrho_1)\Phi \quad (6.16)$$

and the dynamic viscosity is

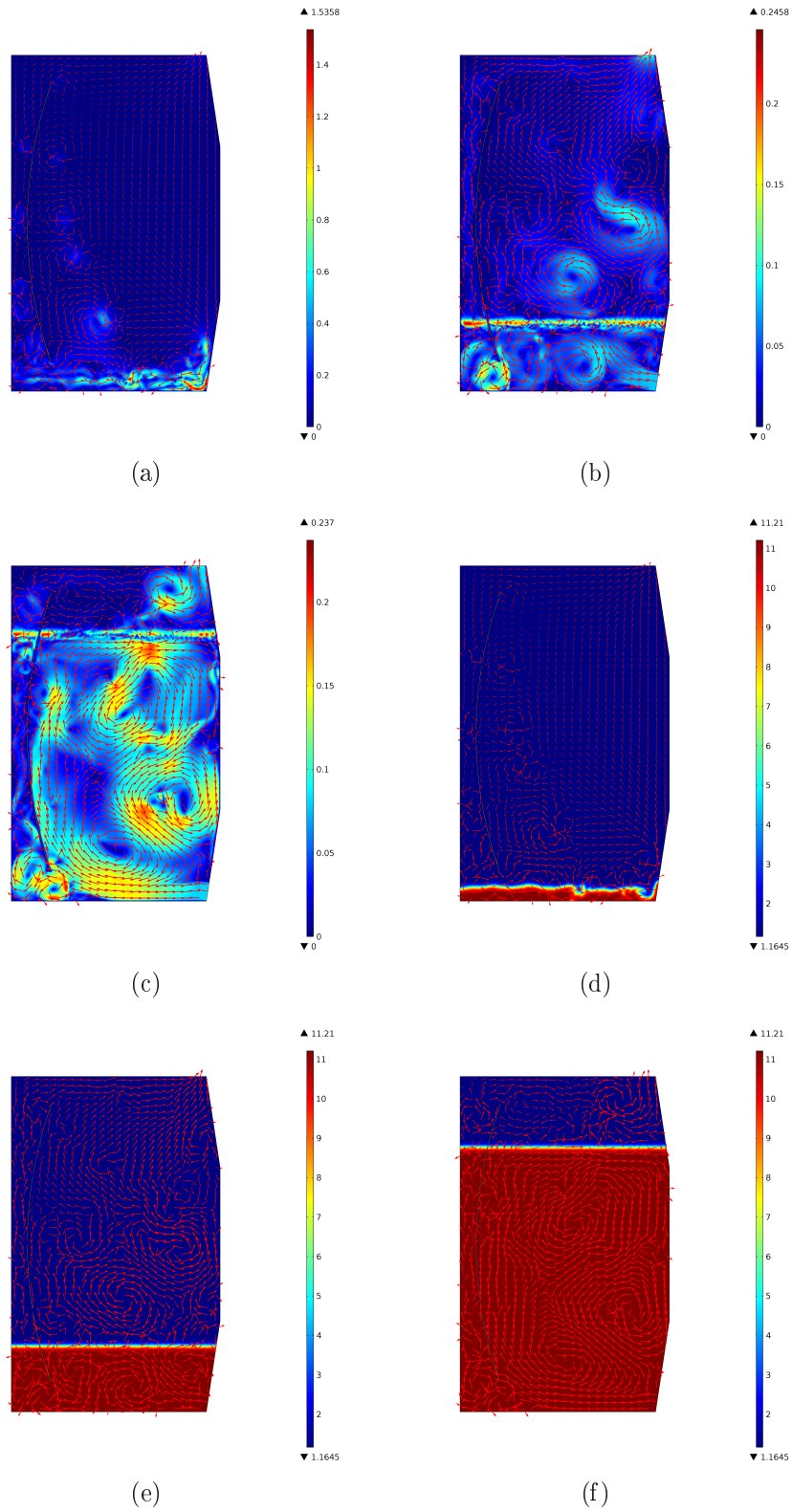
$$\mu = \mu_1 + (\mu_2 - \mu_1)\Phi, \quad (6.17)$$

where ϱ_1 and ϱ_2 are the constant densities of Fluid 1 and Fluid 2, respectively, and μ_1 and μ_2 are the dynamic viscosities of Fluid 1 and Fluid 2, respectively. Here, the Fluid 1 corresponds to the domain with the N_2 and where $\Phi < 0.5$. Fluid 2 corresponds to the domain with the C_4F_{10} and where $\Phi > 0.5$.

The governing equations should be appended by the numerical values of the material parameters and input variables. Isotropic material constants for the nitrogen and perfluorobutane at the temperature $T = 293.15$ K and the pressure $p = 1$ atm, which are required for the two-phase fluid flow analysis are listed in Table 6.2.

The problem for partial differential equations given by Eqs. (6.13), (6.14), (6.15), (6.16) and (6.17) was solved using COMSOL Multiphysics software [79]. The solution primarily yields spatial distributions of the fluid velocity vector \mathbf{u} , the pressure p and the level set function Φ . Secondly, it yields the total fluid density distribution according to the Eq. (6.16). The refractive index of the fluid directly depends on the density value.

The graphical representation of the results can be seen in Figure 6.5. Figures 6.5(a), 6.5(b), 6.5(c) show the fluid flow velocity amplitude distribution in the computed times of 10 s, 150 s, 700 s, respectively, where the



69
 Figure 6.5: Graphical results of the 2-dimensional two-phase fluid flow FEM model. (a), (b), (c) show the fluid flow velocity amplitude distribution in the computed times of 10 s, 150 s, 700 s, respectively, where the color legend stands for the velocity amplitude value in $\text{m}\cdot\text{s}^{-1}$; (d), (e), (f) show the fluid density distribution in the computed times of 10 s, 150 s, 700 s, respectively, where the color legend stands for the density value in $\text{kg}\cdot\text{m}^{-3}$. The red arrows point the direction of the fluid flow velocity.

Material parameter	N ₂	C ₄ F ₁₀	unit
Density	1.1645 ^a	11.2100 [80]	kg·m ⁻³
Dynamic viscosity	1.7436 ^b	1.2190 [80]	10 ⁻⁵ Pa·s
Individual gas constant R_{specific}	296.8 [81]	-	J·kg ⁻¹ ·K ⁻¹

^a Obtained using the Ideal gas law: $\rho_1 = p/(R_{\text{specific}} \cdot T)$

^b Obtained using the temperature dependent polynomial formula [79]:
 $\mu_1 = 1.77230303 \cdot 10^{-6} + 6.27427545 \cdot 10^{-8}T - 3.47278555 \cdot 10^{-11}T^2 + 1.01243201 \cdot 10^{-14}T^3$

Table 6.2: Material parameters of N₂ and C₄F₁₀ used in numerical simulation of two-phase fluid flow.

color legend stands for the velocity amplitude value in m·s⁻¹. Figures 6.5(d), 6.5(e), 6.5(f) show the fluid density distribution in the computed times of 10 s, 150 s, 700 s, respectively, where the color legend stands for the density value in kg·m⁻³. The red arrows point the direction of the fluid flow velocity.

6.1.1.1.2 FEM model of the temperature influence

The density of the gas inside the vessel can be changed not only during the filling but due to the change of ambient temperature or pressure. Here, the example of the FEM model of varying temperature in the course of one day is presented.

The geometry of the vessel placed in the system of coordinates and a boundary condition used in this study are shown in Figure 6.6(a). Only nitrogen is present inside the vessel. Temperature, as a time dependent function, is induced as a boundary condition along the edges of the vessel (blue curve). Red points (1–5) are the representative points at the different places of the vessel where the refractive index will be detected in the simulation. Figure 6.6(b) shows the varying temperature as a function of time in the course of one day (24 hours), given by the Gauss function formula

$$T_{\text{BC}}(t) = T_{\text{min}} + \Delta T e^{-\frac{(t-t_{\text{max}})^2}{2\sigma^2}}, \quad (6.18)$$

where $\Delta T = T_{\text{max}} - T_{\text{min}}$, t_{max} is the time at the T_{max} and standard deviation $\sigma = 4.5$ h. The temperature ranges the interval $T_{\text{min}} - T_{\text{max}} - T_{\text{min}}$ (first warming then cooling down), where $T_{\text{min}} = 15^\circ\text{C}$ and $T_{\text{max}} = 35^\circ$.

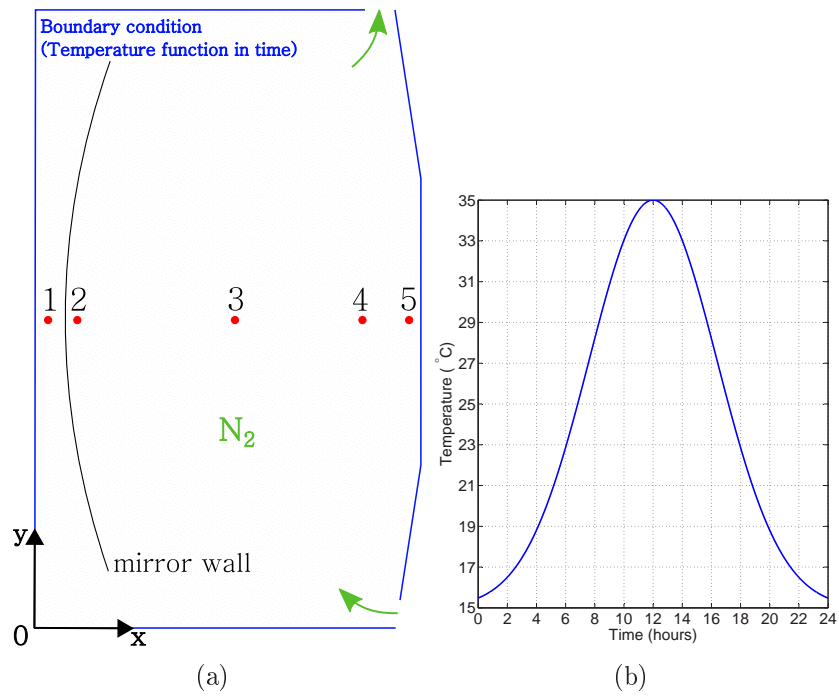


Figure 6.6: (a) Geometry of the 2-D FEM model of varying ambient temperature in the course of one day. Only nitrogen is present inside the vessel. Temperature as a time dependent function is induced as a boundary condition along the edges of the vessel (blue curve). Red points (1 – 5) are the representative points at the different places of the vessel where the refractive index will be detected in the simulation; (b) Varying temperature as a function of time in the course of one day (24 hours). The temperature ranges as $T_{\min} - T_{\max} - T_{\min}$ (first warming then cooling down), where $T_{\min} = 15^{\circ}\text{C}$ and $T_{\max} = 35^{\circ}$.

Material parameter	N ₂	unit
Specific heat capacity at a constant pressure	1.0395 ^a	10 ³ J·kg ⁻¹ ·K ⁻¹
Thermal conductivity	0.0256 ^b	W·m ⁻¹ ·K ⁻¹

^a At the temperature T , obtained using the temperature dependent polynomial formula [79]: $C_p = 1088.22121 - 0.365941919T + 7.88715035 \cdot 10^{-4}T^2 - 3.749223 \cdot 10^{-7}T^3 + 3.17599068 \cdot 10^{-11}T^4$

^b At the temperature T , obtained using the temperature dependent polynomial formula [79]: $k = 3.6969697 \cdot 10^{-4} + 9.74353924 \cdot 10^{-5}T - 4.07587413 \cdot 10^{-8}T^2 + 7.68453768 \cdot 10^{-12}T^3$

Table 6.3: Material parameters of N₂ used in numerical simulation of the heat transfer in the fluid.

The fundamental law governing all heat transfer is the first law of thermodynamics, commonly referred to as the principle of conservation of energy. However, the internal energy is a rather inconvenient quantity to measure and use in simulations [79]. Therefore, the basic law is usually rewritten in terms of the temperature T . For a fluid, the heat equation governing pure conductive heat transfer is:

$$\rho C_p \frac{\partial T}{\partial t} + \nabla \cdot (-k \nabla T) = Q, \quad (6.19)$$

where C_p is the specific heat capacity at a constant pressure in J·kg⁻¹·K⁻¹ and k is the thermal conductivity in W·m⁻¹·K⁻¹. The heat source (or sink) Q (W·m⁻³) is in this simple case equal to zero because there is no added heat source. The initial temperature, i.e. the temperature at time $t = 0$ s, inside the vessel is set to $T_0 = 20^\circ\text{C}$.

Required numerical values of material parameters for nitrogen at the temperature T_0 are listed in Table 6.3.

The problem for partial differential equations given by Eq. (6.19) and the boundary condition given by Eq. (6.18), was solved using COMSOL Multiphysics software [79]. The solution primarily yields spatial distributions of the temperature T in the fluid. Secondly, it yields the heat flux vector direction according to the Fourier's law of heat conduction:

$$\mathbf{q} = -k \nabla T, \quad (6.20)$$

The refractive index of the fluid directly depends on the nitrogen density

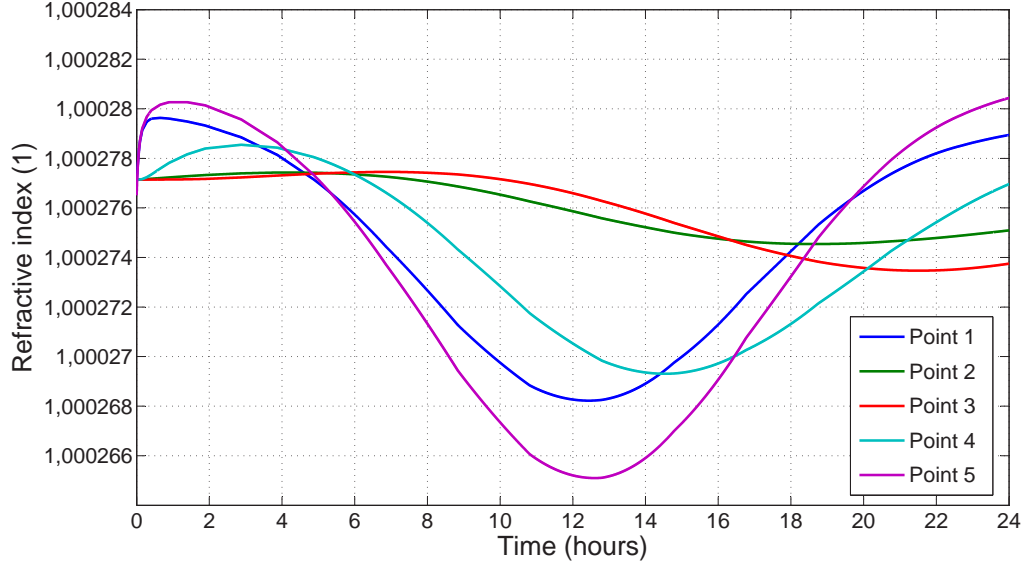


Figure 6.7: Change of the refractive index in the course of time. The values of n were determined in the Points 1 – 5, according to the Figure 6.6. It is obvious that the change of the temperature during the whole day in the range of ΔT does not tremendously affect the value of the refractive index.

ρ which is obtained using the Ideal gas law,

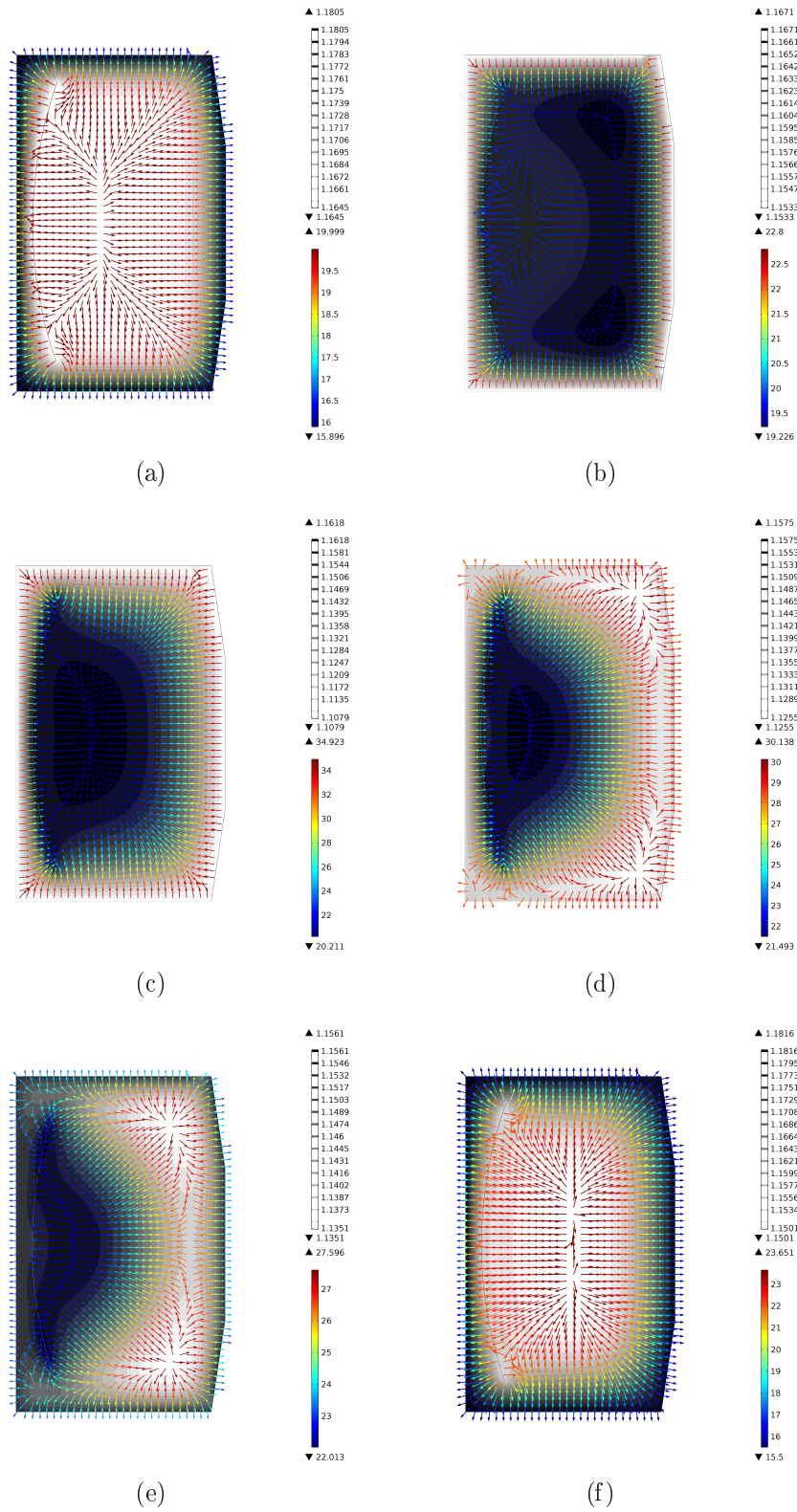
$$\rho = p / (R_{\text{specific}} \cdot T), \quad (6.21)$$

where p is a normal pressure. Then, the refractive index is computed according to the formula (6.12), where the Glad-Stone Dale constant for nitrogen is $c = 2.38 \cdot 10^{-4} \text{ m}^3 \cdot \text{kg}^{-1}$ [82].

Figure 6.8 shows the graphical representation of the resulting nitrogen density computed in times of 1, 6, 12, 16, 18 and 24 hours (Figures 6.8(a), 6.8(b), 6.8(c), 6.8(d), 6.8(e), 6.8(f), respectively). The gray scale legend stands for the fluid density value in $\text{kg} \cdot \text{m}^{-3}$. The colored arrows point the direction of the heat flux and the color itself means the temperature value in degrees of Celsius. It can be seen the warming and the cooling down during the time course.

Finally, the change of the refractive index in the course of time can be seen in Figure 6.7. The values of n were determined in the Points 1 – 5, according to the Figure 6.6. It is obvious that the change of the temperature during the whole day in the range of ΔT does not tremendously affect the value of the refractive index. The maximum change of the refractive index

(1.00026 \rightarrow 1.00028) results in maximum radial shift at the edge of the sensor of about 0.0005 mm, when Eq. (6.11) is applied. Thus the radial shift corresponds to 0.065 pixels.



75
 Figure 6.8: Graphical results of the 2-dimensional heat transfer FEM model. Resulting nitrogen density computed in times of 1, 6, 12, 16, 18 and 24 hours (6.8(a), 6.8(b), 6.8(c), 6.8(d), 6.8(e), 6.8(f)). The gray scale legend stands for the fluid density value in $\text{kg}\cdot\text{m}^{-3}$. The colored arrows point the direction of the heat flux and the color itself means the temperature value in degrees of Celsius. It can be seen the warming and the cooling down during the time course.

6.1.2 Exterior orientation of a camera and collinearity equations

The exterior orientation of a camera defines its location $[X_0, Y_0, Z_0]$ in space and its view direction $[\alpha, \beta, \gamma]$. The viewing directions form the orthogonal rotation matrix $\mathbf{R} = \mathbf{R}_\gamma \mathbf{R}_\beta \mathbf{R}_\alpha$ which corresponds to the rotation about fixed axes in the order α, β, γ . The rotations are:

$$\begin{aligned} \mathbf{R} &= \mathbf{R}_\gamma \mathbf{R}_\beta \mathbf{R}_\alpha = & (6.22) \\ &= \begin{bmatrix} \cos \gamma & -\sin \gamma & 0 \\ \sin \gamma & \cos \gamma & 0 \\ 0 & 0 & 1 \end{bmatrix} \begin{bmatrix} \cos \beta & 0 & \sin \beta \\ 0 & 1 & 0 \\ -\sin \beta & 0 & \cos \beta \end{bmatrix} \begin{bmatrix} 1 & 0 & 0 \\ 1 & \cos \alpha & -\sin \alpha \\ 1 & \sin \alpha & \cos \alpha \end{bmatrix} \end{aligned}$$

A few properties of the matrix \mathbf{R} can be mentioned. Matrix multiplication is not a commutative operation, i.e. the order of the rotation matrices must be kept. Rotation matrices are orthogonal, i.e. $\mathbf{R}^{-1} = \mathbf{R}^T$ which entails $\mathbf{R}\mathbf{R}^T = \mathbf{I}$. The rotation matrix \mathbf{R} is composed of nine coefficients, but only three components are independent.

To calculate the position of CLAM cameras, 26 target points were installed on the mirror wall frame. The targets will be discussed in detail in Sec. 6.1.2.1. The projection of an image point $[x', y', z']$ into a corresponding object point $[X, Y, Z]$ is given by:

$$\begin{bmatrix} X \\ Y \\ Z \end{bmatrix} = \begin{bmatrix} X_0 \\ Y_0 \\ Z_0 \end{bmatrix} + s \begin{bmatrix} r_{11} & r_{12} & r_{13} \\ r_{21} & r_{22} & r_{23} \\ r_{31} & r_{32} & r_{33} \end{bmatrix} \begin{bmatrix} x' \\ y' \\ z' \end{bmatrix} \quad (6.23)$$

The scale factor s is the ratio of object distance to principal point of the camera and focal length of the camera. s varies for each object point. z' corresponds to the negative of objective focal length $-f$. Corrected image coordinates, obtained using the inclusion of interior (Sec. 6.1.1), can be expressed as follow:

$$\begin{bmatrix} x' - x'_0 - \Delta x' \\ y' - y'_0 - \Delta y' \\ z' \end{bmatrix} = \frac{1}{s} \begin{bmatrix} r_{11} & r_{21} & r_{31} \\ r_{12} & r_{22} & r_{32} \\ r_{31} & r_{32} & r_{33} \end{bmatrix} \begin{bmatrix} X - X_0 \\ Y - Y_0 \\ Z - Z_0 \end{bmatrix} \quad (6.24)$$

By doing division of the first and second row of Eq. (6.24) by the third one,

the scale factor is eliminated and the collinearity equation follows:

$$\begin{aligned} x' &= x'_0 + \Delta x' - z' \frac{r_{11}(X - X_0) + r_{21}(Y - Y_0) + r_{31}(Z - Z_0)}{r_{13}(X - X_0) + r_{23}(Y - Y_0) + r_{33}(Z - Z_0)} \\ y' &= y'_0 + \Delta y' - z' \frac{r_{12}(X - X_0) + r_{22}(Y - Y_0) + r_{32}(Z - Z_0)}{r_{13}(X - X_0) + r_{23}(Y - Y_0) + r_{33}(Z - Z_0)} \end{aligned} \quad (6.25)$$

One can see, that Eq. (6.25) describes the transformation of the object coordinates into the corresponding image coordinates as functions of interior orientation parameters and exterior orientation parameters of the image.

A method to calculate the exterior orientation of a single image is called *space resection*. The method is based on collinearity equations, i.e. Eq. (6.25), and it provides a non-linear solution. Due to the group τ of six dependent variables $\tau = \tau(X_0, Y_0, Z_0, \alpha, \beta, \gamma)$ at least three independent reference points in the object space (3D) are required to find a solution. Every point contributes with a set of two nonlinear equations:

$$H(\tau) = \begin{bmatrix} (x'_j + \Delta x'_j - x'_0)(\hat{X}_j - \hat{X}_0) \cdot (\hat{r}_{:,3}) + f(\hat{X}_j - \hat{X}_0) \cdot (\hat{r}_{:,1}) = 0 \\ (y'_j + \Delta y'_j - y'_0)(\hat{X}_j - \hat{X}_0) \cdot (\hat{r}_{:,3}) + f(\hat{X}_j - \hat{X}_0) \cdot (\hat{r}_{:,2}) = 0 \end{bmatrix}, \quad (6.26)$$

where \hat{X}_j stands for the j -th object point given in (X_j, Y_j, Z_j) coordinates. Eq. (6.26) can be linearized using the Taylor series expansion:

$$H^{k+1}(\tau) = H^k(\tau) + \left(\frac{\partial H}{\partial \tau} \right)^k \Delta \tau \quad (6.27)$$

and solved by least-squares adjustment, e.g. based on the Newton method [83]. The least-squares adjustment

$$\begin{aligned} H^{k+1}(\tau) &= 0 \\ \Delta \tau^k &= \tau^{k+1} - \tau^k \\ \tau^{k+1} &= \tau^k - \left(\frac{\partial H}{\partial \tau} \right)^{-1} H^k(\tau) \\ |H(\tau^{k+1}) - H(\tau^k)| &< \epsilon \end{aligned} \quad (6.28)$$

runs in an iterative way. In each step a system of linear equations is computed for estimated values of τ . The iterative procedure is terminated when it converges, i.e. when the convergence parameter ϵ is less than the set convergence criterion.

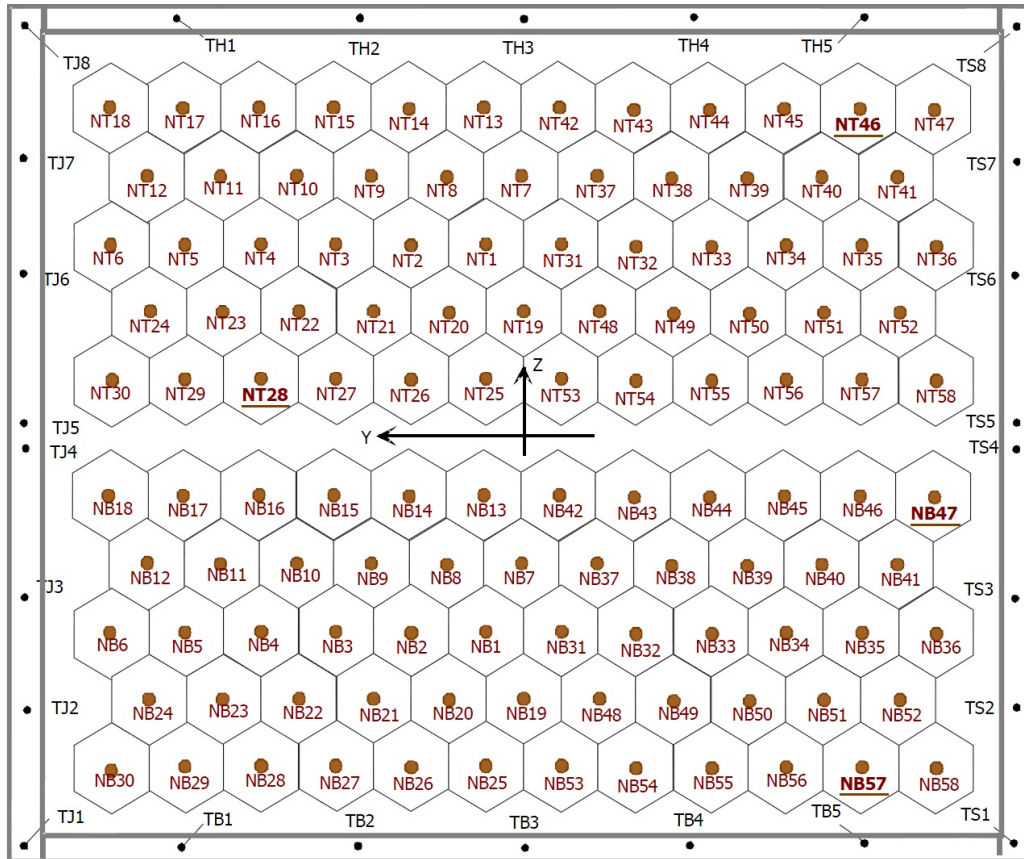


Figure 6.9: RICH1 mirror's labels. Reference points are fixed to the mirror-wall. Their labels start with T [86].

MATLAB is commercially available computing software [84]. Among MATLAB many defined functions, several non-linear least-square methods are already implemented, namely the Gauss-Newton algorithm. Compared e.g. to commonly used Newton-Raphson's method, second derivatives are not required. The Gauss-Newton algorithm minimizes a sum of squared function values. Detailed description can be found also in MATLAB product help.

Correct solution of the least-squares adjustment can be found only when a good initial guess of the τ is provided into the procedure. Approximate values for the first step of the algorithm were obtained by the direct measurement of the RICH1 detector from the CAD drawings [85] and by the simulation of the CLAM system in MATLAB environment.

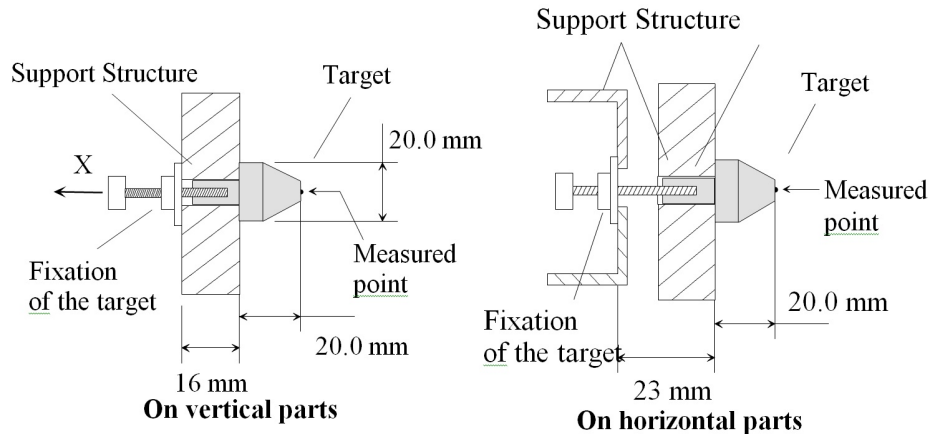


Figure 6.10: Photogrammetric targets on the mirror wall. These targets were used for theodolite measurements which is described in Sec. 3.1.

6.1.2.1 Photogrammetric targets on the frame of the mirror wall

To compute the camera position in the COMPASS coordinate system, reference points in the object space are required. 26 reference points were installed on the mirror wall frame (Figure 6.9). As a consequence of the plane frame, the reference points are coplanar. Because of various obstacles inside the vessel, such as e.g. the beam pipe or various wires, each camera can use maximum of six reference points.

The positions of the reference points were measured by the surveyors using standard photogrammetric targets (Figure 6.10). Then, for the purpose of CLAM measurements, the targets were modified by the retroreflective circular sticker placed on the top of each target (Figure 6.11). Visual inspection inside the RICH1 vessel shows the central misalignment of stickers in the order of 0.5 mm. Positions of the targets are summarized in Table 6.4. The precision of the coordinates in that table is 0.5 mm along XYZ axes.

Two LEDs are used to illuminate the scene (Chapter. 4). The LEDs are placed symmetrically on the sides of each CLAM camera. The direction of the illumination changes in the case, that only one LED is illuminating the targets. As a result the position of the target in the image will be changed. The effect is discussed in the following text.

The targets consist of small reflective balls made from high refractive index glass. Each glass ball can partially reflect light backwards to the light source. Figure 6.12 represents a scheme of beams which are reflected by the photogrammetric target. The beam, falling to the sphere surface at an angle

name	X (m)	Y (m)	Z (m)
TB1	8.4535	1.9512	-2.3013
TB2	8.4541	0.9765	-2.3004
TB3	8.4545	0.0019	-2.2996
TB4	8.4546	-0.9729	-2.2995
TB5	8.4548	-1.9480	-2.3012
TH1	8.4539	1.9533	2.2954
TH2	8.4544	0.9782	2.2942
TH3	8.4547	0.0034	2.2944
TH4	8.4548	-0.9709	2.2941
TH5	8.4552	-1.9463	2.2943
TJ1	8.4538	2.9018	-2.3033
TJ2	8.4535	2.9011	-1.5481
TJ3	8.4535	2.9012	-0.7933
TJ4	8.4534	2.9037	-0.0382
TJ5	8.4536	2.9037	0.0318
TJ6	8.4534	2.9036	0.7867
TJ7	8.4533	2.9033	1.5414
TJ8	8.4532	2.9030	2.2964
TS1	8.4541	-2.8969	-2.3024
TS2	8.4542	-2.8967	-1.5473
TS3	8.4544	-2.8964	-0.7925
TS4	8.4545	-2.8962	-0.0376
TS5	8.4545	-2.8961	0.0325
TS6	8.4547	-2.8951	0.7875
TS7	8.4548	-2.8954	1.5423
TS8	8.4552	-2.8968	2.2977

Table 6.4: The coordinates of the CLAM reference targets placed on the frame of the mirror wall [51].

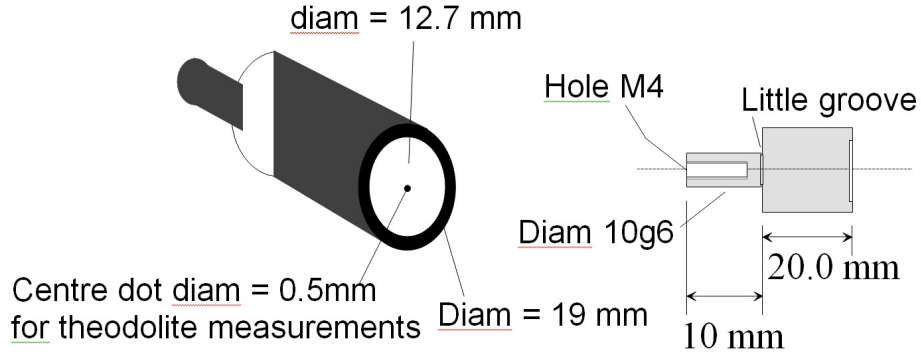


Figure 6.11: CLAM targets on the mirror wall. These targets are used for CLAM measurements. In the centre of each retroreflective target, a dot is present. The dot allows to measure the position of the target by theodolite.

α , is refracted at an angle β , obeyed the Snell's law. It is deflected about $\alpha - \beta$ at point A. The part of the beam is reflected on the opposite side at point B and forwarded out from the sphere with the change of direction of an angle $\pi - 2\beta$. The beam is refracted again at the output point C from the ball by an angle $\alpha - \beta$. The emerging beam direction forms an angle $\pi + \gamma$ with the direction of original beam. If we define an angle γ with an orientation to be positive for diverging input and emerging beams (for small refractive index), and negative for crossing beams (high refractive index) as it is shown in Figure 6.12, the final deflection angle can be described by the equation:

$$\gamma = 4\beta - 2\alpha \quad (6.29)$$

We can assume a simple model, that the ball is far from the diode (the ball radius R is many times smaller than the distance of the ball from the diode), and the ball is illuminated by almost parallel beam. The principal ray, passing towards the principal point of a camera in the direction γ , seems to go from the point C. The point C lies in the distance r from the optical axis which connects the center of the ball and the principal point of the camera. Simply $\sin \alpha = r/R$. If Snell's law is taken into account, γ can be expressed in terms of the refractive index n :

$$\gamma = 4 \arcsin\left(\frac{r}{nR}\right) - 2 \arcsin\left(\frac{r}{R}\right). \quad (6.30)$$

Figure 6.13 explains both rainbow (water drop, $n = 1.33$, the most of light is deflected about 0.75 rad) and exceptional properties of balls with

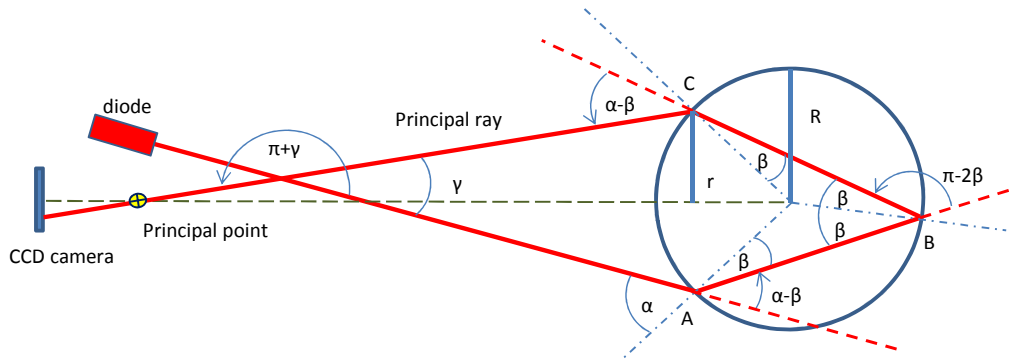


Figure 6.12: Photogrammetric target - schematic drawing of beams in glass ball with refractive index $n = 2.0$. The beam, falling to the sphere surface at an angle α , is refracted at an angle β , obeyed the Snell's law. It is deflected about $\alpha - \beta$ at point A. The part of the beam is reflected on the opposite side at point B and forwarded out from the sphere with the change of direction of an angle $\pi - 2\beta$. The beam is refracted again at the output point C from the ball by an angle $\alpha - \beta$. The emerging beam direction forms an angle $\pi + \gamma$ with the direction of original beam.

the refractive index equal to 2.0. Almost all beams, falling to the ball close to axis, are reflected back to the light source (deflection is below 1 mrad for $r/R < 0.16$, and 10 mrad for $r/R < 0.34$) as it can be seen from the figure.

A more sophisticated model was tested, but the result doesn't differ from the simple one mentioned so far more than in one percent. It is not necessary to take into account also the external reflection on the first surface and effect of two inner reflections, due that the reflection towards the camera is almost negligible in both cases.

For photogrammetric targets an inverse problem must be solved. The angle γ is fixed by geometry measurement: ratio of distance of diode and camera principal point to the distance of ball. The observed image of a beam spot is not in the center of the ball. It is due only beams that are not reflected backwards to the diode. The observed relative position r/R of the spot inside the ball image is described by previous equation Eq. (6.30). Spot is not symmetrical due the asymmetry of spherical error of ball surface. The incoming beams to camera seem to be almost parallel, thus the camera must be focused almost to infinity.

For the two LEDs, symmetrically placed on the both sides of the CLAM camera, two spots on the ball surface are observable. Spots are symmetrically situated at the ball image. The left spot corresponds to the left source,

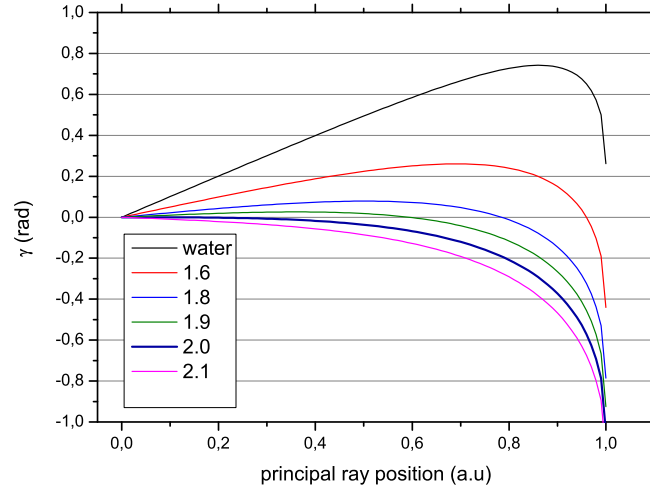


Figure 6.13: Photogrammetric target - deflection of the beam vs. relative principal ray position, given by r/R ratio.

and vice versa. The center of gravity of the two spots image corresponds to the center of the ball image. The distance of the spots is function of angle γ only, so the variation of this distance due to the ball movement is negligible.

6.1.2.2 Image processing

Photogrammetric targets are equally distributed on the mirror wall frame of the supporting structure. They are coplanar and when one looks at the CLAM pictures it can be seen that they are placed at the edges of images. Consequently, the correction parameters (Sec. 6.1.1) are non-negligible according to the position of the reflection points on the mirror wall. It also means that the illumination of the targets differs significantly (Figure 6.14). Furthermore, during the images taking, it happened that only one of the two diodes was working. In such cases, the illumination changed completely. As a result, some of the mirror-wall photogrammetric targets were not illuminated and therefore, the number of inputs to the space resection algorithm decreased. The following image processing techniques were chosen and as well their adaptation was adjusted to suppress such variations in the input

to the camera position algorithm.

When looking for the positions of the mirror wall photogrammetric targets in an image, k-means clustering method [87] is the core of the algorithm. Typically, the method is used in machine learning and data mining, where a g set of observations is given and k-means clustering aims to partition them into h clusters. The observation is assigned to the cluster with the nearest mean. It is an iterative process, where in the initial step h randomly selected observations are assigned to h clusters [88]. In every following step each observation is assigned to the cluster whose mean yields the least within-cluster sum of squares, alias the squared Euclidean distance and new mean is calculated to be the centroid of the observations in the new clusters. The algorithm converges when the assignments no longer change. The assignment can be expressed by:

$$\arg \min_{\text{clusters}} \sum_{i=1}^g \sum_{\text{obs}_j \in \text{cluster}_i} \|\text{obs}_j - \boldsymbol{\mu}_i\|^2, \quad (6.31)$$

where $\boldsymbol{\mu}_i$ is the mean of observations in cluster i .

Image preprocessing techniques used in the program eliminate most of spurious objects in the image. Photogrammetric targets are the most illuminated parts of the image, hence it is possible to threshold the image. Of course, the light intensity varies across the illuminated area. The threshold value is estimated automatically using the Otsu's method [89]. According to the estimated value the threshold is overwritten. There are two values of thresholds to be used. They correspond to the intensity values of the investigated targets. The values were chosen experimentally. As a result of the thresholding, a binary image is obtained and connected components can be found. In some cases the area of the components is too large (expected diameter of the target is 3 – 9 pixels). It happens when the light intensity is too high, or there are significant reflections in the image (Figure 6.14). Consequently, the procedure has to be repeated with increased threshold. During the preprocessing too small components are also deleted. Finally, only one or no component is left in the image. In case of purely illuminated targets, number of components is equal to zero and the threshold has to be decreased. In case that only one LED is switched on during taking photographs, some target may not even be visible in the picture. Very low threshold value can help, unfortunately many spurious objects arise as well. In such case the morphological opening (Sec. 5.3.1) can be applied with properly defined structuring element in the shape of disc.

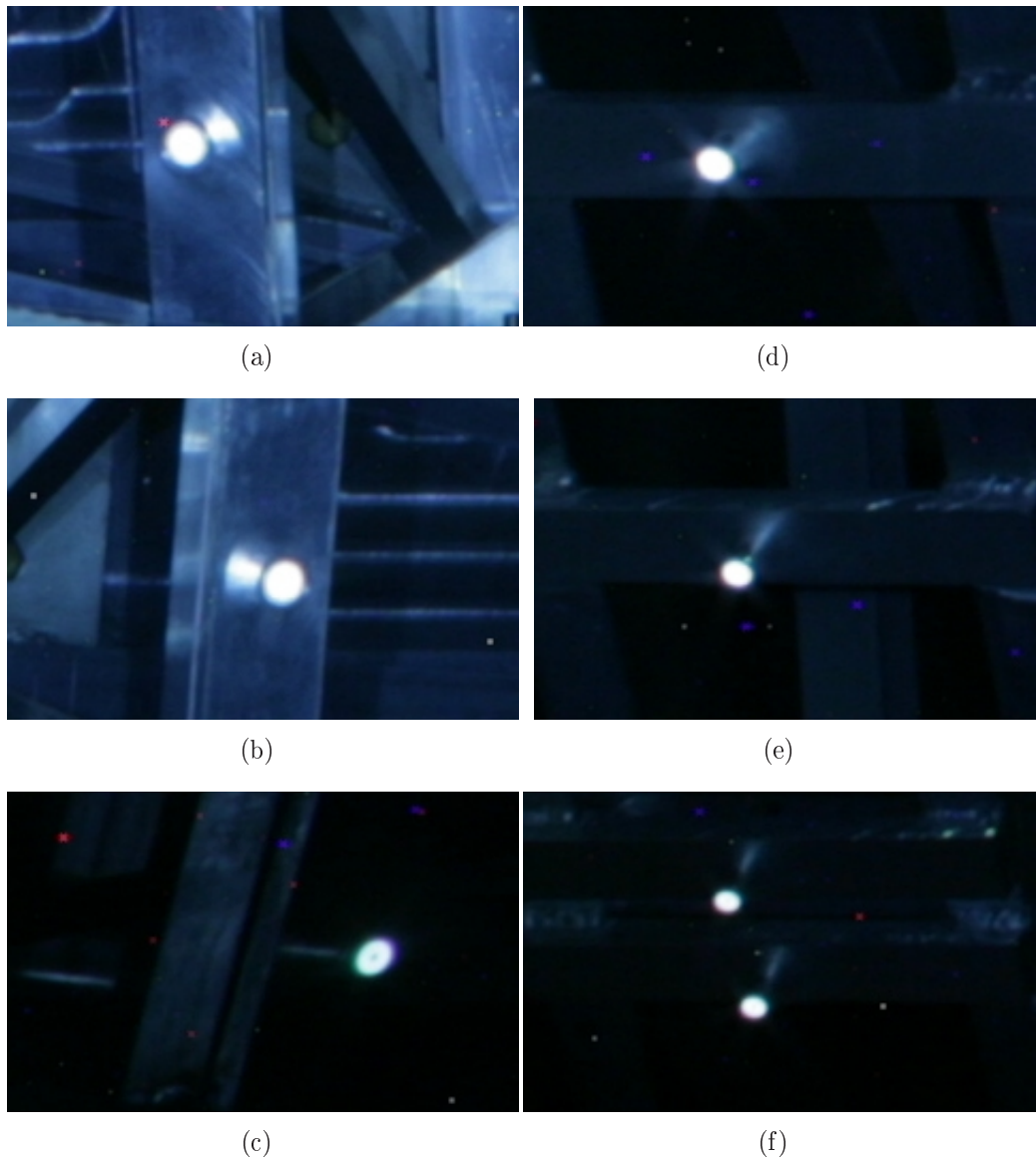


Figure 6.14: Example of the image of photogrammetric targets on the mirror wall in the JT part of the frame. Both LEDs were illuminating the scene for 5 seconds. Figures (a,b,c) correspond to horizontal targets TH1, TH2, TH3 respectively and (d,e,f) correspond to vertical targets TJ7, TJ6, TJ5 and TJ4 respectively. In case that only one LED is illuminating the scene, target TH3 is not detectable.

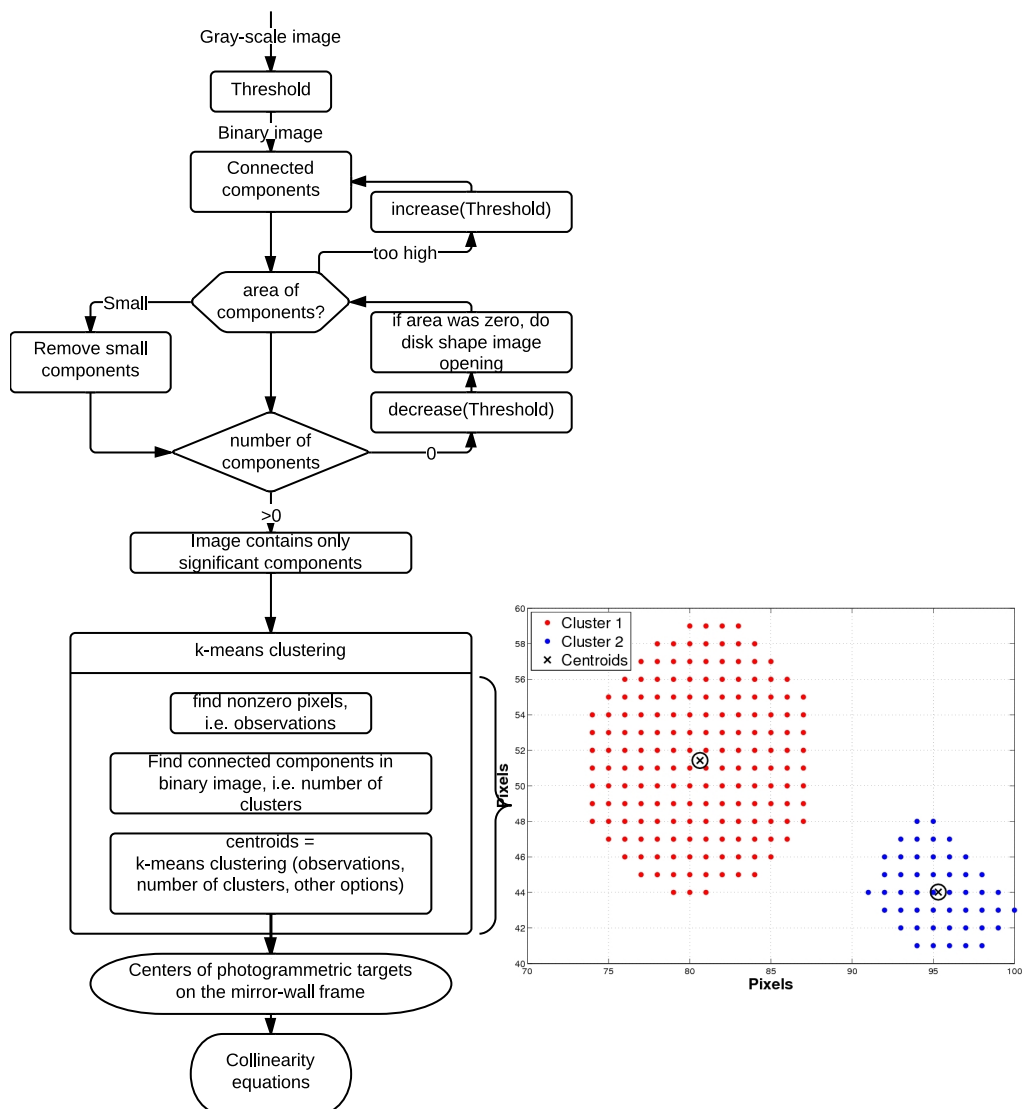


Figure 6.15: Overview of the image preprocessing in the camera position algorithm. Output of the algorithm is processed by collinearity equations.

The overview of summary of the algorithm of the image preprocessing is shown in Figure 6.15.

6.1.3 Sensitivity analysis of the camera position algorithm

The sensitivity analysis is the study how the uncertainty in the input to the mathematical model influences the final result, specifically the camera position. Several tests have been performed to ensure the stability of the algorithm.

First, the camera position was computed hundred times to verify algorithm repeatability. Input to the algorithm was kept identical. Two variants were tested: (i) The targets pixel coordinates were calculated once and (ii) The targets pixel were calculated anew at every repetition. The result was identical. The standard deviation of the repetitions was practically zero which means, that the the camera position algorithm gives equal results for invariable input.

In the previous Chapter, measured position of the photogrammetric targets placed on the mirror wall frame was discussed. To show the importance of accurate values of the position coordinates of the targets and the influence of the target coordinates on the camera position determination, the input coordinates (given in 3D) of selected targets were shifted ± 10 mm. The inaccuracy of the camera position determination for the photogrammetric target TH1 is shown in Figure 6.16. For every photogrammetric target a set of three subtests was performed, where for each test only one coordinate varies. The effect is calculated for each coordinate of the camera position.

To evaluate the positions of all CLAM cameras, the maximum of seven photogrammetric targets for each camera can be used. Furthermore, all the targets are coplanar and placed at two borders of the image. The task of the following test is to identify the minimum number of photogrammetric targets as inputs. Figure 6.17 shows that the position of the selected camera is set correctly with minimum of four targets. The procedure was performed as follows: There are seven targets in total. Every run of the algorithm, the input data of one target are removed from the algorithm and the position of the camera is calculated. The procedure continues until only one target is left in the input data. Analogously, the influence of only one missing target out of seven was tested (Figure 6.18). Every run of the algorithm, only one target (out of seven) is removed. The more distant target from the camera, the largest is the effect on the accuracy of the camera position coordinates

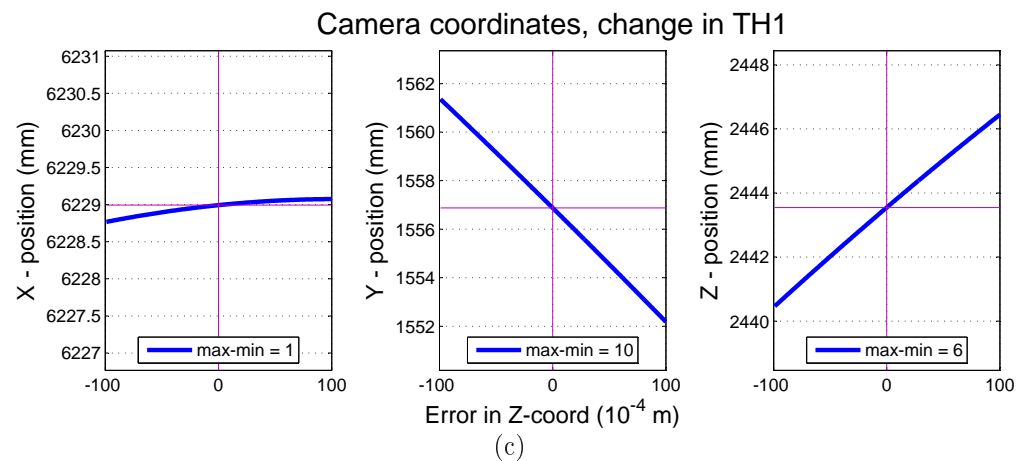
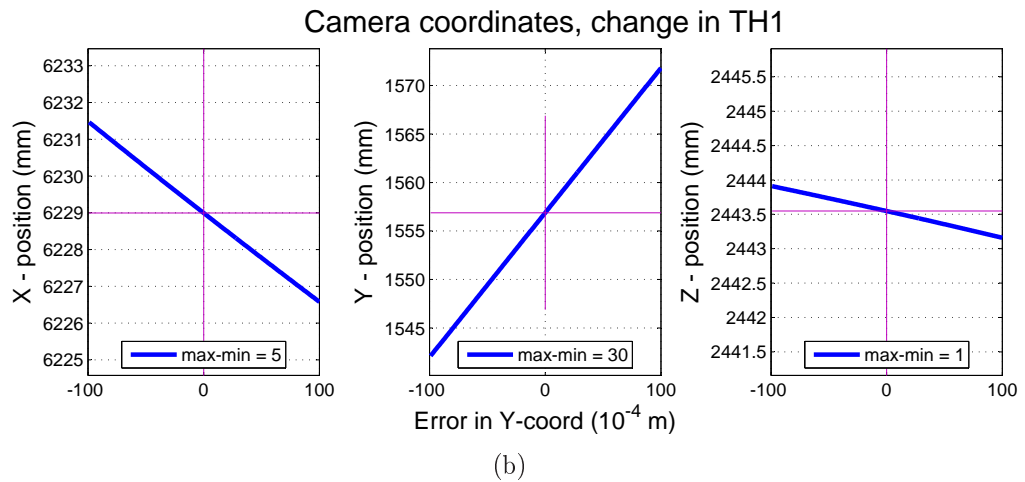
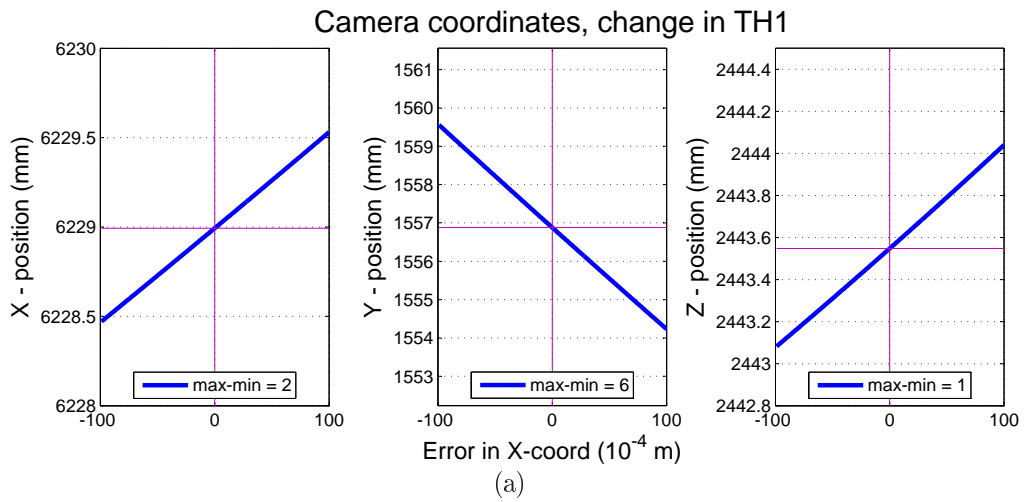


Figure 6.16: Camera position determination - inaccuracy in TH1 target coordinates was simulated. For every photogrammetric target a set of three subtests was performed, where for each test only one coordinate varies. It can be seen the influence for each coordinate of camera position.

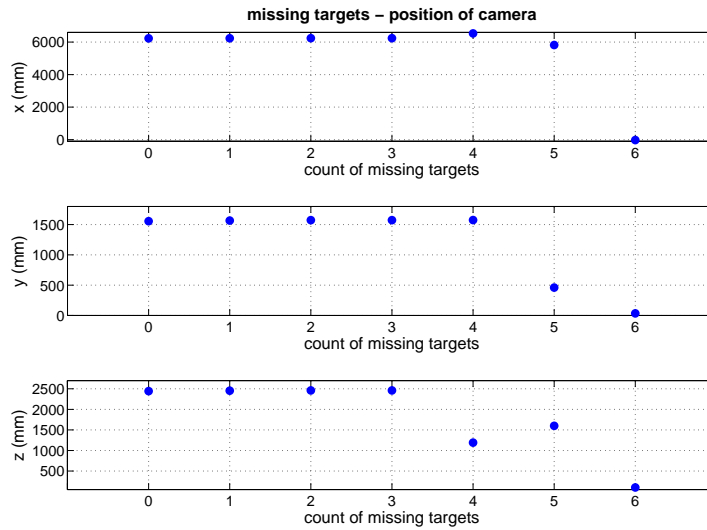


Figure 6.17: Camera position determination - depending on the number of input targets. There are seven targets for each CLAM camera in total. Every run of the algorithm, one of the targets is removed from the input data and the position of the camera is computed. The position of the camera is set correctly by minimum of four targets.

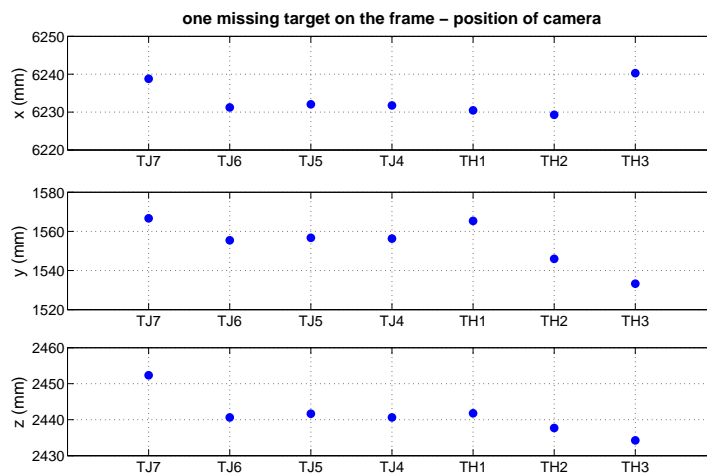


Figure 6.18: Camera position determination - depending on one missing target. Every run of the algorithm, only one target (out of seven) is removed. The more distant target from the camera, the largest is the effect on the accuracy of the camera position coordinates determination.

determination.

The last test shows an influence of the time of illumination of the mirror wall, together with the effect of the left or right diode switched off. The results are summarized in plots in Figure 6.19. The time of illumination ranges from 0.5 to 5 seconds. The measurement was repeated again with changed shutter setting of the camera from 3.2 to 6 seconds. The main source of error is caused by the switched off diode placed on the right side of the camera. In such conditions, target TH3 is not illuminated. The effect is apparent especially for low illumination times (standard deviation is about 8 mm). The algorithm works reasonably well when both LEDs are switched on, or even left LED only (standard deviation is about 0.3 mm). According to the camera position computations, the optimal LED illumination time is about 3 – 4 seconds, the exposition time is not the crucial parameter.

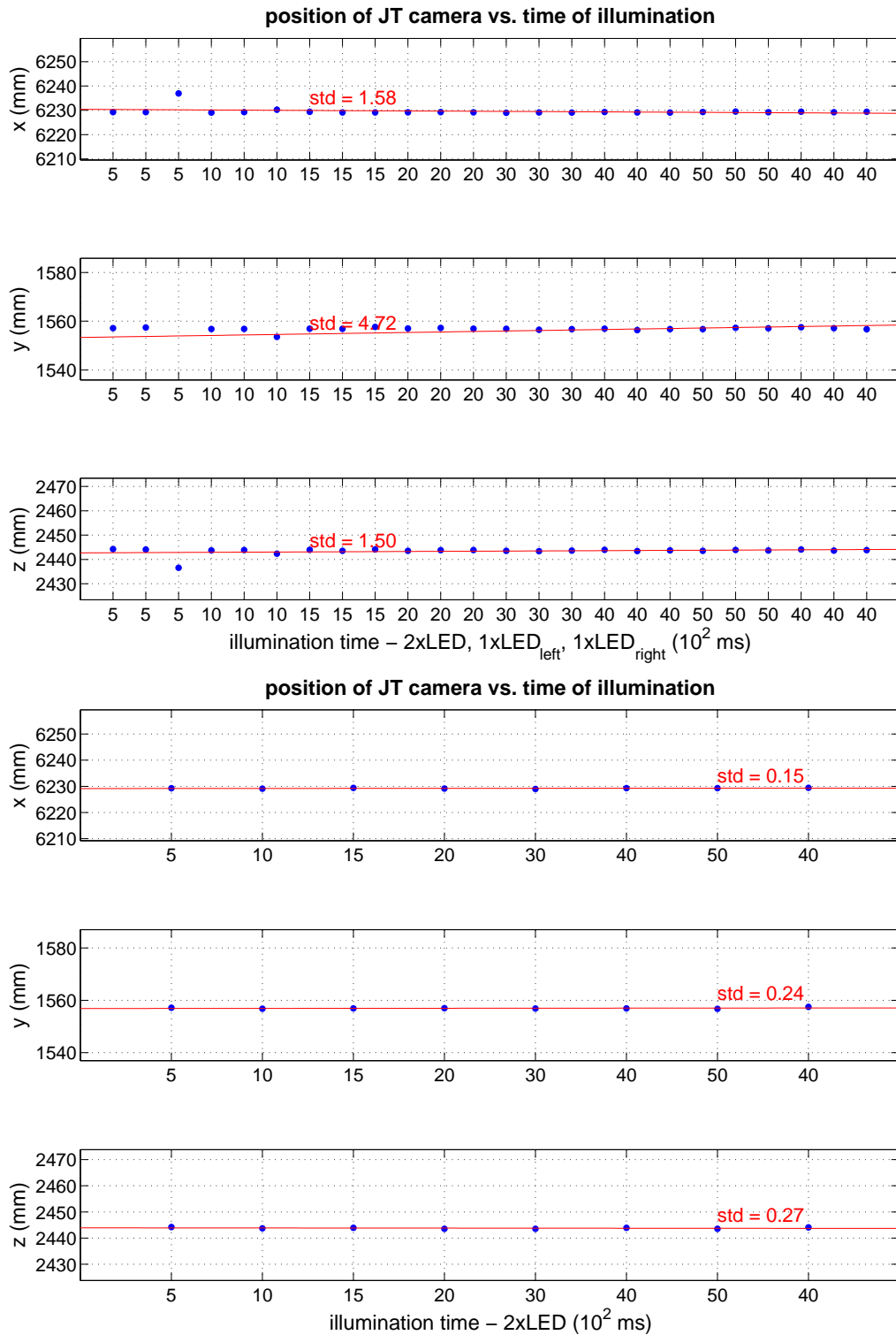


Figure 6.19: Camera position determination - depending on the illumination time. The main source of error is caused by the switched off diode placed on the right side of the camera. The effect is apparent especially for low illumination times (standard deviation is about 8 mm). According to the camera position computations, the optimal LED illumination time is about 3 – 4 seconds, the exposition time is not the crucial parameter.

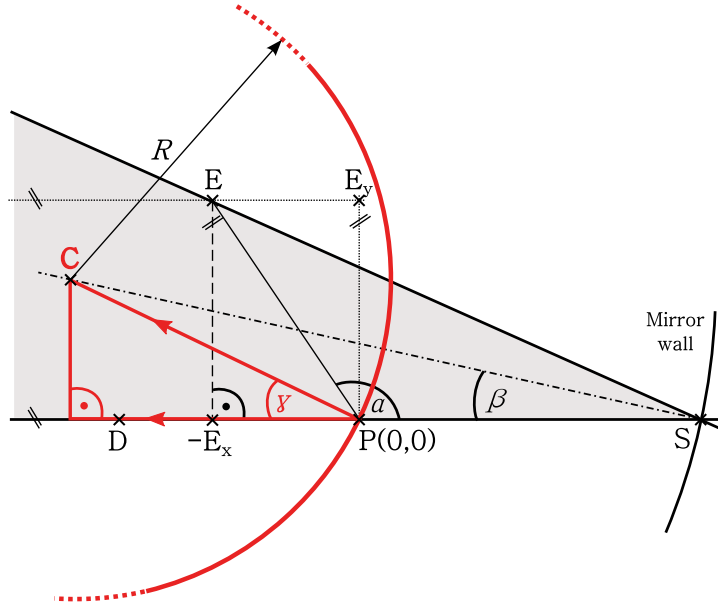


Figure 6.21: Determination of mirror orientation - principle geometry in 2D coordinate system defined using the positions of the points P, E, D . P is the principal point of CLAM camera. It defines the origin of the system. E is the point of the retroreflective rectangular grid with the axes projections E_x and E_y into the 2D plane. The point D is the image of the point E on the camera sensor, S stands for the reflection point on the mirror surface and C for the center of curvature of the mirror.

camera sensor. The positions of points P and D were calculated in previous Section (Sec. 6.1). The position of E was measured with the precision of 0.5 mm in every coordinate. The reflection point S on the mirror surface is not known while only the *ideal* center of curvature C_{id} is known. Also, the ideal the radius of curvature R_{id} of the spherical mirror is known. We search for the centers of curvature C of individual mirrors.

Since points P, E, D are theoretically coplanar, it is possible to define 2D rectangular coordinate system (Fig. 6.21), where the origin is set in the point P , i.e. $P = (0, 0)$, and the x -axis is defined by the direction of the vector \vec{DP} . E_x and E_y are 2D coordinates of the point E . According to the given geometric system, $S = (u, 0)$, where $u = |\vec{PS}|$. Then, C can be expressed as:

$$C = \vec{PS} + \vec{SC} = (u, 0) + (-R \cos \beta, R \sin \beta), \quad (6.32)$$

where β stands for the reflection angle of the mirror surface. There are two unknown variables, u and β . Using the law of sines, the position of the point C in 2D can be estimated using the equation:

$$C_{2D} = \left(\frac{|PE| \sin(\alpha) \cos(2\beta)}{\sin(2\beta)} + |PE| \cos(\alpha) - R \cos(\beta), \quad R \sin(\beta) \right) \quad (6.33)$$

For a set of input points P, E , center of curvature C_{2D} is obtained as a function of parameter β . Back-projection of the C to 3D coordinate system can be resolved using following considerations:

$$(C - D) \cdot [(P - D) \times (E - P)] = 0 \quad (6.34a)$$

$$|\vec{SC}| - R = 0 \quad (6.34b)$$

$$\|C - P\| - \|C_{2D}\| = (C - P) \cdot (C - P) - \|C_{2D}\|^2 = 0 \quad (6.34c)$$

$$\frac{(C - P) \cdot (P - D)}{\|C_{2D}\| \|P - D\|} - \frac{C_{2D,x}}{\|C_{2D}\|} = 0 \quad (6.34d)$$

The meaning of Eqs. (6.34a) - (6.34d) is the following: Eq. (6.34a): Points D, P, E, C are coplanar, Eq. (6.34b): The distance between points S and C is equal to the radius of curvature of the mirror, Eq. (6.34c): The distance between the points P and C . In other words, it is the equation of a circle with the center in P , Eq. (6.34d): The angle γ are equal in 2D and 3D systems (Fig. 6.21).

The theoretical position of the center of curvature of every mirror is given in spherical coordinates R, φ, θ relative to the ideal center of curvature of the top/bottom sphere [90]. The coordinate system is defined according to Figure 6.22: The origin is at the sphere centre, the vertical z -axis is in the upwards direction, the x -axis lies on the vertical symmetry plane of the spheres and y -axis is perpendicular to the zx plane. xyz axes share directions with the COMPASS survey coordinate system. For spherical coordinates, the angle θ is measured from z -axis towards the polar vector while the angle φ is measured from x -axis towards the projection of the polar vector into the xy plane.

The absolute misalignments of the mirrors are given as differences of the spherical coordinates $\Delta\varphi, \Delta\theta$. The misalignment is computed from the ideal center of curvature of the sphere C_{id} , the calculated center of curvature C of selected mirror and the center of the mirror M_S . Spherical coordinates of the mirror center are recalculated according to the calculated center of curvature C . Finally, the misalignments are calculated by subtraction of

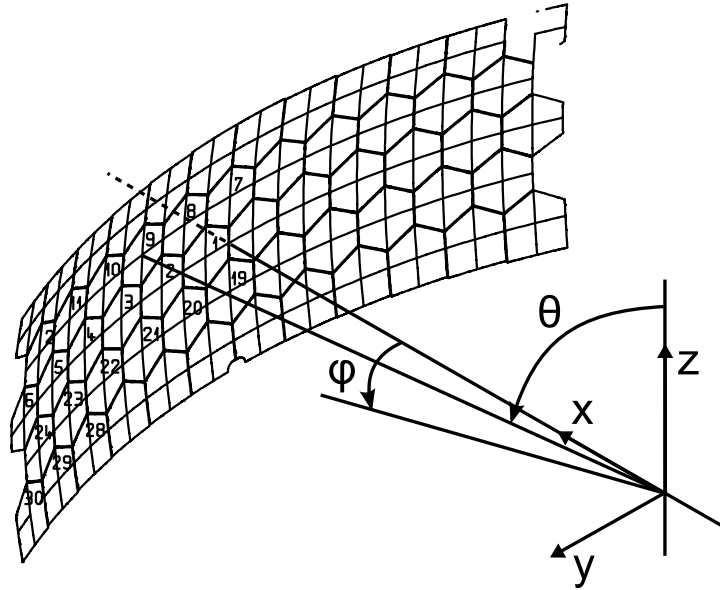


Figure 6.22: Determination of mirror orientation - The spherical coordinate system in the RICH1.

the original spherical coordinates of the mirror center of the recalculated ones.

A description of the computational program of the absolute measurement algorithm is presented in the following Section.

6.2.1 Image processing

The inputs to the algorithm of finding the mirrors misalignment are the position of CLAM camera P , 3D coordinates of the retroreflective rectangular grid point E , the ideal center of curvature of the sphere C_{id} , ideal position of the center of the mirror M_S and a picture taken by the camera.

In the algorithm, mirrors are evaluated separately, i.e. the image is cropped to contain only a selected mirror. Every mirror reflects part of the grid towards the camera, hence the grid of conics emerges in the picture. As it was discussed earlier, only the intersections of conics are used in the calculations. At the intersections, photogrammetric targets are glued (Sec. 4.1.2). The first step of the algorithm is the determination of the targets positions in the image.

The targets are surrounded by dark border. From the perspective of image processing, the border is too narrow to be distinguished from the

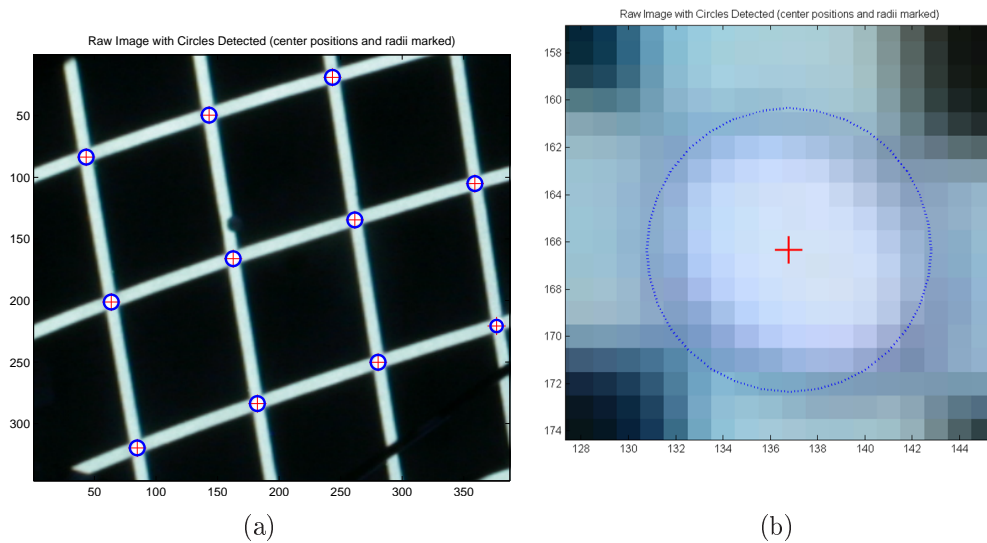


Figure 6.23: Detected reflections of photogrammetric targets in the image, (a) for one mirror, (b) in detail. The centers and edges of circles are found and marked.

illuminated background which is formed of the stripes. Practically, the the border of the target is visible only for low times of illumination. Also, the circular targets appear in the image as ellipses. The idea to separate the targets from the grid is to apply the morphological image opening (Sec. 5.3) with properly defined structuring element in the shape of line. The line structuring element is given by its length (in pixels) and by its angle (in degrees). At first, the inclination of lines of the grid has to be determined. The opening procedure is applied with angles from 5 to 180 degrees and the threshold value of the cropped image is computed. Maximum value of the threshold corresponds to the angle between the lines in the grid image. The procedure is applied twice for the two directions of lines forming the grid. The opening procedure is reapplied with known angles in such a way that the resulted images contain only horizontal or vertical lines. The intersections are found using the logical operator AND of the two black-white images. As a result, approximate positions of the targets are found and it is possible to treat them separately. In every target region the connected components are found and evaluated in a way that only pixels forming the targets retain. The procedure is similar to the one applied in Sec. 6.1.2. The area of the target consists of pixels of different intensity values. The center position of

the target is then given based on pixels locations and intensity values as it can be seen in Figure 6.23. Using Eq. (6.23) 3D coordinates of the centers D can be calculated.

The next task of the algorithm is to find the match between the points E and D . It was already explained, that all the points lie in the DPE plane. The reflection point S of a specific target on the mirror can be estimated from known coordinates of C_{id} and of the pair of points D, P . For every pair of points D, P a line is created. The intersection of the line and the circle with the center in C_{id} and the radius R gives us an estimation of the reflection point S . It is obvious that the angle of reflection β given by $\angle PSC_{id}$ and $\angle ESC_{id}$ should be similar. Both calculations are done and results are compared. Due to inaccuracies in estimated data a table of possible angle matches is created. For every record in the table, the distance between C_{id} and the plane given by the points PSC_{id} is calculated. The least distance corresponds to the match between E and D .

Finally, the set of equations (Eq. 6.34) can be formed and evaluated to obtain the center of curvature of investigated mirror. There are four unknown variables in the set of equations: The coordinates of C and the angle of reflection β . The non-linear equations are solved using Gauss-Newton method, the initial parameters are set as C_{id} and $\angle PSC$ for each pair of points E, D .

6.3 Results

To prove the concept of the absolute measurement algorithm, simulations and laboratory tests were performed. Results of the algorithm applied on real data is also discussed.

6.3.1 Simulations

The simulations were performed to estimate the accuracy of the mirror position determination. In the simulations, the reversed order of the algorithm is applied. In the preparation phase, only the principal point of the camera P and the object points in the image D are used as inputs. Mirror misalignment angles are set artificially and consequently, the center of curvature C and the targets on the grid E are calculated. Then, the position of all the points is known and the algorithm may run as it was described in Sec. 6.2, with D, P, E, C_{id} as the inputs, to search the previously calculated C .

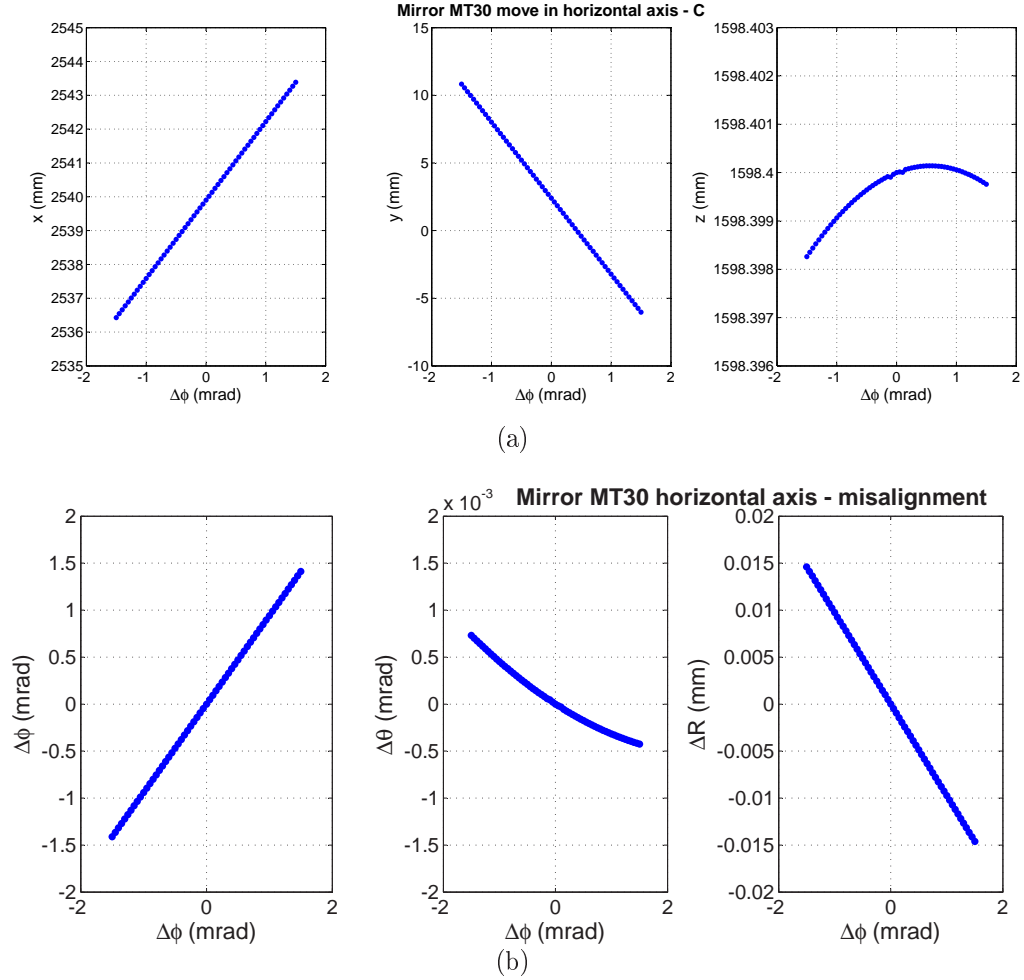


Figure 6.24: One of the example of results of the mirror misalignments simulations. The algorithm is launched for the mirror NT30 (it corresponds to the indication MT30 in the plots titles) in JT area of the mirror wall. x -axes correspond to the rotation of the mirror in a horizontal direction; (a) The calculated center of curvature C given in the COMPASS coordinate system; (b) The mirror misalignments in polar coordinates $\Delta\phi, \Delta\theta$ (b). ΔR corresponds to a difference of the ideal radius of curvature of the spherical mirror to the calculated one.

Figure 6.24 shows an example of a result of the simulation for mirror NT30 placed in the Jura-Top segment of the mirror wall (Fig. 6.9). In this particular test, the mirror is tilted horizontally of about ± 1.5 mrad from its nominal position. The resulting error of the algorithm is less than 2 %.

6.3.2 Sensitivity of the absolute method algorithm

In Sec. 5.2 the laboratory measurement, performed in order to calibrate the CLAM method, was described. In the measurement, a relationship between the shift of conics in the image in horizontal and vertical directions, *hor* and *ver* (in pixels), and the mirror misalignment angles, ϕ and θ (in mrad), was found for each mirror. Mirrors were tilted gradually with the least step of 0.05 mrad.

Since the laboratory arrangement simulates JT segment of the mirror-wall, the results of the measurement can be used to test the absolute algorithm sensitivity. It should be noted, that the position of the grid used in the measurement does not entirely correspond to the grid used in the RICH1 detector. Furthermore, the position of the camera is not known. Therefore, the test can be performed only with a few mirrors where predefined points *E* match points *D* which are detected in the image. Except this detail, the absolute algorithm is used as it would process the real data from the CLAM system in the RICH1 detector.

The Plots in Figure 6.25 show an example of the results for the mirror NT6. The mirror is tilted horizontally. Values on the *x*-axes correspond to the mirror misalignment in the horizontal direction measured by the laser interferometer (Sec. 5.2). Values on the *y*-axes correspond to the CLAM method results, i.e. the mirror misalignment, the coordinates of the mirror center of curvature and the position of the image of a target on the image sensor.

6.3.3 CLAM measurements in RICH1 detector

Now, the absolute algorithm is finally tested on real CLAM data, i.e. the pictures of the RICH1 vessel space which are taken by the CLAM cameras. The influences of the time of illumination and filling the RICH1 vessel with the C4F10 are discussed.

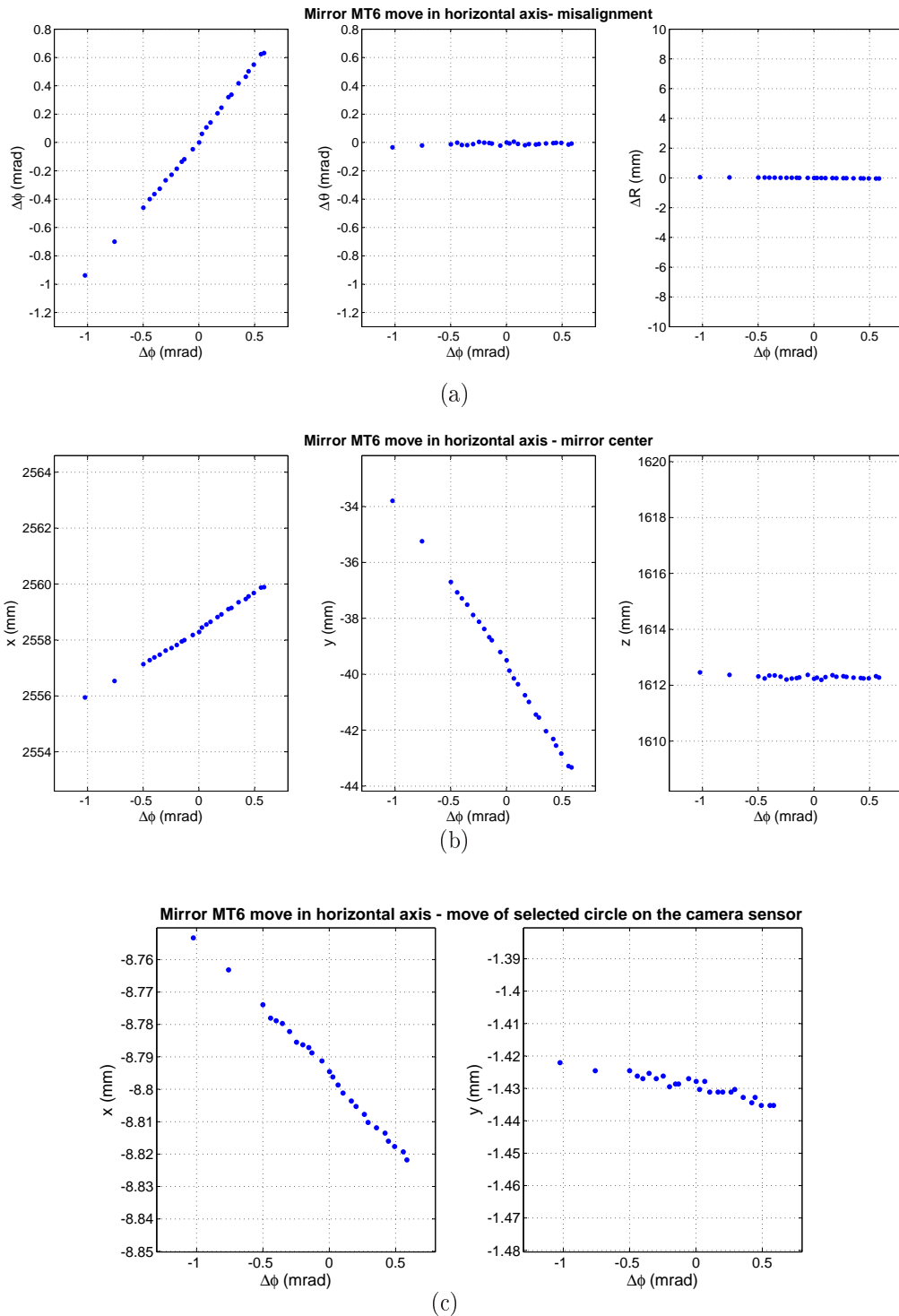


Figure 6.25: One of the example of results of the test of the sensitivity of the absolute method when the data measured in the laboratory were used as the input. The algorithm is launched for the mirror NT6 (it corresponds to the indication MT6 in the plots titles) placed in the JT area of the mirror wall. The mirror is tilted horizontally. Values on x -axes correspond to the mirror misalignment in horizontal plane measured by the laser interferometer (Sec. 5.2). Values on the y -axes correspond to the CLAM method results, i.e. the mirror misalignment, the coordinates of the mirror center of curvature and the position of the image of a target on the image sensor.

6.3.3.1 Time of illumination influence

The time of illumination of the mirror wall, together with the effect of left or right diode switched off, was tested. Distribution of the illumination intensity across the mirror wall is not homogeneous, it varies with the mirror relative position towards the source of illumination. The resulted effect is shown in Figure 6.26 for two cases, the most and the least illuminated mirror, NT1 and NT6.

It emerged that the mirror misalignment variations are mainly correlated with the camera position estimation (Sec. 6.1.3). Regardless of the considered number of LEDs used to illuminate the scene, the variations of the misalignment is less than 0.1 mrad. Considering only the case of both LEDs switched on, the variation is less than 0.05 mrad in wide range of illumination times (Fig. 6.27).

6.3.3.2 Filling RICH1 vessel with C_4F_{10}

During the non-operational mode of the COMPASS experiment, the vessel of the RICH1 detector is filled with the air. Typically, before the start of COMPASS run period, the vessel is filled with the nitrogen and subsequently with the radiator gas C_4F_{10} . CLAM pictures were taken during filling of the vessel: Before the filling (100 % of nitrogen), during the filling (12, 46, 60 % of C_4F_{10}) and at the end of the filling (100 % of C_4F_{10}).

According to the FEM model (Sec. 6.1.1.1), the density and by extension the refractive index of the gas is changing during the filling of the vessel. This effect was also proved using the absolute measurement algorithm as it can be seen in Figure 6.28, where only refractive index of the air is taken into account in the computations. The maximum change of the mirror misalignment at the level of 46 % of C_4F_{10} inside the vessel is correlated with the change of the calculated position of the camera. From the FEM simulation results, it is known that the radiator gas fills the vessel gradually from bottom part of the vessel. Since the targets TJ4-TJ6 are inside the C_4F_{10} gas whereas the rest of the targets are still in the nitrogen atmosphere, the camera position is not calculated properly. The change of the refractive index can be included in the absolute algorithm using the correction given by Eq. 6.11.

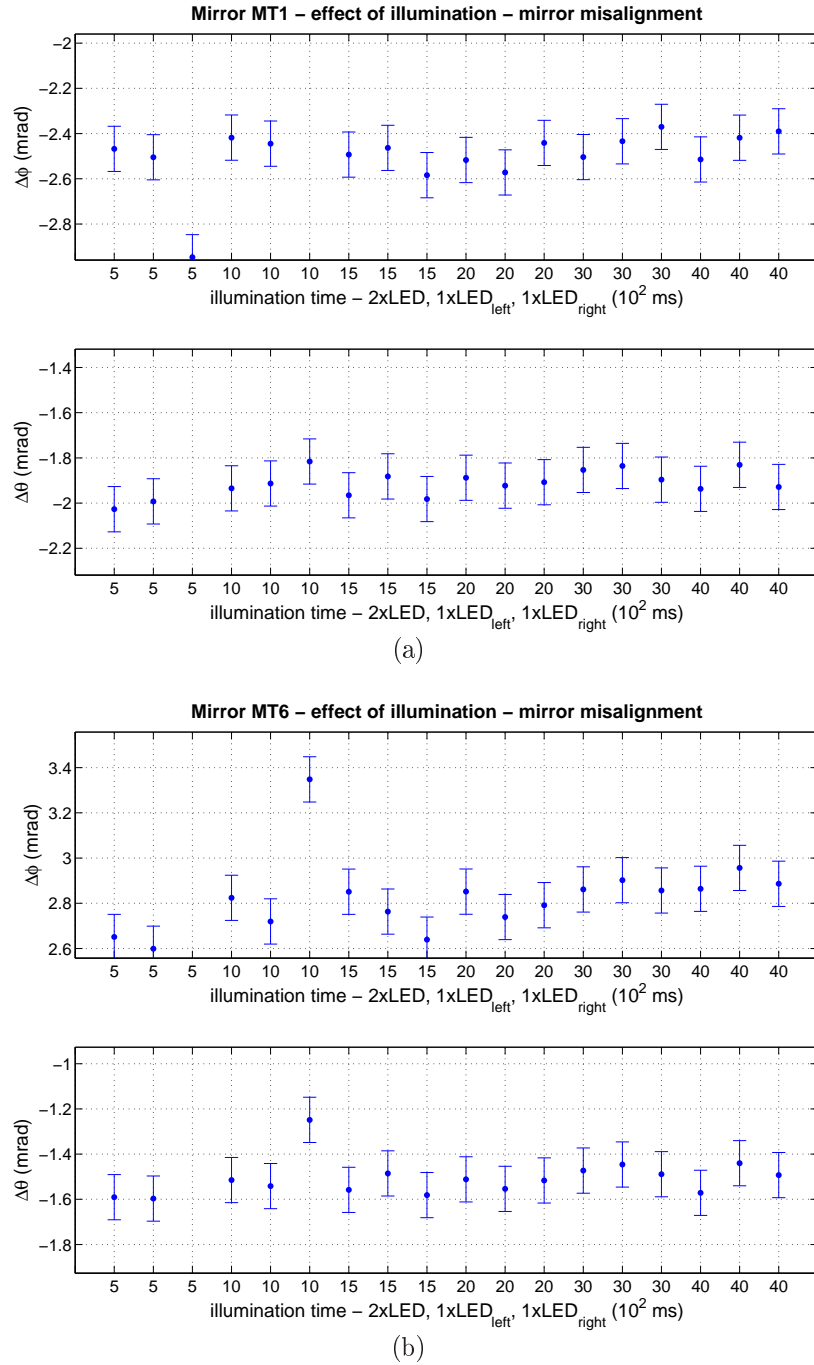


Figure 6.26: Influence of the time of illumination on the detected mirror misalignments ($\Delta\phi$, $\Delta\theta$). Different number of the LEDs switched on is considered for each set of illumination times. The results are presented for the mirror (a) NT1 and (b) NT6. The notations NT1 and NT6 correspond to the indications of MT1 and MT6 in the titles of the plots. Time of illumination ranges the interval of 0.5 ÷ 4.0 seconds. 102

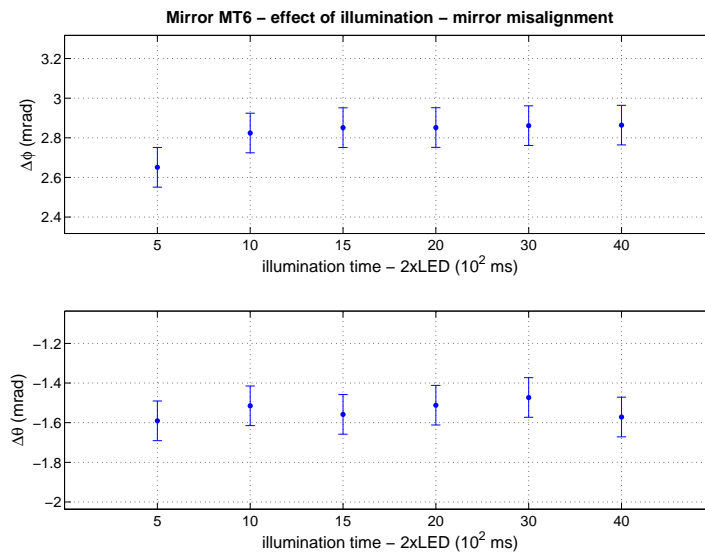


Figure 6.27: Influence of the time of illumination on the detected mirror misalignments ($\Delta\phi$, $\Delta\theta$). Only two LEDs switched on are considered for the set of illumination times. The results are presented for the mirror NT6 (corresponds to the indication of MT6 in the title of the plots). Time of illumination of two LEDs ranges the interval of 0.5 ÷ 4.0 seconds.

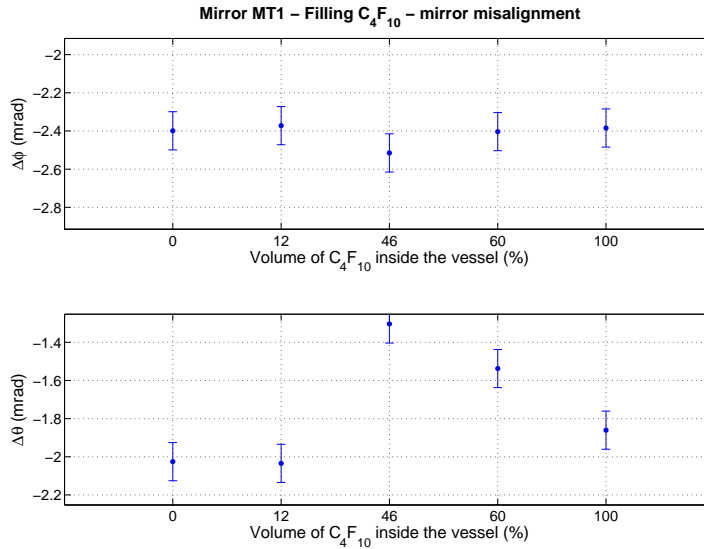


Figure 6.28: The effect of the filling the RICH1 vessel with C₄F₁₀. CLAM pictures were taken during filling of the vessel: Before the filling (100 % of nitrogen), during the filling (12, 46, 60 % of C₄F₁₀) and at the end of the filling (100 % of C₄F₁₀).

6.3.3.3 Measurements during COMPASS run

In Figure 6.29 the variations of mirror misalignments emerged during 2009 are shown. The measurements were randomly distributed over the COMPASS run period, i.e. between May and September 2009. Variations in tilt determination for the mirror NT1 are in the range of ± 0.2 mrad.

In 2001, the whole mirror wall was aligned and the measured residual misalignments showed a standard deviation of 0.06 mrad. The measurements of the misalignments were performed with the theodolite in autocollimation mode method (Sec. 3.1). In following years, the mirrors alignments were measured several times between the experiment data taking periods (from 2002 to 2012 [86,91–94]). Because of a certain difficulty of the theodolite measurement method, the time and space demands, only a few selected mirrors were investigated. The theodolite must be oriented to the center of mirror very precisely. Looking at several theodolite measurements in the RICH1 detector, an error in the theodolite position or an inclination of 1 cm corresponds up to 1.6 mrad error in the mirror misalignment estimation. During the theodolite measurements, the misalignments with a random distribution in the range of 0 – 1 mrad have been observed, with a

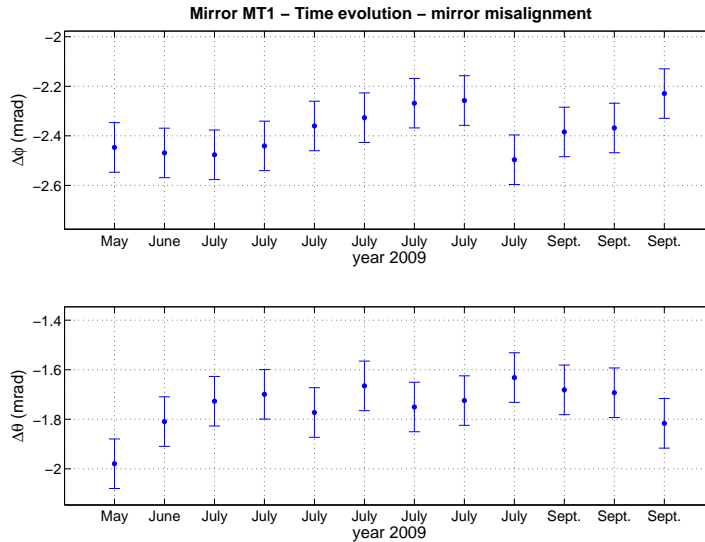
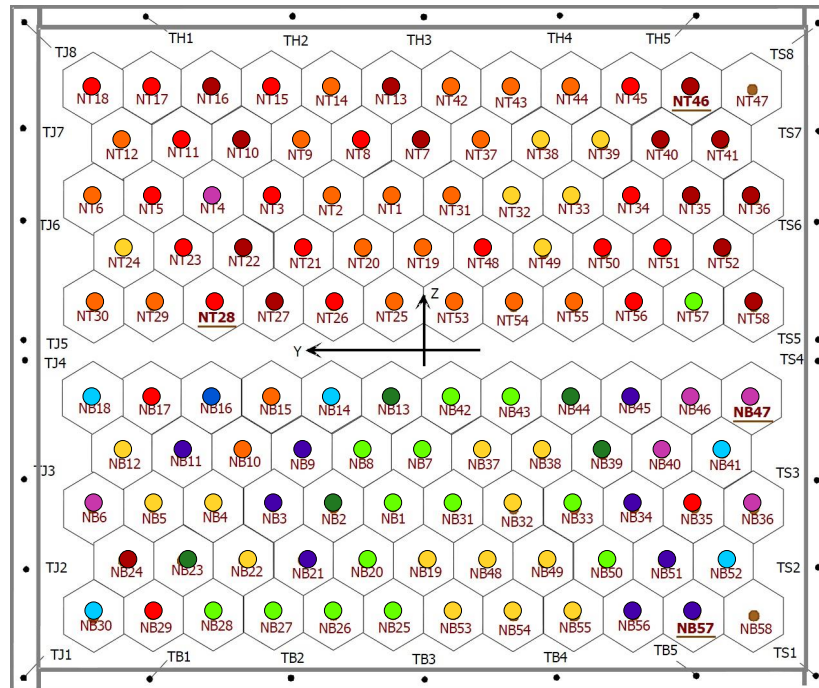


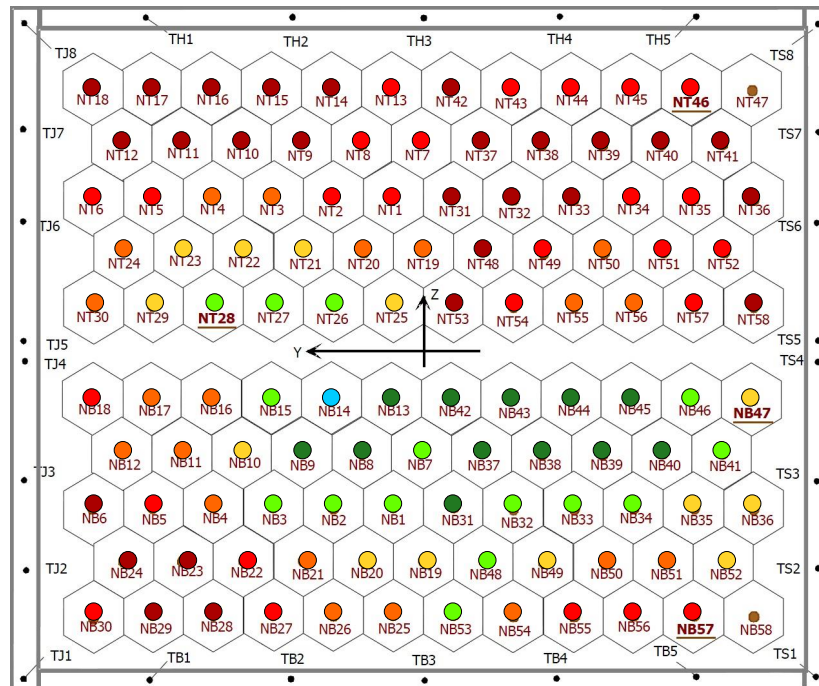
Figure 6.29: Detected mirror misalignments during COMPASS run period. CLAM pictures were taken during 2009. Measurements are randomly distributed over the COMPASS run period between May and September.

few elements exhibiting the misalignments of about 1.5 mrad. The cause of the misalignments emerged after the initial alignment is not known. When one compares the theodolite method with the applied CLAM method, the values differ significantly.

The detected misalignments of all the mirrors are shown in Figure 6.30. Only two mirrors are not measurable by the CLAM method in RICH1 detector, NB58 and NT48, because in the camera field of view the both mirrors are hidden behind an obstacle. The histograms in Figure 6.31 summarize the misalignments of the mirrors for the angles in horizontal and vertical direction, ϕ and θ . The resulting values indicate that almost 50 % of mirrors are horizontally misaligned up to 3 mrad at maximum and 65 % of mirrors are vertically misaligned of about 3 mrad at maximum.

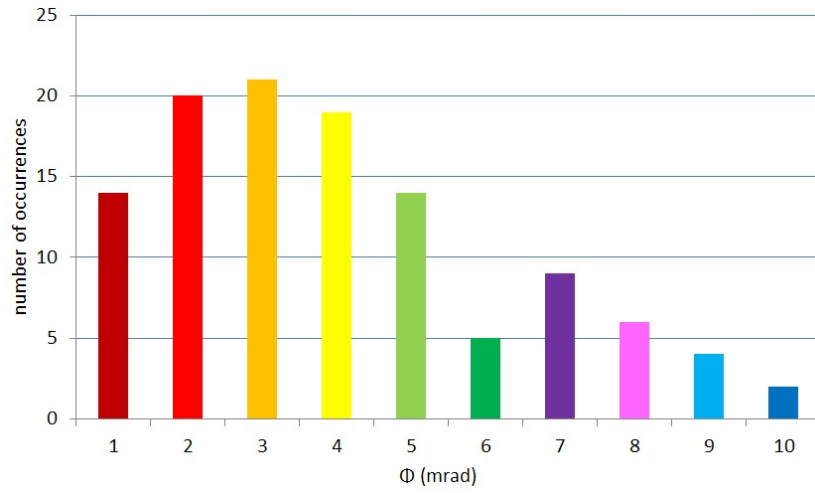


(a)

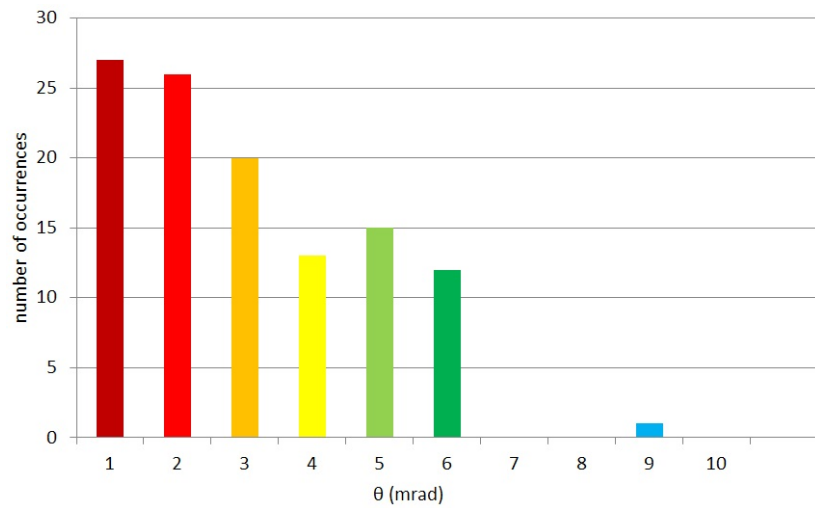


(b)

Figure 6.30: A complete list of detected mirrors misalignments (a) in the horizontal direction and (b) in the vertical direction. The colors correspond to the histograms values in Figure 6.31



(a)



(b)

Figure 6.31: Histograms which summarize the detected misalignments of the mirrors. The resulting values indicate that almost 50 % of mirrors are horizontally misaligned up to 3 mrad at maximum and 65 % of mirrors are vertically misaligned of about 3 mrad at maximum.

6.4 Prospects

The Cherenkov photons originated in the RICH1 detector hit the reflective surface, the mirror wall, in a pseudo-circular region, i.e. the disk. The reflection point of each individual photon is not known because the photon emission point is randomly distributed along the particle path in the radiator (Sec. 2.2). The disk might be entirely included in a single mirror element or it can be shared among several adjacent mirror elements. Since the Cherenkov angle at saturation is 52 mrad, the disk can be shared by three mirrors at maximum. In case of any misalignment of the mirrors, parts of the image of the disk in the photon detection area are distorted. The detected photons do not follow the ring shape fluently and the particle identification algorithm might be misguided, especially in the case when more events are detected at the same time.

In the previous Chapters the ability of the CLAM method to detect mirrors misalignments was discussed and proved. There are two possible ways of prospective work to be followed: (i) to include the results of the CLAM measurements in the COMPASS data analysis or (ii) to directly correct the position of individual mirrors using the joints.

In the first case, the information about the mirror alignment can be used in the reconstruction and data analysis package for the RICH1 detector, called RICHONE [26].

In the second case, the corrections could be applied directly if the mirror wall is equipped by remotely driven actuators. The requirements of such a system, which would be able to apply such corrections, are the resolution of the applied positioning and the compatibility with the radiator gas purity, since the good UV-light transmission of the radiator gas down to 160 nm has to be preserved. Light piezo micro-metric actuators can adjust the individual mirror inclination; they are compatible with the radiator gas purity and they can be locally mounted without causing a significant increase of the mass of the overall radiation length of the mirror wall. Thus, the risk that an extra weight would deform the mirror suspension structure would be avoided.

In the proposal of a remote alignment of large mirror array for RICH1 detector [95], a non-resonant piezo actuator NexLine N100 [96] produced by PiezoWalk is discussed. The motion of the NexLine miniature High-Load piezo nanopositioning device is generated through the succession of coordinated clamp/unclamp and expand/contract cycles. The device can hold a stable position of a nanometer level in power-off mode with the full

holding force available. Because the position is held with zero operating voltage, leakage currents cannot affect the integrity of the piezo drive, which ensures long life time of the actuator. Furthermore, the active parts in all the piezo motors are made of vacuum-compatible ceramics, thus they do not contaminate the UV-light sensitive environment.

The feasibility of the proposed application has been tested and proved in a laboratory exercise, using a RICH mirror element mounted on a holder identical to the RICH1 one. The mirror was tilted in the range of ± 6 mrad. Within the measurement resolution of $40 \mu\text{rad}$, no hysteresis or nonlinearity were observed in the whole tested range. More details about the performed tests of the piezoelectric positioning of the RICH1 mirror can be found in [95].

7. Conclusions

The Thesis was focused on the study of possibilities to monitor the alignment of a large set of spherical mirrors which form the shape of a sphere. It was shown that the use of digital photogrammetry methods can offer an attractive approach to remotely measure the mirror misalignments with sufficient accuracy and speed comfort of the procedure.

In the field of particle physics, in RICH detectors with extended gas radiators, such as RICH1 of the COMPASS experiment at CERN SPS, image focusing is obtained by a large reflecting surfaces formed by mirror segments of a smaller size. The mirror walls are included in the gas vessel and they are sitting in the acceptance region of the experimental setup. The mirror segments must be very accurately aligned to form a single smooth reflecting surface. Any misalignments result in poorly focused images, directly affecting the detector resolution. Details of the RICH1 setup are presented in Chapter 2.

Chapter 3 summarizes state-of-the-art methods of the mirror wall misalignment measurements. In Cherenkov telescopes (Sec. 3.4), the alignment of the mirror wall can be monitored using the image of a distant light source, usually an image of a star. Other methods involve a set of laser beams to monitor each mirror segment individually. Since the segments are typically equipped by stepping motors, their position can be adjusted instantly. In comparison to Cherenkov telescopes, the implementation of a control system in a gaseous RICH counter must also satisfy the requirements of material budget and gas pollution. Another method, data collected by the spectrometer, is used (Sec. 3.2), where the alignment of a reference mirror has to be known precisely in advance. A large statistics is needed, hence the information is averaged over a long time intervals. In case of COMPASS RICH1 detector, no more than about one quarter of the mirrors, those sitting in the most populated areas, can be monitored with this approach. To ensure correct alignment, the laser alignment monitoring system (LAMS) can be adopted (Sec. 3.3). Because of large number of components needed by the

LAMS, the method can be used to monitor only a few mirror segments. The main disadvantage of the most advanced method - surveying the mirrors with the theodolite (Sec. 3.1) - is the need of direct access to the mirror setup. Thus, the surveying can be performed only when the spectrometer is not in operation mode. In 2001, the whole mirror wall was aligned and the measured residual misalignments showed a standard deviation of 0.06 mrad. The measurements of the misalignments were performed with the theodolite in autocollimation mode method (Sec. 3.1). In following years, the mirrors alignments were measured several times between the experiment data taking periods (from 2002 to 2012 [86, 91–94]). Because of a certain difficulty of the theodolite measurement method, the time and space demands, only a few selected mirrors were investigated. The theodolite must be oriented to the center of mirror very precisely. During the theodolite measurements, the misalignments with a random distribution in the range of 0 – 1 mrad have been observed, with a few elements exhibiting the misalignments of about 1.5 mrad. The cause of the misalignments emerged after the initial alignment is not known. It was obvious that a new complementary method for the online monitoring of the mirror wall segments had been missing.

Chapter 4 introduces the CLAM method which is the optical online monitoring system of the mirrors misalignments. The method was proposed by Sergio Costa and Jean-Christophe Gayde in 2005. The proposal was adopted in 2007. The rectangular grid, placed near the focal plane of the mirror wall inside the detector vessel, is made of retro-reflective strips. The grid is illuminated by high luminosity LEDs. The images of the grid, reflected by the spherical mirrors, are collected by four high resolution cameras. Small tilts of a mirror create discontinuities of grid line images, reflected by adjacent mirrors. This observed shift of lines images provides an information about the direction and amount of the mirror tilt.

There are two ways to measure the mirrors misalignments discussed in the Thesis: The relative and absolute measurement. The both methods were implemented by the author in the frame of this Thesis. The relative measurement, proposed in Chapter. 5, is based on the comparison of pictures taken by the camera. It measures a difference according to a reference picture. A laboratory measurement was performed to obtain the relationship between the shift of conics in the image in horizontal and vertical directions and the corresponding inclinations for each mirror. To find the lines in the image and to evaluate the relative change in their position, two image processing methods were adopted - mathematical morphology and Hough transform. Depending on the mirror position within the mirror wall,

shift of one pixel corresponds to the mirror rotation of $0.14 \div 0.20$ mrad. The method is fast and helps in fast visual inspections of the behavior of mirrors inside the detector RICH1. During the taking photographs, several conditions have to stay consistent, e.g. light conditions and camera setup. The comparison of pictures, taken during the run at different pressure and temperature conditions, shows that some mirrors exhibit a slow continuous motion, characterized by a typical relative tilt of 0.05 mrad in the horizontal and 0.11 mrad in the vertical direction. Some mirrors tend to a stable position after 2 months of run. Unfortunately, several mirrors were misaligned since the beginning when the CLAM data collection started.

The new absolute measurement method, introduced in Chapter 6, was developed to determine directly mirror tilt/orientation using only one picture. The idea, that well aligned mirrors share the same center of curvature and for a misaligned mirror the center of curvature differs, was adopted. The process to obtain the mirrors misalignments involves mainly image processing and digital photogrammetry techniques. The influence of the used optical system, pressure and temperature changes are considered in the calculations. The algorithm was tested on simulated data with the maximum resulting error of 2 % from the correct value. The utilization of the laboratory measurements results shows that the sensitivity of the absolute measurement algorithm is in the order of 0.05 mrad.

In the default setup the grid structure is illuminated by two LEDs. The effect of different time of illumination together with the used number of LEDs is shown. Considering only both LEDs switched on during the test, the variation of the detected misalignment is less than 0.05 mrad in wide range of illumination times. The accuracy of the method is influenced mainly by the estimate of the position of a CLAM camera. It is presented that the algorithm can be used to monitor mirrors position even during COMPASS run period. The detected misalignments of all the mirrors were performed with the CLAM method. The resulting values indicate that almost 50 % of mirrors are horizontally misaligned up to 3 mrad at maximum and 65 % of mirrors are vertically misaligned of about 3 mrad at maximum.

The information about the mirror alignment can be used in the reconstruction and analysis package for the RICH1 detector, called RICHONE. The corrections could be also applied directly to the mirrors if the mirror wall is equipped by remotely driven actuators. The two attitudes are introduced in Sec. 6.4. The possibility to correct the mirror misalignments without accessing the radiator vessel has other advantages: If the vessel is always closed, the mirror segments can be constantly kept in a dry, clean

atmosphere, thus preventing the degradation of the reflecting surface by moisture and dust. Measuring the mirrors misalignments and possibly adjusting their position can enhance the RICH1 performance by means of the increase of the resolution of the measured Cherenkov angle and consequently increasing the range of momentum for K/π separation. The newly developed method can be used in other Cherenkov detectors as well.

Bibliography

- [1] The COMPASS Collaboration, “COMPASS,” *CERN Document Server*, 1996.
- [2] M. Alekseev *et al.*, “Gluon polarisation in the nucleon and longitudinal double spin asymmetries from open charm muoproduction,” *Physics Letters B*, vol. 676, no. 1â3, pp. 31–38, Jun. 2009.
- [3] —, “Flavour separation of helicity distributions from deep inelastic muon-deuteron scattering,” *Physics Letters B*, vol. 680, no. 3, pp. 217–224, Sep. 2009.
- [4] —, “Collins and sivers asymmetries for pions and kaons in muon-deuteron DIS,” *Physics Letters B*, vol. 673, no. 2, pp. 127–135, Mar. 2009.
- [5] P. Abbon *et al.*, “The COMPASS experiment at CERN,” *Nuclear Instruments and Methods in Physics Research Section A: Accelerators, Spectrometers, Detectors and Associated Equipment*, vol. 577, no. 3, pp. 455–518, Jul. 2007.
- [6] G. K. Mallot, “The COMPASS spectrometer at CERN,” *Nuclear Instruments and Methods in Physics Research Section A: Accelerators, Spectrometers, Detectors and Associated Equipment*, vol. 518, no. 12, pp. 121–124, Feb. 2004.
- [7] “CERN,” <http://home.web.cern.ch/>.
- [8] “New compass page,” <http://wwwcompass.cern.ch/>.
- [9] H. Liu *et al.*, “Radiation-luminescence-excited quantum dots for in vivo multiplexed optical imaging,” *Small*, vol. 6, no. 10, p. 10871091, 2010.

- [10] C. Joram, “The evolution of the cherenkov imaging technique in high energy physics,” *Nuclear Physics B - Proceedings Supplements*, vol. 109, no. 2-3, pp. 153–161, Jun. 2002.
- [11] B. N. Ratcliff, “Imaging rings in ring imaging cherenkov counters,” *Nuclear Instruments and Methods in Physics Research Section A: Accelerators, Spectrometers, Detectors and Associated Equipment*, vol. 502, no. 1, pp. 211–221, Apr. 2003.
- [12] T. Ypsilantis and J. Seguinot, “Theory of ring imaging cherenkov counters,” *Nuclear Instruments and Methods in Physics Research Section A: Accelerators, Spectrometers, Detectors and Associated Equipment*, vol. 343, no. 1, pp. 30–51, Apr. 1994.
- [13] P. Cherenkov, “Visible emission of clean liquids by action of gamma radiation,” *Doklady Akademii Nauk SSSR*, vol. 2, p. 451, 1934.
- [14] I. M. Frank and I. E. Tamm, “Coherent radiation of fast electrons in a medium,” *Doklady Akademii Nauk SSSR*, vol. 14, p. 107, 1937.
- [15] E. Albrecht *et al.*, “Status and characterisation of COMPASS RICH-1,” *Nuclear Instruments and Methods in Physics Research Section A: Accelerators, Spectrometers, Detectors and Associated Equipment*, vol. 553, no. 12, pp. 215–219, Nov. 2005.
- [16] J. A. Brown and W. H. Mears, “Physical properties of n-perfluorobutane,” *The Journal of Physical Chemistry*, vol. 62, no. 8, pp. 960–962, 1958.
- [17] G. Lenzen, E. Schyns, J. Thadome, and J. Werner, “The use of fluorocarbon radiators in the DELPHI RICH detectors,” *Nuclear Instruments and Methods in Physics Research Section A: Accelerators, Spectrometers, Detectors and Associated Equipment*, vol. 343, no. 1, pp. 268–272, Apr. 1994.
- [18] E. Albrecht *et al.*, “The radiator gas and the gas system of COMPASS RICH-1,” *Nuclear Instruments and Methods in Physics Research Section A: Accelerators, Spectrometers, Detectors and Associated Equipment*, vol. 502, no. 1, pp. 266–269, Apr. 2003.
- [19] ———, “The mirror system of COMPASS RICH-1,” *Nuclear Instruments and Methods in Physics Research Section A: Accelerators,*

- Spectrometers, Detectors and Associated Equipment*, vol. 502, no. 1, pp. 236–240, Apr. 2003.
- [20] S. Costa, “The mirror system of COMPASS RICH-1,” INP Demokritos, 2002.
- [21] E. Albrecht *et al.*, “COMPASS RICH-1,” *Nuclear Instruments and Methods in Physics Research Section A: Accelerators, Spectrometers, Detectors and Associated Equipment*, vol. 502, no. 1, pp. 112–116, Apr. 2003.
- [22] P. Abbon *et al.*, “Design and construction of the fast photon detection system for COMPASS RICH-1,” *Nuclear Instruments and Methods in Physics Research Section A: Accelerators, Spectrometers, Detectors and Associated Equipment*, vol. 616, no. 1, pp. 21–37, Apr. 2010.
- [23] S. Levorato, “Measurement of transverse spin effect in COMPASS on a transversely polarised proton target,” Ph.D. dissertation, University of Trieste, 2009.
- [24] T. Ypsilantis and J. Seguinot, “Theory of ring imaging cherenkov counters,” *Nuclear Instruments and Methods in Physics Research Section A: Accelerators, Spectrometers, Detectors and Associated Equipment*, vol. 343, no. 1, pp. 30–51, Apr. 1994.
- [25] P. Abbon *et al.*, “Pattern recognition and PID for COMPASS RICH-1,” *Nuclear Instruments and Methods in Physics Research Section A: Accelerators, Spectrometers, Detectors and Associated Equipment*, vol. 595, no. 1, pp. 233–236, Sep. 2008.
- [26] ———, “Particle identification with COMPASS RICH-1,” *Nuclear Instruments and Methods in Physics Research Section A: Accelerators, Spectrometers, Detectors and Associated Equipment*, vol. 631, no. 1, pp. 26–39, Mar. 2011.
- [27] J. C. Gayde, “COMPASS RICH - CLAM,” technical report, CERN, Geneva, May 2007.
- [28] C. J. Brochu, J. W. Moffat, and G. A. Morin, “Optical alignment of the spherical antenna measurement system,” Tech. Rep., Nov. 1997.

- [29] H. G. Bas, “The accuracy of using theodolite in close-range engineering measurements,” in *ISPRS Volume XXXIII Part B5(/1+2)*, vol. 2000, Amsterdam, pp. 45–52.
- [30] P. Križan *et al.*, “The RICH detector for HERA-B,” *Nuclear Instruments and Methods in Physics Research Section A: Accelerators, Spectrometers, Detectors and Associated Equipment*, vol. 371, no. 1-2, pp. 295–299, Mar. 1996.
- [31] A. Gorišek, P. Križan, S. Korpar, and M. Starič, “Alignment of the HERA-B RICH optical system with data,” *Nuclear Instruments and Methods in Physics Research Section A: Accelerators, Spectrometers, Detectors and Associated Equipment*, vol. 433, no. 12, pp. 408–412, Aug. 1999.
- [32] C. D’Ambrosio *et al.*, “Monitoring, alignment and control of the RICH detectors,” Apr. 2001.
- [33] P. Schiavon, “COMPASS RICH-1, hints for mirror alignment, progress report,” Technical report, Oct. 1999.
- [34] A. Papanestis, “The calibration and alignment of the LHCb RICH system,” *Nuclear Instruments and Methods in Physics Research Section A: Accelerators, Spectrometers, Detectors and Associated Equipment*, vol. 595, no. 1, pp. 248–251, Sep. 2008.
- [35] A. Papanestis, G. Vidal-Sitjes, P. Soler, and A. Macgregor, “Laser alignment monitoring system (LAMS) for the RICH,” in *CERN Document Server*, vol. 2007, CERN, Geneva, Jun. 2007.
- [36] C. Blanks, J. Nardulli, and F. Soomro, “The laser alignment and monitoring system for the LHCb RICH detectors,” Jun. 2011.
- [37] “IACT,” Oct. 2013, page Version ID: 541309450.
- [38] R. Cornils *et al.*, “The optical system of the H.E.S.S. imaging atmospheric cherenkov telescopes. part II: mirror alignment and point spread function,” *Astroparticle Physics*, vol. 20, no. 2, pp. 129–143, Nov. 2003.
- [39] J. A. Toner, V. A. Acciari, A. Cesarini, and E. Al, “Bias alignment of the VERITAS telescopes,” *International Cosmic Ray Conference*, vol. 3, pp. 1401–1404, 2008.

- [40] A. Kawachi *et al.*, “The optical reflector system for the CANGAROO-II imaging atmospheric cherenkov telescope,” *Astroparticle Physics*, vol. 14, no. 4, pp. 261–269, Jan. 2001.
- [41] V. D. M. Garczarczyk, “The active mirror control of the MAGIC telescope,” *28th International Cosmic Ray Conference, Universal Academy Press*, vol. 2003, pp. 2935–2938.
- [42] “VERITAS telescope,” <http://veritas.sao.arizona.edu/index.php>.
- [43] A. McCann, D. Hanna, and M. McCutcheon, “An alignment system for imaging atmospheric cherenkov telescopes,” *Instrumentation and Methods for Astrophysics (astro-ph.IM); High Energy Astrophysical Phenomena (astro-ph.HE)*, Jul. 2009.
- [44] S. Dalla Torre, “TEMPERATURE MEASUREMENTS DURING MIRROR ALIGNMENT IN SPRING 2001,” technical report, 2001.
- [45] J. C. Gayde, “COMPASS-RICH 1, réglage de l’orientation de 116 miroirs du RICH, mesures du 2 mai au 1er juin 2001,” technical report, 2001.
- [46] S. Dalla Torre *et al.*, “Remote alignment of large mirror array for RICH detectors,” *Nuclear Instruments and Methods in Physics Research Section A: Accelerators, Spectrometers, Detectors and Associated Equipment*, vol. 595, no. 1, pp. 220–223, Sep. 2008.
- [47] S. Costa *et al.*, “CLAM, a continuous line alignment and monitoring method for RICH mirrors,” *Nuclear Instruments and Methods in Physics Research Section A: Accelerators, Spectrometers, Detectors and Associated Equipment*, vol. 553, no. 12, pp. 135–139, Nov. 2005.
- [48] “POV-Ray - the persistence of vision raytracer,” <http://www.povray.org/>.
- [49] “Canon global,” <http://www.canon.com/>.
- [50] “NIPPON CARBIDE INDUSTRIES CO.,INC.” <http://www.carbide.co.jp/en/>.
- [51] J.-C. Gayde and S. Berni, “COMPASS RICH 1 - CLAM POSITION OF THE GRID POINTS report,” Apr. 2007.

- [52] “Philips lumileds LED lighting | LUXEON LEDs | LED lighting solutions,” <http://www.philipslumileds.com/>.
- [53] M. Svec, “Online monitoring mirrors in detector of cherenkov’s radiation,” Diploma thesis, Technical Univezity of Liberec, Sep. 2007.
- [54] M. Alexeev *et al.*, “On-line mirror alignment monitoring method for COMPASS RICH-1,” *Nuclear Instruments and Methods in Physics Research Section A: Accelerators, Spectrometers, Detectors and Associated Equipment*, vol. 595, no. 1, pp. 194–196, Sep. 2008.
- [55] “NI LabVIEW - improving the productivity of engineers and scientists - national instruments,” <http://sine.ni.com/np/app/main/p/docid/nav-104/lang/cs/>.
- [56] A. Peters, “Lectures on image processing,” https://archive.org/details/Lectures_on_Image_Processing.
- [57] M. Sonka, V. Hlavac, and R. Boyle, *Image Processing, Analysis, and Machine Vision*. Nelson Education Limited, 2008.
- [58] D. H. Ballard, “Generalizing the hough transform to detect arbitrary shapes,” *Pattern Recognition*, vol. 13, no. 2, pp. 111–122, 1981.
- [59] “International communication union: Recommendation BT.601,” <http://www.itu.int/rec/R-REC-BT.601/>.
- [60] J. Serra, *Image analysis and mathematical morphology*. London: Academic Press, 1982.
- [61] P. Hough, “Method and means for recognizing complex patterns,” 1962, uS Patent 3,069,654.
- [62] S. Robson and S. Kyle, *Close Range Photogrammetry: Principles, Techniques and Applications*. Wiley, ISBN:0470106336, 9780470106334, 2006.
- [63] R. Hartley and A. Zisserman, *Multiple View Geometry in Computer Vision*. Cambridge University Press, ISBN: 0521540518, 2003.
- [64] “the american society for photogrammetry and remote sensing,” <http://www.asprs.org>.

- [65] J. P. de Villiers, F. W. Leuschner, and R. Geldenhuys, “Centi-pixel accurate real-time inverse distortion correction,” vol. 7266, 2008, pp. 726 611–726 611–8.
- [66] D. Brown, “Decentering distortion of lenses,” *Photometric Engineering*, vol. 32, no. 3, pp. 444–462, 1966.
- [67] R. Tsai, “A versatile camera calibration technique for high-accuracy 3D machine vision metrology using off-the-shelf TV cameras and lenses,” *IEEE Journal of Robotics and Automation*, vol. 3, no. 4, pp. 323–344, 1987.
- [68] G. Q. Wei and S. D. Ma, “Implicit and explicit camera calibration: Theory and experiments,” *IEEE Trans. Pattern Anal. Mach. Intell.*, vol. 16, no. 5, p. 469480, May 1994.
- [69] Z. Zhang, “Flexible camera calibration by viewing a plane from unknown orientations,” in *The Proceedings of the Seventh IEEE International Conference on Computer Vision, 1999*, vol. 1, 1999, pp. 666–673 vol.1.
- [70] “AICON 3D systems,” <http://aicon3d.com/start.html>.
- [71] A. Mikš and P. Pokorný, “Vliv tlouky planparalelní desky na zkreslení objektivu,” *Jemná mechanika a optika*, vol. 2011, no. 7-8, pp. 220–223, 2011.
- [72] —, “Vliv disperze skla planparalelní desky na kvalitu zobrazení optické soustavy,” *Jemná mechanika a optika*, vol. 2013, no. 7-8, pp. 214–218, 2013.
- [73] “LHCb wiki,” <https://twiki.cern.ch/twiki/bin/view/LHCb/C4F10>.
- [74] “Refractive index tables,” <http://refractiveindex.info>.
- [75] “Refractive indices - indexy lomu,” <http://ottp.fme.vutbr.cz/~pavelek/optika/2003.htm>.
- [76] I. I. Bigi, L. Moroni, and S. i. d. fisica, *Heavy Flavour Physics: A Probe of Nature’s Grand Design : Varenna on Lake Como, Villa Monastero, 8-18 July 1997*. IOS Press, Jan. 1998.

- [77] M. F. L'Annunziata, *Handbook of Radioactivity Analysis*. Academic Press, 2012.
- [78] "Level set method," http://en.wikipedia.org/wiki/Level_set_method, 2013.
- [79] COMSOL, "Comsol multiphysics user's guide, version 4.3a," Nov. 2012.
- [80] "Physical properties of gases," <http://encyclopedia.airliquide.com/..encyclopedia.asp>.
- [81] "Engineering toolbox: The individual and universal gas constant," http://www.engineeringtoolbox.com/individual-universal-gas-constant-d_588.html.
- [82] "Mineralogy database," <http://webmineral.com>.
- [83] E. Süli and D. F. Mayers, *An Introduction to Numerical Analysis*. Cambridge University Press, Aug. 2003.
- [84] "MATLAB - the language of technical computing," <http://www.mathworks.com/products/matlab/>.
- [85] "COMPASS RICH1," <http://wwwcompass.cern.ch/compass/detector/..rich/welcome.html>.
- [86] B. Beauquis, J. C. Gayde, and N. L'Olivier, "COMPASS RICH 1 CONTROL OF THE ORIENTATION OF 8 TOP SPHERE AND 15 BOTTOM SPHERE MIRRORS," Tech. Rep. EDMS N°: 837912, 2007.
- [87] J. B. MacQueen, "Some methods for classification and analysis of MultiVariate observations," in *Proc. of the fifth Berkeley Symposium on Mathematical Statistics and Probability*, L. M. L. Cam and J. Neyman, Eds., vol. 1. University of California Press, 1967, pp. 281–297.
- [88] H.-J. Mucha, "Späth, h.: Cluster dissection and analysis: theory, FORTRAN programs, examples." *Biometrical Journal*, vol. 28, no. 2, p. 182, 1986.
- [89] N. Otsu, "A threshold selection method from gray-level histograms," *IEEE Transactions on Systems, Man and Cybernetics*, vol. 9, no. 1, pp. 62–66, Jan. 1979.

- [90] P. Dalloz and R. Valbuena, “THE COMPASS RICH-1 MIRROR WALL GEOMETRY,” Tech. Rep. EST-ESI/99-08 Rev 2, 2000.
- [91] P. Andreo, A. Behrens, E. Lacroix, and J. C. Gayde, “COMPASS RICH 1 POSITION OF BACK FLANGE AND MIRROR SUPPORT STRUCTURE AND CONTROL OF ORIENTATION OF SOME MIRRORS,” Tech. Rep. EDMS N°: 1238351, 2012.
- [92] J. C. Gayde, “COMPASS RICH 1 POSITION OF RICH1 AND CONTROL OF THE ORIENTATION OF THE MIRRORS BEFORE AND AFTER MOVEMENT,” Tech. Rep. EDMS N°: 605541, 2005.
- [93] J. C. Gayde, B. Beauquis, and L. Sandri, “COMPASS RICH 1 CONTROLE DE LORIENTATION DE 27 MIROIRS SPHERE DU BAS,” Tech. Rep. EDMS N°: 458246, 2004.
- [94] J. C. Gayde, “COMPASS RICH 1 CONTROLE DE LORIENTATION DE 100 MIROIRS,” Tech. Rep. EDMS N°: 343027, 2002.
- [95] S. Dalla Torre *et al.*, “Remote alignment of large mirror array for RICH detectors,” *Nuclear Instruments and Methods in Physics Research Section A: Accelerators, Spectrometers, Detectors and Associated Equipment*, vol. 595, no. 1, pp. 220–223, Sep. 2008.
- [96] “Piezo nano positioning,” http://www.physikinstrumente.com/en/..products/piezo_motor/nexline.php.

Publications of the Author

- [1] M. Šulc, J. Polák, L. Steiger, D. Kramer: Optická soustava pro detektor Čerenkovova záření. *JMO*, (2013) 52.
- [2] L. Steiger, M. Šulc: Počítačová korekce rozladění polohy zrcadel v detektoru Čerenkovova záření RICH-1 experimentu COMPASS v CERN. *JMO*, (2013) 211-213.
- [3] M. Šulc J. Polák, L. Steiger, D. Kramer, M. Finger, M. Slunečka: New optics for resolution improving of Ring Imaging Cherenkov detectors. *EPJ Web of Conferences* (2013) 48.
- [4] M. Alexeev et al.: Mirror alignment control for COMPASS RICH-1 detector, *Nucl. Instrum. Methods Phys. Res., A* 639 (2011), 219-221
- [5] M. Šulc et al.: On-line mirror alignment monitoring method for COMPASS RICH-1, *Nucl. Instrum. Methods Phys. Res., A* 595 (2008) 194-196.
- [6] S. Levorato, et al.: Remote alignment of large mirror array for RICH detectors, *Nucl. Instr. and Meth., A* 595 (2008) 220-223.

Publications of the Author which are not directly related to the Thesis

- [1] C. Adolph et al. Transverse target spin asymmetries in exclusive ρ^0 muoproduction. arXiv:1310.1454 (2013).at <<http://arxiv.org/abs/1310.1454>>
- [2] M. Alexeev et al.: Hadron Transverse Momentum Distributions in Muon Deep Inelastic Scattering at 160 GeV/c, *Eur. Phys. J. C*, 73 (2013), 18p.
- [3] M. Alexeev et al.: Study of $\Sigma(1385)$ and $\Xi(1321)$ hyperon and anti-hyperon production in deep inelastic muon scattering, *Eur. Phys. J. C*, (2013) 11p.
- [4] M. Alexeev et al.: Leading and Next-to-Leading Order Gluon Polarization in the Nucleon and Longitudinal Double Spin Asymmetries from Open Charm Muoproduction, *Phys. Rev. D*, 87 (2013)
- [5] M. Alexeev et al.: Ion backflow in thick GEM-based detectors of single photons, *Journal of Instrumentation*, 8(1)(2013)
- [6] C. Adolph et al.: D^* and D meson production in muon nucleon interactions at 160 GeV/c. *The European Physical Journal C* 72, (2012).
- [7] C. Adolph et al.: Exclusive muoproduction on transversely polarised protons and deuterons. *Nuclear Physics B* 865, 1–20 (2012).
- [8] C. Adolph et al.: I – Experimental investigation of transverse spin asymmetries in μ -p SIDIS processes: Collins asymmetries. *Physics Letters B* 717, 376–382 (2012).
- [9] C. Adolph et al.: II – Experimental investigation of transverse spin asymmetries in μ -p SIDIS processes: Sivers asymmetries. *Physics Letters B* 717, 383–389 (2012).

- [10] C. Adolph et al.: Measurement of the Cross Section for High- p_T Hadron Production in Scattering of 160 GeV/c Muons off Nucleons. *Phys. Rev. Lett.* (2012).
- [11] M. Alexeev et al.: Progress towards a THGEM-based detector of single photon, *Nucl. Instrum. Methods Phys. Res.*, A 639(2011), 130-133
- [12] P. Abbon et al.: Particle identification with COMPASS RICH-1, *Nucl. Instrum. Methods Phys. Res.*, A 631 (2011), 26-39
- [13] S. Levorato et al.: Detection of single photons with ThickGEM-based counters, *IOP Science: Journal of instrumentation: Proc. 2nd International Conference on Micro Pattern Gaseous Detectors (MPGD)* (2011)
- [14] S. Levorato et al.: Development of THGEM- based Photon Detectors for COMPASS RICH-1, *ELSEVIER: Physics Procedia: Proc. Technology and Instrumentation in Particle Physics 2011 (TIPP)*
- [15] S. Levorato et al.: Detection of single photons with THickGEM-based counters, *Nucl. Instrum. Methods Phys. Res.*, A 676 (2011)
- [16] M. Sulc et al.: A study of the RICH gas refractive index, *Nucl. Instrum. Methods Phys. Res.*, A 639 (2011), 271-273
- [17] R. Birsa et al.: The experience of building and operating COMPASS RICH-1, *Nucl. Instrum. Methods Phys. Res.*, A 639 (2011), 15-19
- [18] M. Alexeev et al.: Micropattern gaseous photon detectors for Cherenkov imaging counters, *Nucl. Instrum. Methods Phys. Res.*, A 623 (2010), 129-131
- [19] P. Abbon et al.: Particle identification with the fast COMPASS RICH-1 detector, *Nucl. Instrum. Methods Phys. Res.*, A 623 (2010), 330-332
- [20] M. Alexeev et al.: Design and construction of the fast photon detection system for COMPASS RICH-1, *Nucl. Instrum. Methods Phys. Res.*, A 616 (2010), 21-37
- [21] M. Alexeev et al.: THGEM based photon detector for Cherenkov imaging applications, *Nucl. Instrum. Methods Phys. Res.*, A 617 (2010) 396-397.
- [22] F. Tessarotto et al.: Development of a THGEM-based Photon Detector for RICH Applications, (*Nuovo Cimento*), C 32 (2009) 419-423.
- [23] P. Abbon et al.: The Upgrade Project of the RICH-1 of the COMPASS Experiment , *Nuovo Cimento*, C 32 (2009) 407-412.

- [24] M. Alexeev et al.: Development of THGEM-based photon detectors for Cherenkov Imaging Counters, *J. Instrum.*, 5 (2010) P03009.
- [25] P. Abbon et al.: The COMPASS RICH-1 detector upgrade, *Eur. Phys. J. Spec. Top.*, 162 (2008) 251-257.
- [26] P. Abbon et al.: The COMPASS RICH-1 fast photon detection system, *Nucl. Instrum. Methods Phys. Res., A* 595 (2008) 23-26.
- [27] P. Abbon et al.: Pattern recognition and PID for COMPASS RICH-1, *Nucl. Instrum. Methods Phys. Res., A* 595 (2008) 233-236.
- [28] P. Abbon et al.: The characterisation of the multianode photomultiplier tubes for the RICH-1 upgrade project at COMPASS, *Nucl. Instrum. Methods Phys. Res., A* 595 (2008) 177-179.
- [29] P. Abbon et al.: The fast readout system for the MAPMTs of COMPASS RICH-1, *Nucl. Instrum. Methods Phys. Res., A* 595 (2008) 204-207.
- [30] P. Abbon et al.: Fast photon detection for COMPASS RICH-1, *Nucl. Instrum. Methods Phys. Res., A* 572 (2007) 419-421.
- [31] P. Abbon et al.: Design and status of COMPASS FAST-RICH, *Nucl. Instrum. Methods Phys. Res., A* 567 (2006) 114-117.
- [32] C. Shill et al.: Fast photon detection for the COMPASS RICH detector, *Nucl. Phys. B, Proc. Suppl.*, 172 (2007) 75-78.
- [33] P. Abbon et al.: Fast Photon Detection for Particle Identification with COMPASS RICH-1, *Nucl. Instrum. Methods Phys. Res., A* 580 (2007) 906-909.
- [34] P. Abbon et al.: Studies for a fast RICH, *9th ICATPP Conference on Astroparticle, Particle, Space Physics, Detectors and Medical Physics Applications*, (2005) 103-107.